UNIVERSITÀ DEGLI STUDI DELL’INSUBRIA

FACOLTÀ DI SCIENZE MATEMATICHE, FISICHE E NATURALI

DIPARTIMENTO DI FISICA E MATEMATICA

Ph.D. THESIS

MULTIPLE-WELLED TUNNELING SYSTEMS IN GLASSES AT LOW TEMPERATURES

PALIIENKO MAKSYM

Supervisor:
Prof. GIANCARLO JUG

May 2011

THESIS DEFENCE: May 30th, 2011

JURY MEMBERS:

Professor PETER FULDE

(MAX-PLANCK INSTITUT – Dresden,
ASIA PACIFIC CENTER - Pohang)

Professor FRANÇOIS LADIEU

(SPEC CEA-SACLAY)

Professor DAVID SHERRINGTON

(UNIVERSITY OF OXFORD,
LOS ALAMOS NATIONAL LABORATORY,
SANTA FE INSTITUTE)

Abstract

Glasses at low temperatures show rather universal physical properties that are attributed to the low-energy excitations that characterize all kinds of amorphous solids.

The two-level system (2LS) tunneling model (TM) has been accepted as the explanation for the thermal, dielectric and acoustic properties of glasses at T<1 K. The magnetic effects discovered recently in the multi-silicate glasses and the temperature dependence of the specific heat and permittivity of some mixed glasses indicate the need however for a suitable generalization of the 2LS TM.

All these anomalous effects can be explained well in terms of the very same new (anomalous) tunneling systems (ATS) model. ATS in glasses are provided by the process of partial devitrification of the glassy network due to the presence of network-modifying ions in real glasses. A new probability distribution, which is inversely proportional to the energy asymmetry, takes into account partial devitrification. Using the ATS model we arrive at some expressions for the contribution to the dielectric constant and heat capacity anomaly from the advocated ATS with a few new parameters, which are concerning to the ATS and characterizing their energy gap distribution. We have shown the role of the ATS already in zero magnetic field in the multi-component glasses. The multi-welled ATS together with STM's 2LS explain qualitatively, as well as quantitatively and with reasonable parameters, the relative change of the dielectric permittivity at zero magnetic field for multi-component glasses such as AlBaSiO (or BAS) and BK7. They explain also the relative change of the dielectric permittivity and heat capacity with temperature T and with alkali concentration x in the mixed $(SiO_2)_{1-x}(K_2O)_x$ glass.

In order to explain the effects of the magnetic field we consider the motion of a fictitious charged particle in a 3-welled potential as a working example, coupling to the magnetic field through the particle's orbital motion. The magnetic-field dependent Hamiltonian of a single ATS has been modified introducing the Aharonov-Bohm phase. The experimental data of the relative change of the dielectric permittivity and loss in the presence of the magnetic field have been carefully fitted using the ATS model.

The polarization echo's theory has been improved and extended to the case of the independent ATS model describing glasses in a magnetic field. The agreement between theory and experiment is highly satisfactory, given the simplifications used in the theory. The isotope substitution effect on the dipole-echo amplitude also can be explained in a simple way with our model.

The interpretation of the extracted material parameters brings us to confirm the existence of the coherent tunneling of a cluster of N true particles, with a value of N ranging from about 25 coherent-tunneling particles in a cluster at the lowest temperatures, to about 600 at the higher temperatures.

MULTIPLE-WELLED TUNNELING SYSTEMS IN GLASSES AT LOW TEMPERATURES

CONTENTS

Chapter 1

Introduction

Glasses are materials that play an essential role in science and technology. Their wide application in industry is dictated by the economic and practical points of view (cheap and easy production, chemical neutrality and mechanical strength). Their chemical, physical and in particular optical properties make them appropriate for applications such as flat and container glass, optics and optoelectronics application materials, solar energy industry, high-tech information industry, semiconductor industry, laboratory equipment, thermal insulator (glass wool), reinforcement material (glass-reinforced plastic, glass fiber reinforced concrete) and glass art.

But their fundamental physical properties are hardly understood from first principles, in contrast to the long-studied crystalline solid-state materials. Thus the scientific challenge, stretched even further by recent startling discoveries.

The term glass is often used to describe any amorphous material that exhibits a glass transition temperature T_g, at which the material changes its behaviour from being glassy (a non-crystalline, infinite-viscosity solid) to being liquid (thus shapeless). T_g is always lower than the melting temperature T_m of the crystalline state of the material, if one exists. Because the glass transition is not a true thermodynamic transition, but rather a manifestation of divergent viscoelasticity and metastability, the exact value of T_g depends on the method used to produce the glassy state and the rate at which the temperature is lowered during fabrication. The final structure of the glass therefore depends on how slowly it has been cooled.

Glass exhibits an atomic structure close to that observed in the super-cooled liquid phase between T_m and T_g, but displays all the mechanical properties of a solid. Contrary to crystals, glasses do not possess any long-range order in their atomic arrangement. Therefore, it makes glass hard to be to mathematically described in a simple, tractable way.

The question of the nature of glass and of the transition from the liquid or the cristalline solid and a glassy phase is long-standing and still open question. According to P.W. Anderson, “the nature of the glass transition is the deepest and most important problem in solid-state physics”. The ultimate difference between the glassy and the over-cooled liquid state remains in fact a mystery.

It is well known that glasses display universal thermal and dielectric properties at the lower temperatures, properties which are very different from those of their crystalline counterparts. Below 1 K, the specific heat of dielectric glasses depends approximately linearly and the thermal conductivity almost quadratically on temperature, while cubic dependences for both properties are observed in crystals.

These thermal properties, together with other dielectric and acoustic universal properties, are well understood theoretically in terms of tunneling systems, since in 1972 Phillips and, independently, Anderson, Halperin and Varma introduced the tunneling model (TM), the fundamental postulate of which is the general existence of atoms (or small groups of atoms) which can tunnel between two configurations of very similar energy (the double-welled two-level systems as a simplest case). The distribution of energy asymmetries, barrier heights, etc., is such that the probability of the resulting tunneling two-level system having an energy splitting E is approximately independent of E. This presented an advancement in the study of glasses, a simplification in the mathematical modeling.

The two-level systems' (2LS) tunneling model (TM) has enjoyed an apparently impressive success. It gave the possibility to theoretical physicists to explain many of the characteristic features of glassy behaviour observed below 1 K (linear specific heat, logarithmic ultrasound velocity shift, T^2 thermal conductivity, etc.) and also to predict qualitatively a whole novel series of nonlinear effects.

However, the microscopic nature of the tunneling systems in glasses remains unknown. The tunneling model came under biting criticism by Yu and Legget (1998). Moreover, the limitations of the 2LS TM do not allow to explain quantitatively and even qualitatively (being in open contradiction) most of the properties of multi-component silicate and ceramic glasses in the presence (sometimes even in the absence) of a weak magnetic field, such as was found in a-Al_2O_3-BaO-SiO_2, BK7 (a borosilicate glass important for optical applications), Duran (ditto, for chemistry), a-$SiO_{2+x}C_yH_z$, $(SiO_2)_{1-x}(K_2O)_x$ glasses and so on. These materials are important for applications in technology, and not only for low-temperature thermometry, but also hopefully in the capacitive measurements of weak magnetic fields.

The relative dielectric constant and loss in some dielectric glasses show non-monotonic behaviour in the presence of weak to moderate magnetic fields, which does not scale with the concentration of paramagnetic impurities sometimes present in the glass, in trace ppm concentrations, due to specific contamination in the fabrication process. The amplitude of the dipole echo (similar to NMR's spin echo) in some non-magnetic glasses exhibits a strong non-monotonic (oscillating, even) dependence on the magnetic field (or pulses separation time) even for very weak fields (about 10 mT), whilst pure a-SiO_2 shows no response at all. The dipole-echo experiments in pure and deuterated a-glycerol and in the doped crystals KCl:Li with ^{6}Li and ^{7}Li isotopes exhibit even an effect of isotopic substitution on the dipole-echo amplitude. These effects are still very poorly understood.

Some unexplained older data of the dielectric permittivity in zero magnetic field for the mixed $(SiO_2)_{1-x}(K_2O)_x$ and $(SiO_2)_{1-x}(Na_2O)_x$ glasses for different concentration x present considerable difficulties to be understood within the standard tunneling model.

Up to now several different attempts have been put forwards to explain the magnetic effects: introducing dipole-dipole interactions between the tunneling systems, along with the proposal of the interaction between the tunneling systems and the magnetic field by introducing a Aharonov-Bohm orbital coupling. The presence of nuclear electric quadrupole moments of atoms contained in the magnetically responsive glasses put physicists on some attempts of coupling the tunneling systems to the nuclear quadrupole moments and then, via the nuclear magnetic moments, to the magnetic field. The nuclear approach has enjoyed some success.

However, the single model which could explain all kinds of reported, sometimes startling magnetic experiments in non-magnetic glasses is still absent.

These are incentives for further investigation to receive understanding of the novel physical properties, and which call for an extension of the standard tunneling model. A simple explanation for many astonishing experimental discoveries in the last decade can now be given in terms of one single model (the multi-welled tunneling model) involving some additional (and anomalous, with respect to the standard parameter distribution) tunneling systems. The new multi-welled tunneling model is the simplest magnetic extension of the tunneling model of the 1970s that can very well, qualitatively and quantitatively, explain: the relative change of the dielectric permittivity for mixed glasses in the absence and presence of the magnetic field, the variation of the permittivity and heat capacity with changing the concentration of the chemical components in the mixed glasses, and the highly non-monotonic, astonishing behaviour in the magnetic field of the polarization echo generated in glasses at high frequencies.

The thesis is organized as follows. In Chapter 2 we present an overview of the structure of glasses and the basic physics of the standard double-welled tunneling model. Chapter 3 describes the structure of real glasses and reports numerical simulations that help us in the understanding of the nature of the tunneling systems. In Chapter 4 we present an overview of the experiments on the mixed glasses indicating deviations from the standard tunneling model and we build up our own model in zero magnetic field. In Chapter 5 we present a review of the existent other models proposed to explain magnetic field effects in glasses. In Chapter 6 we describe the multi-welled tunneling model in the presence of a magnetic field. In Chapter 7 we present our own results for the magnetic-field dependence of the dielectric constant for several materials, in weak fields and with a simple attempt to explain behaviour in higher fields as well. In Chapter 8 we present our results for the dielectric loss and relaxation in a magnetic field. In Chapter 9 we present our results for the dipole-echo in a magnetic field, for the multi-silicate as well as for the organic glasses. The isotope effect finds a simple explanation. In Chapter 10 we present our interpretation of the fitting parameters, which sheds much new light on the nature of the tunneling systems. At the end of the thesis are the conclusions, outlook and references.

Chapter 2

Structural glasses at low temperatures: the standard tunneling model

2.1 General considerations

The modern thinking about the microscopic structure of glasses is based on Zachariasen's hypotheses [2.1]. Zachariasen noted similar mechanical properties (elastic modulus, etc.) between glasses and crystals and so expected similar structural energies and similar underlying atomistic building blocks. However, glasses have greater structural energies and are amorphous structures: glasses do not have the periodic (long range) order of a crystal, no infinitely-repeating unit cell (no repeating large scale structures), their 3D network lacks symmetry and periodicity, moreover glasses are isotropic - same average packing and structural properties in all directions. The most simple, studied and known glass is silica glass: SiO_2. X-ray investigation shows that the average distance between the nearest atoms of Si and O is 1.62 Å, and between the (next) nearest atoms of Si is 3 Å; that almost coincides with the inter-atomic spacing in the crystal versions of SiO_2 (quartz and crystobalite). But in the glasses a wide dispersion of the angles Si-O-Si from 120° to 180° is also observed. The local regular (short-ranged) order in silicate glasses is conserved at distances of 10-12 Å. In this complex single-component glass the unit cell consists of oxygen triangles or of oxygen tetrahedra around a silicon atom, connected randomly.

Real, multi-component oxide glasses contain appreciable amounts of cations which can form vitreous oxides (good glass-formers), and other cations which are able to replace isomorphically, or much more likely form their own phase-separated droplets, any of the glass formers. These network modifiers - combined alone with oxygen - would typically form a crystal (good crystal-formers). The glass- or Network-Forming (NF) cations are, typically: B^{3+}, Si^{4+}, P^{3+}, P^{5+}, As^{3+}, As^{5+}, Ge^{4+} . These cations are responsible for the glass-forming ability, and they combine together with oxygen atoms, creating the vitreous network of the glass. Other positive cations such as Na^{+}, K^{+}, Ca^{2+}, Ba^{2+}, Al^{3+} are capable of replacing the Si^{4+} ions, or more likely generate their own droplets by exploiting the vacua in the amorphous structure. These vacua, surrounded by oxygen atoms, necessarily must exist in the network, because the oxygen polyhedra in the glass network (tetrahedra or triangles) are connected randomly. These cations, which combined with oxygen would normally form crystals, are named Network-Modifiers (NM) [2.1, 2.2]. The structure of real glasses and the significance of the NM-ions will be discuss in Chapter 3.

After Zeller and Pohl published their celebrated findings [2.3] concerning the low-temperature thermal anomalies in glasses, for the next following few years about ten different models were proposed to explain their discoveries (see the review [2.4]). The most successful of these was a model developed by Anderson, Halperin and Varma [2.5] and independently by Phillips [2.4]. Later this became known as the "standard tunneling model" (STM), for its simplicity and wide application.

The STM is a phenomenological model based on the assumption that certain atoms or - rather - groups of atoms in disordered solids (Fig. 2.1b represents an old viewpoint now) have two (or more) spatial equilibrium positions (local potential minima), as opposite to perfect crystals (Fig. 2.1a), where the atoms have the same and only equilibrium positions. This assumption was confirmed in recent studies [2.6, 2.7] on computer modeling of the dynamics of the atomic structure of some amorphous solids like pure a-SiO_2 and a-SiO_2 with a small concentration of lithium oxide, Li_2O. Again in the 1970s and within the acoustic measurements [2.8, 2.9] a wide range of different materials have been investigated by more traditional experiments. The range of materials showing thermal anomalies below 1 K was extended to include disordered crystals and metallic glasses, thus showing not only the generality of the phenomena, but also that localized disorder, as present in imperfect crystals, was sufficient to reproduce effects found in true amorphous or glassy solids. Further, both thermal [2.10] and dielectric [2.11] measurements demonstrated that impurities could influence the properties of glasses below 1 K.

At low temperatures these atoms cannot overcome the potential barrier between two minima via thermal excitation. But they can get to the other minimum through quantum-mechanical tunneling. Due to the disorder of the atomic structure in the amorphous solids the minima of the double-well potentials have a wide range of barrier heights and depths of the potential minima. For the STM this configurational variability is described by the simplest possible model realization of the configurational energy landscape, which has the form of a paradigm one-dimensional double-well potential (Fig. 2.1c: x is not necessarily a linear coordinate, so a non-zero angular momentum is also possible).

This potential, created by the surrounding atoms (the tunneling particle is embedded), is shown as a function of one generalized configuration coordinate. The frequency ω_0 of the harmonic vibrations in both wells is taken to be the same. Since the barrier height is thought to be relatively small (V_B~100 K), the overlap of the tunneling wave functions of the localized harmonic-oscillator states in the left $|l\rangle$ and right $|r\rangle$ wells generates two localized states: a ground and an excited states. Below 1 K, the statistical population of the higher levels can be neglected, since they have an energy of at least $\hbar\omega_0$~100 K or above. Only the two lowest energy levels are believed to be important, with an energy difference determined by quantum mechanical tunnelling through the barrier, having tunnelling splitting Δ_0, and by the asymmetry of the ground-state harmonic-oscillator energies, Δ. Systems like those described above are known as tunneling two-level systems (2LS).

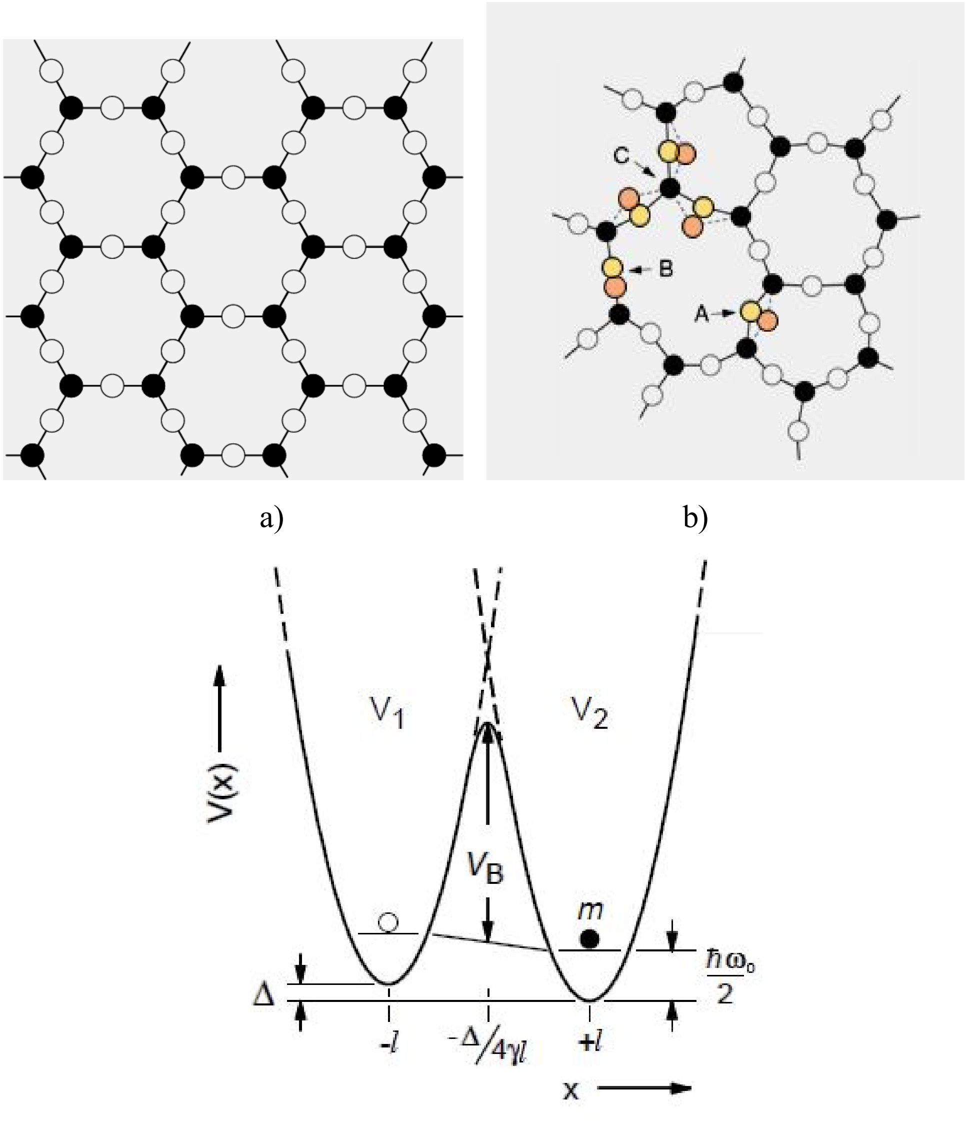

a)

b)

c)

Figure 2.1 – a) (2D projected) crystalline SiO_2 structure; b) amorphous SiO_2 structure; c) a double-well potential built up from two harmonic-oscillator wells.

To find the energy levels of a particle moving in a double-well potential V of the form shown in Fig.2.1c one can start with the solution of the single-well problem. This is known as the *well, non-diagonal or coordinate* QM representation. These two states are the ground states of the relevant harmonic potential wells V_1 and V_2, they are shown continued as dashed lines in Fig. 2.1c.

Fig. 2.1c shows a schematic representation of the potential:

$$V(x) = \begin{cases} V_1(x) = \gamma(x+l)^2 + \Delta\,, \text{when } x \leq -\dfrac{\Delta}{4\gamma l} \\ V_2(x) = \gamma(x-l)^2\,, \qquad \text{other.} \end{cases} \tag{2.1}$$

Δ is the potential's asymmetry, V_B is the potential barrier, m is the mass of the (fictitious, as we shall see) "particle", γ, l are constants, and $\frac{\hbar\omega_0}{2}$ is the lowest ground-state energy of the oscillator in the single-well.

The simple unperturbed Hamiltonian H_0 of each independent tunneling system is formulated in matrix form as follows, in order to generalize to arbitrary double-well potentials, in the position-, or well-representation (and an overall constant apart):

$$H_0 = -\frac{1}{2}\begin{pmatrix} \Delta & \Delta_0 \\ \Delta_0 & -\Delta \end{pmatrix} \tag{2.1}$$

There is a formal analogy between the 2LS and a particle with spin 1/2 in a magnetic field. The states $|l\rangle$ and $|r\rangle$ correspond to different signs of the spin projection on the magnetic field vector. Then, using the Pauli matrices $\sigma_x, \sigma_y, \sigma_z$, the Hamiltonian H_0 of Eq. (2.2) can be written in terms of spin operators:

$$H_0 = -\frac{1}{2}(\Delta\sigma_z + \Delta\sigma_x) \tag{2.3}$$

These are referred to as pseudo-spin operators.

Δ_0 can be evaluated explicitly for specific toy potentials. Within the quasi-classical WKB approximation the tunnelling splitting can be written as:

$$\Delta_0 = \hbar\omega_0 e^{-\lambda}, \text{ where } \lambda = \frac{d\sqrt{2mV_B}}{\hbar} \tag{2.4}$$

Here V_B is the minimum energy barrier between the two wells, $\hbar$ is the Planck constant, d is the separation between the two minima. Roughly speaking the tunneling splitting Δ_0 is given by the vibrational energy $\hbar\omega_0$ of the particle multiplied by the probability $exp(-\lambda)$ for tunneling. λ is a tunneling parameter, which reflects the overlap of the wave functions of the "particle" from both sides of the potential barrier.

The matrix (2.2) can be diagonalized to obtain the energy of the ground and excited states of the double-well potential, the eigenstates in *diagonal* or *energy* representation. The eigenfunctions $E_{1,2}$ will be:

$$E_{1,2} = \pm\frac{1}{2}\sqrt{\Delta^2 + \Delta_0^2} \tag{2.5}$$

The energy difference between ground and excited states is named energy gap or excitation energy of the 2LS and corresponds to the following expression:

$$E = \sqrt{\Delta^2 + \Delta_0^2} \tag{2.6}$$

When the glass is cooled from the melt, its atoms or ions form a potential energy landscape in which the characteristic parameters of the manifest double well-potentials (V_B, m, l and Δ) are spread wide. The STM assumes that the asymmetry energy Δ and the tunneling parameter λ are independent of each other and uniformly distributed according to a broad probability distribution function

$$P(\Delta, \lambda) d\Delta d\lambda = \overline{P} d\Delta d\lambda \tag{2.7}$$

where $\overline{P}$ is a material-dependent constant, proportional to the volume concentration of 2LS and must be determined experimentally. For many of the dielectric glasses its value is of the order of ~10^{45} $J^{-1}m^{-3}$, but it varies widely. Using the expression (2.4), we can rewrite the distribution function (2.7) as a function of Δ and Δ_0:

$$P(\Delta, \Delta_0) d\Delta d\Delta_0 = \frac{\bar{P}}{\Delta_0} d\Delta d\Delta_0 \tag{2.8}$$

However, not all states of the parameter space (Δ, Δ_0) count. Using the expression (2.6) and its Jacobian matrix, one can convert the above distribution function to a distribution in terms of the tunneling splitting Δ_0 and energy E:

$$P(E, \Delta_0) dE d\Delta_0 = \bar{P} \frac{E}{\Delta_0} \frac{1}{\sqrt{E^2 - \Delta_0^2}} dE d\Delta_0 \tag{2.9}$$

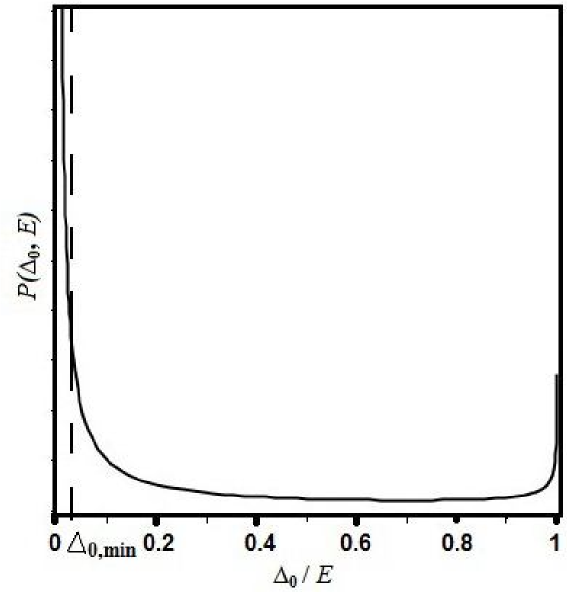

Figure 2.2 – Distribution function (2.9) as a function of Δ_0/E .

As seen from (2.9), the distribution function becomes infinity, when $\Delta_0 = 0$. The other singularity at $\Delta_0 = E$ is integrable. In this situation it is convenient to introduce a minimal tunneling splitting Δ_{0min} and (eventually) a maximum energy splitting E_{max} .

The tunneling systems (TS) couple to their environment by interacting with both phonons and photons. External elastic and electric fields change the asymmetry energy Δ and induce relaxation processes.

The time required for changing the system from a perturbed state to the equilibrium state is called the relaxation time. The inverse of the relaxation time is the relaxation rate and is found to be given by the one-phonon scattering formula: [2.4]

$$\tau^{-1} = \left(\frac{\gamma_l^2}{v_l^5} + 2\frac{\gamma_t^2}{v_t^5}\right)\frac{\Delta_0^2 E}{2\pi\hbar^4}\coth\left(\frac{E}{2k_B T}\right) \qquad (2.10)$$

Here $\gamma_{l,t}$ are deformation potentials, $v_{l,t}$ is the speed of sound in glass, k_B is Boltzmann’s constant. The indices "l" and "t" denote the longitudinal and transverse phonon branches. The distribution function (2.9) as a function of energy E and relaxation times τ, using a Jacobian transformation, now reads as:

$$P(E,\tau) = \frac{\overline{P}}{2\tau\sqrt{1-\frac{\tau_{min}(E)}{\tau}}} \qquad (2.11)$$

The shortest relaxation time τ_{min} is obtained for symmetric TS (Δ=0), where the tunnel splitting Δ_0 is equal to the energy splitting E. Systems with the smallest tunnel splitting Δ_{0min} have the longest relaxation time τ_{max}:

$$\tau_{min}(E) = \frac{\gamma}{E^3}\tanh\left(\frac{E}{2k_B T}\right) \qquad (2.12a)$$

$$\tau_{max}(E) = \frac{\gamma}{\Delta_0^2 E}\tanh\left(\frac{E}{2k_B T}\right) \qquad (2.12b)$$

Here, $\gamma = 2\pi\rho\hbar^4\left(\frac{\gamma_l^2}{v_l^5} + 2\frac{\gamma_t^2}{v_t^5}\right)^{-1}$ is an elastic material parameter of the solid.

2.2 Dielectric properties.

To measure the frequency-dependent dielectric properties of the cold glasses one applies an ac electric field to the sample, typically at radio frequencies (RF). The tunneling systems then couple to this field via the electric charge or dipole moment of the tunneling “particle”. The applied electric field both modulates the energy splitting of the tunneling states and excites them from thermodynamic equilibrium. The electric field only affects the asymmetry energy Δ [2.12]. The influence of the electric field on the tunnel splitting Δ_0 is usually neglected [2.13]. The coupling to the external field therefore causes resonant processes like resonant absorption and stimulated emission.

In the presence of the external electric field F the Hamiltonian matrix takes the form (coordinate representation):

$$H = H_0 + \vec{p}_0\vec{F}\sigma_z = -\frac{1}{2}\begin{pmatrix} \Delta - 2\vec{p}_0\vec{F} & \Delta_0 \\ \Delta_0 & -\Delta + 2\vec{p}_0\vec{F} \end{pmatrix} \tag{2.13}$$

Here $\vec{p}_0$ denotes the electric dipole moment of the fictitious particle, $\vec{F} = \vec{F}_\omega \cos\omega t$ is the time-dependent electric field. Diagonalizing the Hamiltonian (2.13) one can get (energy representation):

$$H = -\begin{pmatrix} \frac{1}{2}E & 0 \\ 0 & \frac{1}{2}E \end{pmatrix} + \begin{pmatrix} \frac{\Delta}{E} & \frac{\Delta_0}{E} \\ \frac{\Delta_0}{E} & -\frac{\Delta}{E} \end{pmatrix} \vec{p}_0\vec{F}\cos\omega t \tag{2.14}$$

The dynamics of the two-level systems is given by the change in the expectation values through the Bloch equations, which were first derived by Bloch in the context of magnetic resonance [2.14]:

$$\begin{aligned} \frac{dS_x}{dt} &= -\frac{1}{\tau_2}S_x + \tilde{\gamma}\left(S_yB_z - S_zB_y\right) \\ \frac{dS_y}{dt} &= -\frac{1}{\tau_2}S_y + \tilde{\gamma}(S_zB_x - S_xB_z) \\ \frac{dS_z}{dt} &= -\frac{1}{\tau_1}(S_z - \langle S_z\rangle) + \tilde{\gamma}\left(S_xB_y - S_yB_x\right). \end{aligned} \tag{2.15}$$

Here we have introduced the pseudo-spin ½ operator $\boldsymbol{S} = \boldsymbol{\sigma}/2$, where $\boldsymbol{\sigma}$ are Pauli's matrices (in the TS energy representation), τ_1 is a characteristic time for the equilibration of the level populations of the two-level systems (2LS), and τ_2 is the transverse dephasing time due to spin-spin (i.e. 2LS-2LS) interactions. Also, $\langle S_z\rangle$ is the thermal equilibrium value of S_z given by $\langle S_z\rangle = \tanh(\tilde{\gamma}\hbar B_z(t)/2k_BT)/2$, $\tilde{\gamma}$ is the appropriate (fictitious) gyromagnetic ratio and $\boldsymbol{B} = \boldsymbol{B}_{dc} + \boldsymbol{B}_{ac}$ is a fictitious effective field made up of a static (dc) part and of an oscillating (ac) one proportional to the electric field with frequency ω. The dimensionless spin ***S*** processes around this fictitious effective field ***B***, given by

$$\mu\vec{B} = \left(\frac{2\Delta_0}{E}\vec{p}_0\vec{F}, 0\; E + \frac{2\Delta}{E}\vec{p}_0\vec{F}\right).$$

Since the ac field is a small perturbation, one can expand $\langle S_z\rangle$ in a Taylor series by keeping terms up to the first order in $\boldsymbol{B}_{ac}$. The solution to the Bloch equations takes the form $(t) = S^0(t) + S^1(t)$, where $S^0(t)$ is of zeroth order and $S^1(t)$ is of first order in $\boldsymbol{B}_{ac}$. Thus the linearised Bloch equations become, for the zero-order and first-order contributions, respectively, to the S-components:

$$\frac{dS_z^0}{dt} + \frac{1}{\tau_1}[S_z^0(t) - S_z^0(\infty)] = 0,$$

$$\frac{dS_x^1}{dt} - \omega_0 S_y^1 + \frac{1}{\tau_2}S_x^1 = 0,$$

$$\frac{dS_y^1}{dt} + \omega_0 S_x^0 + \frac{1}{\tau_2} S_y^1 - \delta\alpha S_z^0(t)\cos\omega t = 0,$$

$$\frac{dS_z^1}{dt} + \frac{1}{\tau_1}\left(S_z^1 - \delta\alpha S_z^0(t)\cos\omega t\right) = 0 \qquad (2.16)$$

where we introduced the resonance frequency $\omega_0 = \tilde{\gamma} B_{z,dc} = -E/\hbar$, which depends on the level splitting, $\delta = -(2\Delta/\hbar E)p_0 F_\omega \cos\theta$ which is a first-order term in the ac field F_ω, θ being the angle between the ac field and the dipole moment. $S_z^0(0)$ is the initial value of $S_z^0(t)$ shortly after the field is applied, $S_z^0(\infty) = -\tanh(E/2k_BT)/2$ is the equilibrium value of the aligned spin, $\alpha = \Delta_0/\Delta$, and we define $\lambda = \hbar\left[1 - 4\left(S_z^0(\infty)\right)^2\right]/4k_BT$. If one introduces raising and lowering operators $S^\pm = S_x^1 \pm iS_y^1$, then the equations for S^+ and S^- separate. The equations for S^+ becomes:

$$\frac{dS^+(t)}{dt} + i\left(\omega_0 - \frac{i}{\tau_2}\right)S^+(t) - i\alpha\delta S_z^0(t)\cos\omega t = 0 \qquad (2.17)$$

and the equations for S^- is the complex conjugate of the above.

The solutions of these equations are given by the following expressions [2.15]:

$$S_z^0(t) = S_z^0(\infty) + [S_z^0(0) - S_z^0(\infty)]e^{-t/\tau_1} ,$$

$$S_z^1(t) = \frac{\delta\lambda}{1+\tau_1^2\omega^2}[\cos\omega t + \tau_1\omega \sin\omega t] , \qquad (2.18)$$

$$S^+(t) = \frac{\delta\alpha[(\omega_0 - i/\tau_2)\cos\omega t - i\omega \sin\omega t]S_z^0(\infty)}{(\omega_0 - i/\tau_2)^2 - \omega^2} + \frac{\delta\alpha[(\omega_0 + i/\tau_1 - i/\tau_2)\cos\omega t - i\omega \sin\omega t]\left[S_z^0(0) - S_z^0(\infty)\right]e^{-t/\tau_1}}{(\omega_0 + i/\tau_1 - i/\tau_2)^2 - \omega^2}.$$

the result for $S^-(t)$ being the complex conjugate of the equation for $S^+(t)$.

The Bloch spins should now be related to the 2LS polarization in the electric field direction. The component $p_\parallel$ of the dipole moment along the direction of the electric field, in the diagonal basis as in Eq. (2.14), is now given by $p_\parallel = -\langle \frac{\Delta}{E}\sigma_z + \frac{\Delta_0}{E}\sigma_x \rangle p_0 \cos\theta$ and using the average values of $\langle\sigma_z\rangle$ and $\langle\sigma_x\rangle$ from the solutions of the Bloch equations one can obtain the dipole moment in the energy representation [2.15]:

$$p_\parallel = -p_0 \cos\theta \left(\frac{2\Delta S_z^1(\mathrm{t})}{\mathrm{E}} + \frac{\Delta_0(\mathrm{S}^+ + \mathrm{S}^-)}{\mathrm{E}}\right) \qquad (2.19)$$

Then, one must insert the deduced pseudo-spin values $S_z(t)$, $S^+(t)$ and $S^-(t)$,Eq. (2.18) to (2.19). Equation (2.19) depends of electric field F_ω linearly and can be easily differentiated with respect to the electric field, and this gives a formula for the dielectric constant $\epsilon = \left.\frac{dp_\parallel}{dF_\omega}\right|_{F_\omega = 0}$. For convenience one may separate the resulting formulae writing $\epsilon = (\epsilon'_{RES} + \epsilon'_{REL}) + i(\epsilon''_{RES} + \epsilon''_{REL})$. These are the real (ϵ') and imaginary (ϵ'') parts of the dielectric constant. The imaginary part is interpreted as a dielectric loss (loss tangent, $\tan\delta = \epsilon''/\epsilon'$) - a parameter of the dielectric material that quantifies its inherent dissipation of electromagnetic energy (much like in a RLC circuit). One gets:

$$\epsilon'_{RES} = \frac{{p_0}^2 \cos^2\theta}{\hbar}\left(\frac{\Delta_0}{E}\right)^2 \left[\left(\frac{(\omega_0+\omega)\tau_2^2}{1+(\omega_0+\omega)^2\tau_2^2} + \frac{(\omega_0-\omega)\,\tau_2^2}{1+(\omega_0-\omega)^2\tau_2^2}\right)\tanh\left(\frac{E}{2k_{BT}}\right) - \left(\frac{(\omega_0+\omega)\tau_{12}^2}{1+\tau_{12}^2(\omega_0+\omega)^2} + \frac{(\omega_0-\omega)\tau_{12}^2}{1+\tau_{12}^2(\omega_0-\omega)^2}\right)\left(2\,\mathrm{S}_\mathrm{z}^0(0) + \tanh\left(\frac{E}{2k_{BT}}\right)\right)e^{-t/\tau_1}\right] \tag{2.20a}$$

$$\epsilon''_{RES} = \frac{{p_0}^2 \cos^2\theta}{\hbar}\left(\frac{\Delta_0}{E}\right)^2 \left[\left(\frac{\tau_2}{1+(\omega_0-\omega)^2\tau_2^2} - \frac{\tau_2}{1+(\omega_0+\omega)^2\tau_2^2}\right)\tanh\left(\frac{E}{2k_{BT}}\right) + \left(\frac{\tau_{12}}{1+\tau_{12}^2(\omega_0+\omega)^2} - \frac{\tau_{12}}{1+\tau_{12}^2(\omega_0-\omega)^2}\right)\left(2\,\mathrm{S}_\mathrm{z}^0(0) + \tanh\left(\frac{E}{2k_{BT}}\right)\right)e^{-t/\tau_1}\right] \tag{2.20b}$$

$$\epsilon'_{REL} = \frac{{p_0}^2 \cos^2\theta}{k_B T}\left(\frac{\Delta}{E}\right)^2 \cosh^{-2}\left(\frac{E}{2k_B T}\right)\frac{1}{1+\tau_1^2\omega^2} \tag{2.20c}$$

$$\epsilon''_{REL} = \frac{{p_0}^2 \cos^2\theta}{k_B T}\left(\frac{\Delta}{E}\right)^2 \cosh^{-2}\left(\frac{E}{2k_B T}\right)\frac{\tau_1\omega}{1+\tau_1^2\omega^2}\,, \tag{2.20d}$$

where $\tau_{12}^{-1} = \tau_2^{-1} - \tau_1^{-1}$. In the adiabatic limit the initial value of the pseudo-spin is $\mathrm{S}_\mathrm{z}^0(0) = -\tanh\left(\mathrm{E}/2\mathrm{k_B T}\right)/2$, when the 2LS eigenvalues are $\pm\frac{1}{2}E$. That makes the time dependent terms of (2.20a) and (2.20b) equal to 0 shortly after applying the field.

For an ensemble of 2LS, from the manipulation of the Bloch equations for the motion of the spatial components of a pseudo-spin 1/2 under periodic electric and elastic perturbations and taking into account the phonon relaxation mechanism, one then finds the explicit form of the expression for the dielectric constant [2.16]:

$$\epsilon = \epsilon_{RES} + \epsilon_{REL}\frac{1}{1+i\omega\tau} = \left(\epsilon_{RES} + \epsilon_{REL}\frac{1}{1+\omega^2\tau^2}\right) - i\epsilon_{REL}\frac{\omega\tau}{1+\omega^2\tau^2}$$

The typical energy splittings of the TS in low temperature experiments correspond to frequencies in the range of $\frac{\omega_0}{2\pi} \approx 10^8\mathrm{Hz}$, when the electric field frequency ω is about 10^3 Hz. This justifies a low-frequency approximation $\omega \ll \omega_0$. To obtain the resonant part we can also set $\tau_2^{-1} = 0$, which simplifies expressions (2.20a) and (2.20b), remembering that $E = \hbar\omega_0$. From the averaging over the dipole orientation angle θ comes a prefactor 1/3: $\overline{p_0^2 \cos^2\theta} = \frac{1}{3}\overline{p_0^2}$, where $\overline{p_0^2}$ is the configurationally averaged square 2LS electric-dipole moment.

The real part of the relative dielectric constant for 2LS shows the temperature-dependent contributions ($\epsilon(T) = \epsilon'(0) + \Delta\epsilon'(T)$, with $|\Delta\epsilon'| \ll \epsilon'$):

$$\left.\frac{\Delta\epsilon'}{\epsilon'}\right|_{2LS\;RES} = \frac{2}{3}\overline{p_0^2}\frac{\Delta_0^2}{E^3}\tanh\left(\frac{E}{2k_B T}\right) \tag{2.21}$$

$$\left.\frac{\Delta\epsilon'}{\epsilon'}\right|_{2LS\;REL} = \frac{1}{3k_B T}\overline{p_0^2}\frac{\Delta^2}{E^2}\cosh^{-2}\left(\frac{E}{2k_B T}\right)\frac{1}{1+\omega^2\tau^2} \tag{2.22}$$

The equation (2.21) corresponds to the resonant tunneling contribution to the dielectric constant, and (2.22) is the relaxational contribution. We neglect for now, for low ω, the frequency dependence in the RES part so long as $\omega \ll \omega_0$.

The dielectric loss is described by the following formula (the resonant contribution being vanishingly small):

$$\Delta\tan\delta|_{2LS\ REL} = \left.\frac{\Delta\epsilon''}{\epsilon'}\right|_{2LS\ REL} = \frac{1}{3k_BT}\overline{p_0^2}\,\frac{\Delta^2}{E^2}\cosh^{-2}\left(\frac{E}{2k_BT}\right)\frac{\omega\tau}{1+\omega^2\tau^2} \tag{2.23}$$

Integrating equations (2.21-2.23) over the parameter distribution of the 2LS and over the dipole orientation angle θ , using functions (2.9, 2.11), one can find the temperature-dependent contributions to the dielectric constant and dielectric loss:

$$\left.\frac{\Delta\epsilon'}{\epsilon'}\right|_{2RES} = \frac{2\overline{P}\overline{p_0^2}}{3\epsilon_0\epsilon_r}\int_{\Delta_{0,min}}^{E_{max}}\frac{dE}{E}\tanh\left(\frac{E}{2k_BT}\right)\sqrt{1-\left(\frac{\Delta_{0,min}}{E}\right)^2}, \tag{2.24}$$

$$\left.\frac{\Delta\epsilon'}{\epsilon'}\right|_{2REL} = \frac{\overline{P}\overline{p_0^2}}{3\epsilon_0\epsilon_r k_BT}\int_{\Delta_{0,min}}^{E_{max}} dE\int_{\tau_{min}(E)}^{\tau_{max}(E)}\frac{d\tau}{\tau}\sqrt{1-\frac{\tau_{min}(E)}{\tau}}\cosh^{-2}\left(\frac{E}{2k_BT}\right)\frac{1}{1+\omega^2\tau^2}, \tag{2.25}$$

$$\left.\frac{\Delta\tan\delta}{\epsilon'}\right|_{2REL} = \frac{\overline{P}\overline{p_0^2}}{3\epsilon_0\epsilon_r k_BT}\int_{\Delta_{0,min}}^{E_{max}} dE\int_{\tau_{min}(E)}^{\tau_{max}(E)}\frac{d\tau}{\tau}\sqrt{1-\frac{\tau_{min}(E)}{\tau}}\cosh^{-2}\left(\frac{E}{2k_BT}\right)\frac{\omega\tau}{1+\omega^2\tau^2}. \tag{2.26}$$

If one extends, when appropriate and as a further approximation, the integration limits ($E_{max} \to \infty$ and $\Delta_{0,min} \to 0$), then calculating the E-integral one gets a characteristic logarithmic variation of the real part of the dielectric constant as a function of temperature:

$$\left.\frac{\Delta\epsilon'}{\epsilon'}\right|_{2RES} \approx \begin{cases} -\frac{2\overline{P}\overline{p_0^2}}{3\epsilon_0\epsilon_r}\ln\left(\frac{T}{T_0}\right), & T < \frac{\Delta_{0max}}{2k_B} \\ 0, & T > \frac{\Delta_{0max}}{2k_B} \end{cases} \tag{2.27}$$

For $\omega\tau_{min} \gg 1$ and at low temperatures, the contribution from relaxation to the real part as compared to the resonant contribution is negligible. Under the condition $\omega\tau_{min} \ll 1$, however, the term $d\tau/\tau$ dominates in the integral and we obtain again a logarithmic variation with temperature:

$$\left.\frac{\Delta\epsilon'}{\epsilon'}\right|_{2REL} \approx \begin{cases} 0, & \omega\tau_{min} \gg 1 \\ \frac{1\overline{P}\overline{p_0^2}}{3\epsilon_0\epsilon_r}\ln\left(\frac{T}{T_0}\right), & \omega\tau_{min} \ll 1 \end{cases} \tag{2.28}$$

A crossover between the resonant (low temperature) and relaxation (high T) regimes occurs at a characteristic temperature [2.16]

$$T_0(\omega) = \frac{1}{k_B}\sqrt[3]{\frac{\omega\pi\rho\hbar^4}{\gamma_l^2/v_l^5 + 2\gamma_t^2/v_t^5}} \tag{2.29}$$

which for a thermal 2LS with $E = \Delta = k_BT$ satisfies the condition $\omega\tau(T_0) = 1$

Eqs. (2.27-2.28) show that with increasing temperature the T dependence changes from a decrease in the resonant regime to an increase in the relaxation one. At the temperature $T_0(\omega)$ there is a minimum. Thus, the sum of the two contributions has a characteristic V-shaped form, in a semi-logarithmic plot, with the minimum occurring at a T_0 roughly given by the condition $\tau_{min}(k_BT_0) \cong 1$, or $k_BT_0(\omega) \cong \left(\frac{1}{2}\gamma\omega\right)^{1/3}$. $\epsilon_0\epsilon_r$ is here the bulk of the solid's dielectric constant and we see that a −2:1 characteristic behavior is predicted by the STM with the slope for $T > T_0$ given by (2.28). This behavior is indeed observed in pure a-SiO$_2$ [2.17]. However in most multi-component glasses (chemically made up of good glass formers as well as of good crystal formers, for example a-Al$_2$O$_3$-BaO-SiO$_2$) it is rather a V-shaped curve with a (roughly) −1:1 slope ratio that is often observed.

2.3 Heat capacity

At low-temperatures the specific heat observed in glasses has the same (universal) characteristic temperature dependence. Introducing the density of 2LS states $n(E)$ it is simple to calculate the heat capacity of these localised 2LS states:

$$C = k_B \int_0^\infty n(E) \left\{ \left(\frac{E}{2k_BT}\right)^2 \cosh^{-2}\left(\frac{E}{2k_BT}\right) \right\} \tag{2.30}$$

In the seminal papers [2.4, 2.5] one supposes that $n(E)$ is a slowly-varying continuous function of E, and $(0) \neq 0$. This reduces to a linear dependence for the heat capacity on temperature:

$$C \propto \frac{\pi^2}{6} k_B^2 T n(0) \tag{2.31}$$

For the heat capacity of glasses one should also take into account the Debye-type contribution of the acoustic (long wavelengths, oblivious to disorder) phonons, which is proportional to the temperature in power three:

$$C_{Debye} \sim \frac{N k_B 12\pi^4}{5} \left(\frac{T}{T_D}\right)^3, \tag{2.32}$$

where N is the number of atoms, T_D is the Debye temperature $T_D = \frac{hc_S}{2k_B} \sqrt[3]{\frac{6}{\pi}\frac{N}{V}}$, and c_S is the effective sound velocity. The Debye formula, originally derived for a crystal, applies also to the glasses because only very low wavelengths contributions from the acoustic phonons are involved, and these are oblivious to the solid's structure.

2.4 Sound velocity

At low temperatures, when $\omega\tau_{min} \gg 1$, the internal friction Q decreases as the third power of temperature, and the sound velocity v is expected to vary logarithmically with temperature too, as [2.18, 2.19]

$$Q^{-1} = \frac{\pi^2 C \gamma^2 k_B^2 T^2}{24\hbar\omega} \tag{2.33}$$

$$\frac{\delta v}{v} = C \ln\left(\frac{T}{T_0}\right), \tag{2.34}$$

where T_0 is a new characteristic reference temperature, and the parameter C is given by $C = \overline{P}\gamma_i^2/\varrho v_i^2$; the index i standing for longitudinal or transverse polarization. At higher temperatures, when $\omega\tau_{min} \ll 1$, the internal friction approaches the value [2.18]

$$Q^{-1} = \frac{\pi}{2}C\,, \tag{2.35}$$

independent of temperature and frequency. The sound velocity has an inverted V-shaped semi-logarithmic dependence, passing through a maximum and then decreasing logarithmically with increasing temperature as (for $T>T_0$):

$$\frac{\delta v}{v} = -\frac{C}{2}\ln\left(\frac{T}{T_0}\right) \tag{2.36}$$

Thus, it is believed that the sound velocity anomaly is also due to a direct coupling of the 2LS to the thermal phonons in the cold glasses.

Other experiments reveal the existence and pseudo-spin like nature of the TS in glasses below 1 K, one of the most noteworthy being the **dipole, or polarization echo** which will be discussed in a separate chapter at the end.

2.5 Realistic glassy energy landscape

As was stated before, many properties of glass-forming materials can be explained in terms of their multi-dimensional potential energy landscape (at low T; at higher T one needs the free energy). *Qualitatively (pictorially)*, the energy landscape of glass-forming systems is usually drawn as a 1D potential containing a large number of hills and valleys as shown in Fig. 2.3 and Fig. 2.4 [2.20]. Looking at Fig. 2.3 one can choose any two nearest well with different depth and energy barrier between them. It will be a local double-well potential, or 2LS, as already shown in Fig. 2.1.

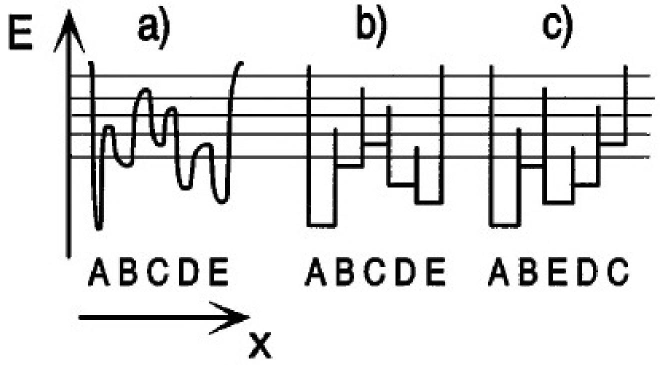

Figure 2.3 – a) A simple 1D energy landscape, (b) a schematic representation of (a), (c) the potential minima are rearranged. The horizontal lines are discussed in the text of Ref [2.20].

In his seminal work [2.20] Heuer calculated numerically the energy landscape of a model system of 32 Lennard-Johnes (LJ) particles with simulated densities 1 and 1.075. He found 367 minima with different energy for ρ=1 and 75 for ρ = 1.075. In Fig. 2.4 this schematic potential is reproduced for the energy landscape of the LJ glass with ρ =1. On the left far side one can see the isolated crystalline minimum. A very high energy has to be reached before the crystal can "melt". Heuer **defines** a 2LS as adjacent pairs of minima k_1 and k_2 such that the energy at its saddle is smaller than the energy of all other saddles which can be reached either from minimum k_1 or k_2 (see, e.g., minima D and E in Fig. 2.3). This condition guarantees that at low temperatures the system can switch between both minima without escaping to a third minimum. Double-well potentials are marked by squares. Here are found 7 2LS for 223 minima, one has thus a probability of 14/223 per minimum that it belongs to a 2LS. The density of states in Heuer's numerical work has been found to be $2 \times 10^{46}\ \mathrm{J}^{-1}\mathrm{m}^{-3}$, that is of the right order of magnitude if compared with experimental data on molecular or metallic glasses. But the 2LS is an oversimplified representation of the model LJ glass. It is in fact possible to find three or more wells grouped together and with relatively close energy minima.

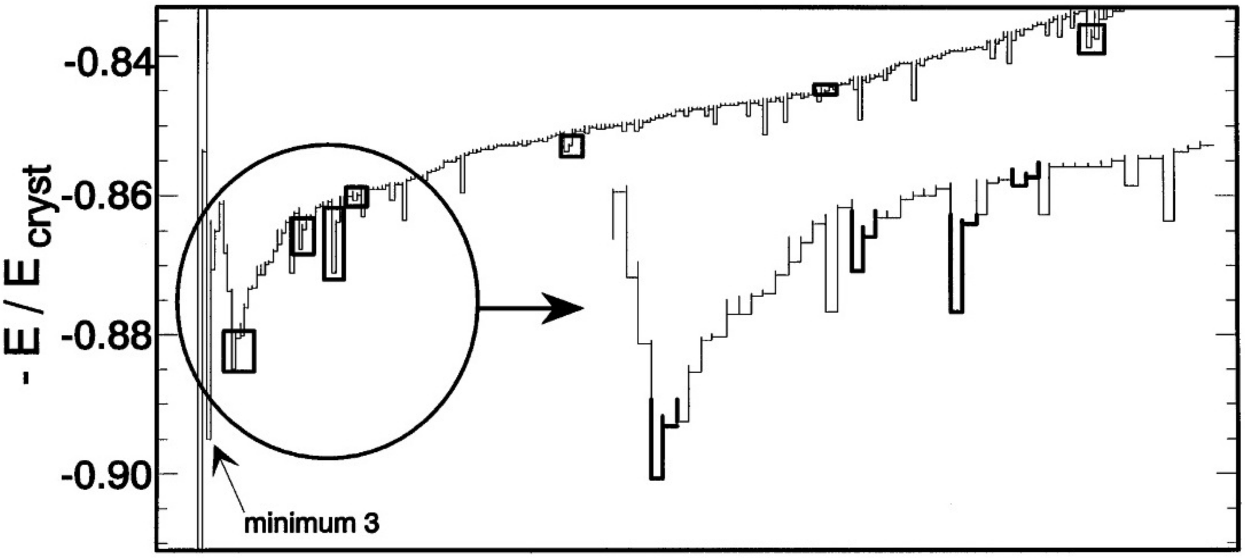

Figure 2.4 – The energy landscape for a LJ glass calculated numerically by Heuer [2.20]

There is a number of experiments with the low temperature glasses, which can be used to verify the hypothesis of the tunneling states, and especially of the 2LS tunneling model: sound velocity, dielectric permittivity, heat capacity and phonon heat conductivity, dipole-echo experiment and so on. However, all this experiments are made in the presence of electric and magnetic fields and are performed by different types of experimental equipment. Owing to the sol-gel fabrication process, through which one usually prepares thick-film samples of the glass, these samples can (partially) devitrify after some time, the **devitrification** being favoured by the presence of different concentrations of impurities (Fe, OH, …) There are, on the other hand, important nonlinearity effects due to the high electric field magnitude employed in the experiments (non-linear response is measured, but linear-response is used in the theory). All these non-ideal features result in discrepancies between the estimated STM parameters for the different experiments. It should be stressed - in fact – that, in spite of its simplicity and relative success in explaining data, the 2LS STM still has many shortcomings. Such as: a strong variability of the various model's parameters (needed to produce reasonable fits) from experiment to experiment for the very same glassy material. Moreover, the model's parameters vary as different temperature- or frequency- (etc.) ranges are explored. All this points to the STM (especially in the 2LS form) as being just a crude phenomenological model; a good critique has been published by C. Yu and Leggett [2.21]. The restriction to only two wells, in particular - that is a spin-1/2 pseudo-spin degree of freedom - seems a convenient but unrealistic limitation. Despite some other interesting earlier and more recent attempts (the model of Fulde and Wagner [2.22], the Russian School approach [2.23], the Soft-Potential model [2.23], Kuehn's quantum-mechanical model [2.24], Carruzzo et al.'s interacting-defects model [2.15], the elastic dipole model of Grannan, Randeira and Sethna [2.25], the free-volume model of Cohen and Grest [2.26], etc.…) the 2LS STM remains, however, the most popular approach for the explanation of the low-temperature properties of glasses.

In Table 2.1 we list the STM parameters Δ_{0min}, E_{max}, $\bar{P}$ for the most investigated glasses, as found in the literature.

Table 2.1 – Material parameters for the 2LS STM in the literature.

Reference	**Material**	**Δ_{0min}, mK**	**E_{max} , K**	$\bar{P}$, J^{-1} m^{-3}
a	SiO_2	$2x10^{-3}$,$2x10^{-7}$	4	10^{45}
b	Suprasil W			$2.2x10^{44}$
c	SiO_x, 5kHz, 500 V/m	3.3	10	
d	Suprasil	4		
e	Alpha-SiO_2, 90 kHz	6.6		
f	Suprasil 1	3		$1.39x10^{45}$
	Suprasil 300	1		$0.92 x10^{45}$
	Suprasil 310	3		$1.1 x10^{45}$
	Suprasil W	2		$0.98 x10^{45}$

g	Al_2O_3-BaO-SiO_2 (BAS)	2.0±1.0		1.2x10^{45}
h i	BAS 1 kHz, 15 kV/m	12.2	5	10^{45}
j	BK7	~10^{-5} ,10^{-2}		
k	BK7	1.5±1.2		2.3x10^{45}
c	BK7, 5 kHz, 200V/m	2.2		
l	BK7	16		
m	BK7, 1 kHz, 75 V/m	3	10	$\bar{P}p_0^2$=1.28x10^{13} C/Jm
n	Duran	1.5±1.0		1.57x10^{45}
c	5%K:SiO_2 5kHz, 500 V/m	1.3	10	
	$(KBr)_{1-x}(KCN)_x$			
o	x=0.2			0.83x10^{45}
p	x=0.25			4.00x10^{45}
q				3.10x10^{45}

a) Carruzzo H., Grannan E. R. and Yu C. C., Phys. Rev. B **50**, 6685 (1994).
b) Black J. L., Halperin B. I., Phys. Rev. B **16,** 2879 (1977).
c) Rogge S., Natelson D., Tigner B. and Osheroff D. D., Phys. Rev. B **55**, 11256 (1997).
d) van Rooijen R., Marchenkov A., Akimoto H. and Jochemsen R., J. Low Temp. Phys. **110**, 269-274 (1998).
e) Thompson EunJoo, Lawes G., Parpia J. M. and Pohl R. O., Phys. Rev. Lett. **84**, 4601 (2000).
f) Meissner M., Strehlow P., J. Low Temp. Phys. **137** (2004).
g) Seibert L., Ph.D. Thesis Heidelberg University (2001).
h) Strehlow P. and Wohlfahrt M., Jansen A. G. M., Haueisen R. and Weiss G., Enss C. and Hunklinger S., Phys. Rev. Lett. **84**, 1938 (2000); Wohlfahrt M., Ph.D. Thesis Heidelberg University (2001).
i) Kettemann S., Fulde P., Strehlow P., Phys. Rev. Lett. **83**, 4325 (1999).
j) Burin A. L., Natelson D., Osheroff D. D. and Kagan Y. In: Esquinazi P., Editor, Tunneling Systems in Amorphous and Crystalline Solids, Springer, Berlin , p. 223 (1998).
k) Hunklinger S., Arnold W. In: Thurston R. N. and Mason W. P., Editors, Physical Acoustics – Vol. **12**, p. 155 (1976).
l) Lasjaunias J. C., Maynard R. and Vandorpe M., Journal de Physique Colloque **39**, C6 973 (1978).
m) Strehlow P., Physica B **329–333**, p. 1243–1244 (2003).
n) Schilling K., 2. Int. Koll. der Hochschule fur Elektrotechnik, Illmenau p. 101 (1958).
o) Foote M. C., Golding B., Phys. Rev. B **43**, 9206 (1991).
p) De Yoreo J. J., Knaak W., Meissner M., Pohl R. O., Phys. Rev. B **34**, 8828 (1986).
q) Berret J. F. and Meissner M. In: Phonon Scattering in Condensed Matter V, edited by Anderson A.C. and Wolfe J.P., Springer Series in Solid-State Sciences Vol. **68** (Springer-Verlag, Berlin, 1986).

Chapter 3

Nature of the tunneling systems

One of the most well-known method for preparing an amorphous solid involves the cooling of a viscous liquid below its thermodynamic-equilibrium freezing point T_f, through a metastable supercooled regime, and finally below a "glass transition" temperature T_g $(T_g<T_f)$. The very fast cooling of the liquid does not make possible the arrangement of all atoms in perfect crystal cells. To understand the basic phenomena related to supercooling and glass formation, it is useful to take a "topographic" view of the potential energy function, a function that depends on the spatial location of each particle. Figure 3.1 shows a highly schematic illustration of the multi-dimensional landscape in a 1D representation. The minima correspond to mechanically (but not necessarily thermodynamically) stable arrangements of the particles in space. Any small displacement from such an arrangement gives rise to restoring forces to the changed arrangement. The lowest lying minima correspond to the crystal phases (there might be more than one). Higher lying minima correspond to amorphous particle packing and are sampled by the stable liquid phase above the melting/freezing temperature.

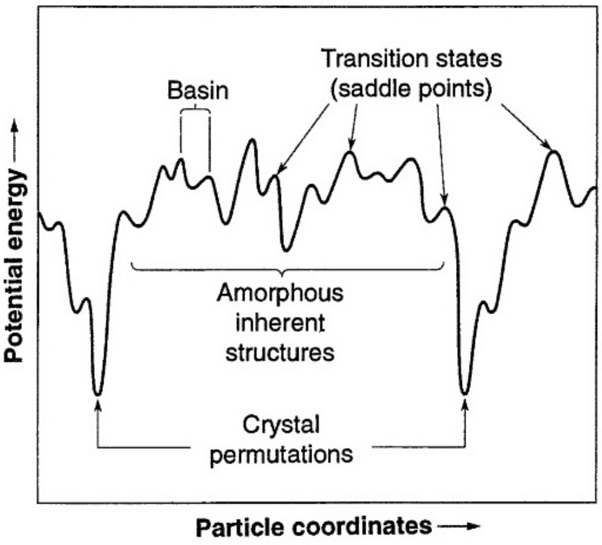

Fig. 3.1 – Schematic 1D diagram of the potential energy surface in the multidimensional configuration space for a many-particle system [3.1].

In some seminal papers, Heuer [3.2, 3.3] presents a numerical simulation procedure which is able to describe the low-energy excitations in a model glass on a microscopic level and calculate the total potential energy landscape of a small glass-forming system. There, Heuer describes a quantitative method which finds the tunneling systems in glasses and hence allows for a microscopic backing of the STM and applies this method to a two-component model amorphous alloy. [3.2] Numerical simulations allow for the visualization of how crystalline and amorphous regions are separated from each other [3.3]

Some previous realistic attempts to detect numerically double-well potentials (DWP's) were made in simulation by Stillinger and Weber [3.1]. Since they chose a rather time-consuming method to detect DWP's, they only reported a few DWP's.

In his important work Heuer (see also Section 2.5) calculated numerically the energy landscape of a model system of 32 Lennard-Johnes (LJ) particles with simulated densities ρ =1 and ρ=1.075 in units of the nearest-neighbor distance *a* and for unit mass. He found 367 minima with different energy for ρ=1 and 75 for ρ = 1.075. It was already seen through the observation of the energy distribution of minima, that the absolute number of minima decreases by more than a factor of 4 when going from ρ=1 to ρ = 1.075.

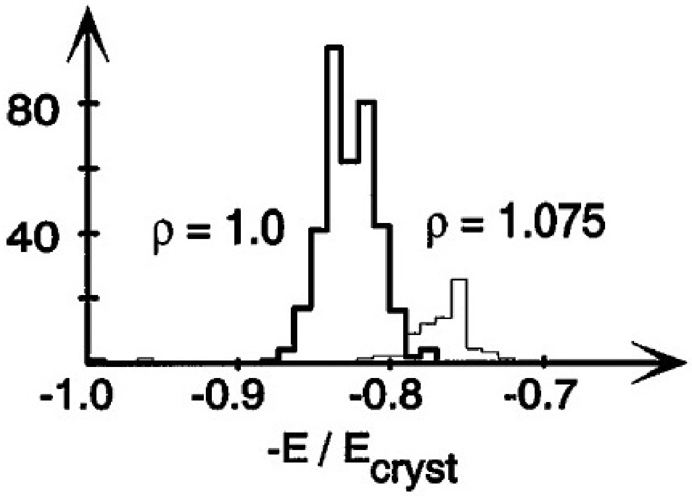

Fig 3.2 – The energy distribution of the number of found minima for ρ=1(thick line) and ρ=1.075 (thin line).

The Euclidean distances of all pairs (k_1, k_2) of minima in configuration space is $[d(k_1,k_2)]^2 = \sum_{i_1}^{N}\left[\vec{r}_{i_1,k_1} - \vec{r}_{i_2(i_1),k_2}\right]^2$, where *N* is number of particles, $\{\vec{r}_{i_1,k_1}\}$ and $\{\vec{r}_{i_2,k_2}\}$ are positions of the *N* particles. The notation $i_2(i_1)$ indicates that *a priori* it is not evident which particle of configuration k_2 corresponds to which particle of k_1, so that several mappings have to be checked. The tunneling systems which dominate the low temperature properties correspond to pairs of minima with an average value of $d \approx 0.35$.

Heuer defines a DWP as a couple of neighbouring pairs of minima k_1 and k_2 such that the energy at its saddle is smaller than the energy of all other saddles which can be reached either from minimum k_1 or k_2 (see Fig 2.4). Corresponding to this configurational landscape there were found 7 DWP's for 223 minima, with a probability of 14/223 per minimum that it belongs to a DWP and the corresponding density of states has been found to be about $2 \times 10^{46} \mathrm{J}^{-1} \mathrm{m}^{-3}$, that is of the right order of magnitude if compared with experimental data on molecular or metallic glasses. One expects that the complexity of the energy landscape dramatically increases with further increasing the system's size. However, Heuer's work shows that already very small model systems contain relevant information about the nature of real glass-forming systems.

But let us look again at the energy landscape, calculated numerically by Heuer and re-proposed in Fig 3.3 [24]. The DWP's highlighted by Heuer in Fig 2.4 can be viewed, from another point of view, as three-, four-, or more welled local potentials with relatively close energy minima, as in shown by the red-lines highlighting in Fig 3.3. Therefore, the 2LS approach is an oversimplified representation of a more realistic glassy energy landscape, which comprises multi-welled local potentials as well.

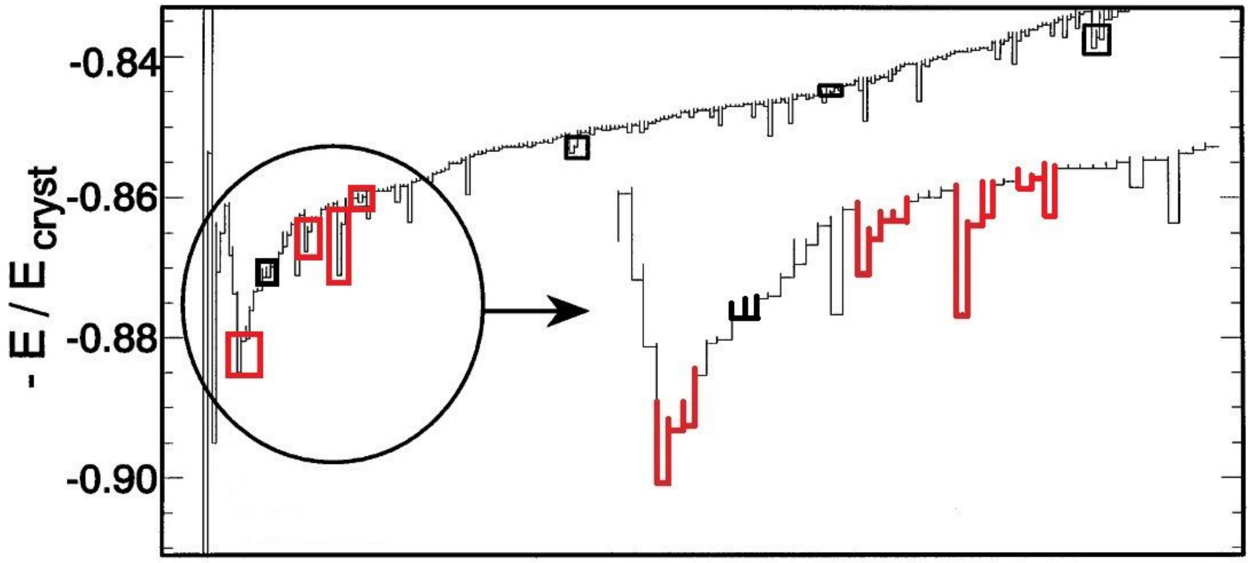

Fig. 3.3 – The energy landscape for ρ =1 with highlighted multi-welled potentials (black the 2LS, red the 3LS, 4LS, …).

Another attempt to find the tunneling states and describe their behavior numerically was presented in the work of K. Trachenko *et al.* [3.4]. They found large sudden rotational rearrangements of the atomic structure with little energy cost, in a dynamical simulation, which may be identified with the tunneling states. In addition to visualising these tunneling states Trachenko *et al.* also answered the question concerning the extent of the part of glass structure which flops from one state to another: whether it involves one atom or tetrahedron, or whether it is spatially more extended. To explain their anomalous thermal data at low temperatures, Zeller and Pohl indeed suggested the existence of large-amplitude reorientational motions of the SiO_4 tetrahedra in a-SiO_2 [2.4, 2.5]

Figure 3.4 shows the time dependence of the coordinates x, y, z of one atom that shows wide jumping motion, together with other similar events that have been identified in other simulation runs for comparison. Fig. 3.5 shows snapshot images of the reorientations of the associated groups of tetrahedra. For this jump movement the participation ratio indicates that the number of tetrahedra involved in this event is around 30 per jump. The largest atomic displacement in these events is typically 0.8 Å. The figure shows superimposed snapshots of the local configuration captured before and after the jump event in order to highlight the large-amplitude re-orientation movements. One considers that the jump event shown in Figs. 3.4 and 3.5 is a candidate event for the jump motion supposed to be involved in the two-level tunneling excitations (2LS). This procedure gave an energy barrier of 0.06 ± 0.02 eV (for about 30 tetrahedra), and the change in energy of the sample on flipping from one state to another was less than 0.01 eV.

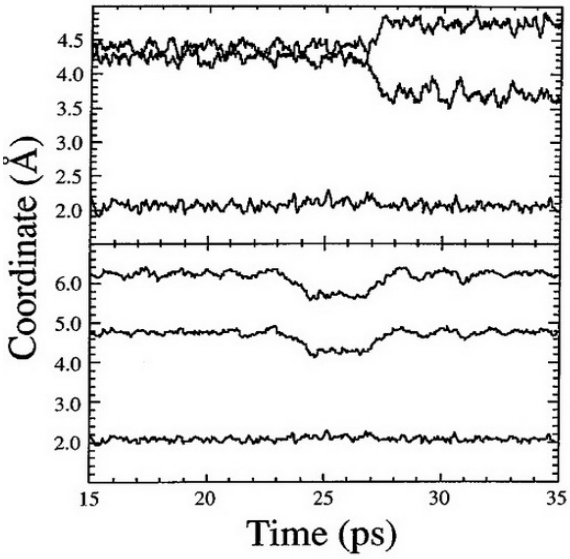

FIG. 3.4 – Time dependence of atomic coordinates x, y, z (in orthogonal Å units) for an atom undergoing a large jump involving a movement of about 0.5 Å (top), and an atom in a different simulation run that jumps from one site to another and subsequently jumps back again (bottom).[3.4]

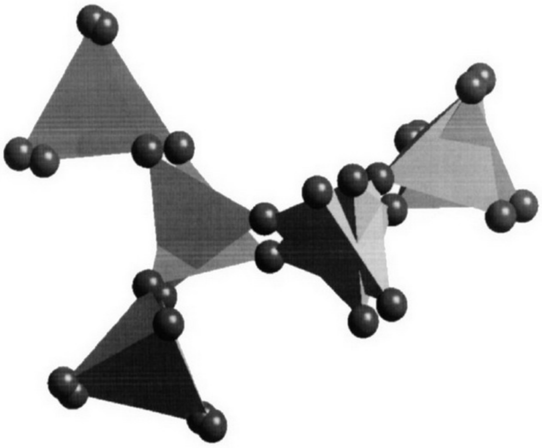

FIG. 3.5 – Snapshot images of the tetrahedra participating in the jump event indicated in Fig. 3.4 captured before and after the jump event. [3.4]

Simulations show that jump events in a sample of 216 tetrahedra happen at intervals of around 20 ps. The simulation also shows that the system has a local free energy minimum in these states, because the system can remain in one state for times much larger that the periods of oscillation of the SiO_4 tetrahedra before jumping to another state, without being able to oscillate back and forwards into the second state. This means that the jump can happen only when all of the tetrahedra associated with the jump are aligned in a particular way. If the system evolves through the cooperative small-amplitude oscillations of the tetrahedra, eventually the potential energy barriers collapse to the small value that has been measured.

In their work, Trachenko *et al.* have for the first time identified the potential tunneling states naturally, by allowing the system to evolve in its own phase space, in contrast to previous simulations for metallic and other glasses [3.1, 3.2, 3.5, 3.6], where in each case their identification has always required some initial stimulation of the system.

The 2LS are an oversimplified view of the local energy landscape's potential minima and were proposed many years ago. A more realistic view can identify 3LS, 4LS and so on in the simulations of the potential energy landscape. The wells in the minima correspond to metastable configurations involving many atoms, the jumps from one well to the next in a local multi-welled TS corresponding to the rearrangement of many atomic groups, like the work of Trachenko *et al.* has indicated [3.4].

Physicists believe that glass is formed when a liquid is cooled quickly and its constituent atoms are unable to arrange themselves in a stable crystalline state. When the temperature becomes lower that the freezing temperature T_f, the atoms link with each other randomly and become trapped in a state, from which they cannot reach their final destination of a crystalline structure. The atoms 'want' to form a crystal structure, but can't. A potential energy landscape can be characterized by a large number of wells, most of them very close to the crystalline phase's energy, but separated from it by high potential barriers (Fig. 3.6 a). These wells can have more (2, 3 or more) smaller adjacent wells, where atoms tunnel through coherently, that can be presented as 3LS, 4LS and so on (Fig. 3.6 b). It was being said before, that groups of atoms create the tetrahedral structure linked to each other by corners. So they can change their position together, when some numbers of atoms are involved within the jump. This creates a coherent tunneling motion of a few atoms.

Multi-component dielectric glasses, like AlBaSiO (*a*-Al_2O_3-BaO-SiO_2, also known as BAS in the literature), BK7, Duran (a complex borosilicate commercial glass), consist of glass-forming (or network-forming (NF)) as well as of crystal-forming (or network-modifying (NM)) atomic species. 50-80% of the components is SiO_2. Other components are B_2O_3, Al_2O_3, Na_2O, BaO, or (in traces) FeO or Fe_2O_3 and so on. What happens when a 'non-glass former' (a good crystal-former) is added to a 'glass-former'? Bridging oxygens link glass-forming tetrahedra, non-bridging oxygens form the ionic bonds with the network-modifiers. NM ions can be large and carry a small charge [2.1]. (Fig. 3.6 c).

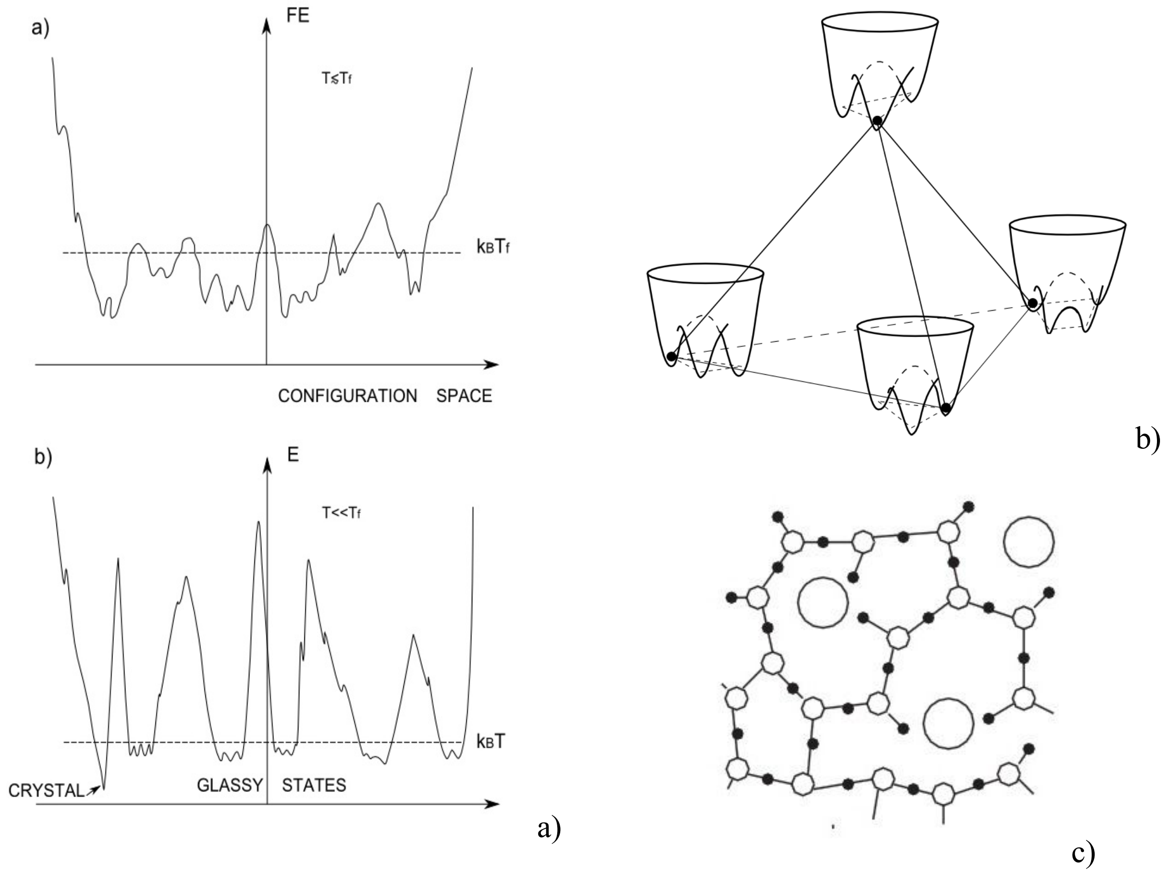

Fig. 3.6 – a) The potential energy landscape of glass as a function of temperature as the system is cooled down below T_f; b) a coherently tunneling group of real particles in the multi-welled potentials; c) mixed glass structure: the large circles represent the network modifiers (Na^+, K^+, Ba^{2+}, Ca^{2+}, Fe^{2+}, Fe^{3+} and so on).

The structure of the multi-component silicate glasses has been investigated by means of molecular-dynamics simulations, neutron scattering and X-ray spectroscopy. Fig. 3.7 shows a snapshot of a simulation [3.7] of the structure of the glass $(Na_2O)\ 3(SiO_2)$ at 2100 K at the density 2.2 g/cm^3 and one can notice that whilst the SiO_4 groups form a well-connected network the Na^+ ions are organized in pocket and channels in the structure and have only a relatively short-ranged connectivity, without forming a network. Simulations on the sodium di- and tri-silicates have shown [3.8] that the NM species (Na^+ ions in this case) cause a general loosening of the tight SiO_4-tetrahedral matrix of pure a-SiO_2 whilst the Na^+ ions show a tendency to form micro-aggregates and to partially destroy the SiO_4-network.

It is natural to imagine that when a multi-component glass is cooled below 1 K, different tunneling entities will develop within the NM regions than the by-now familiar 2LS that are sitting in the network made up by the NF chemical species.

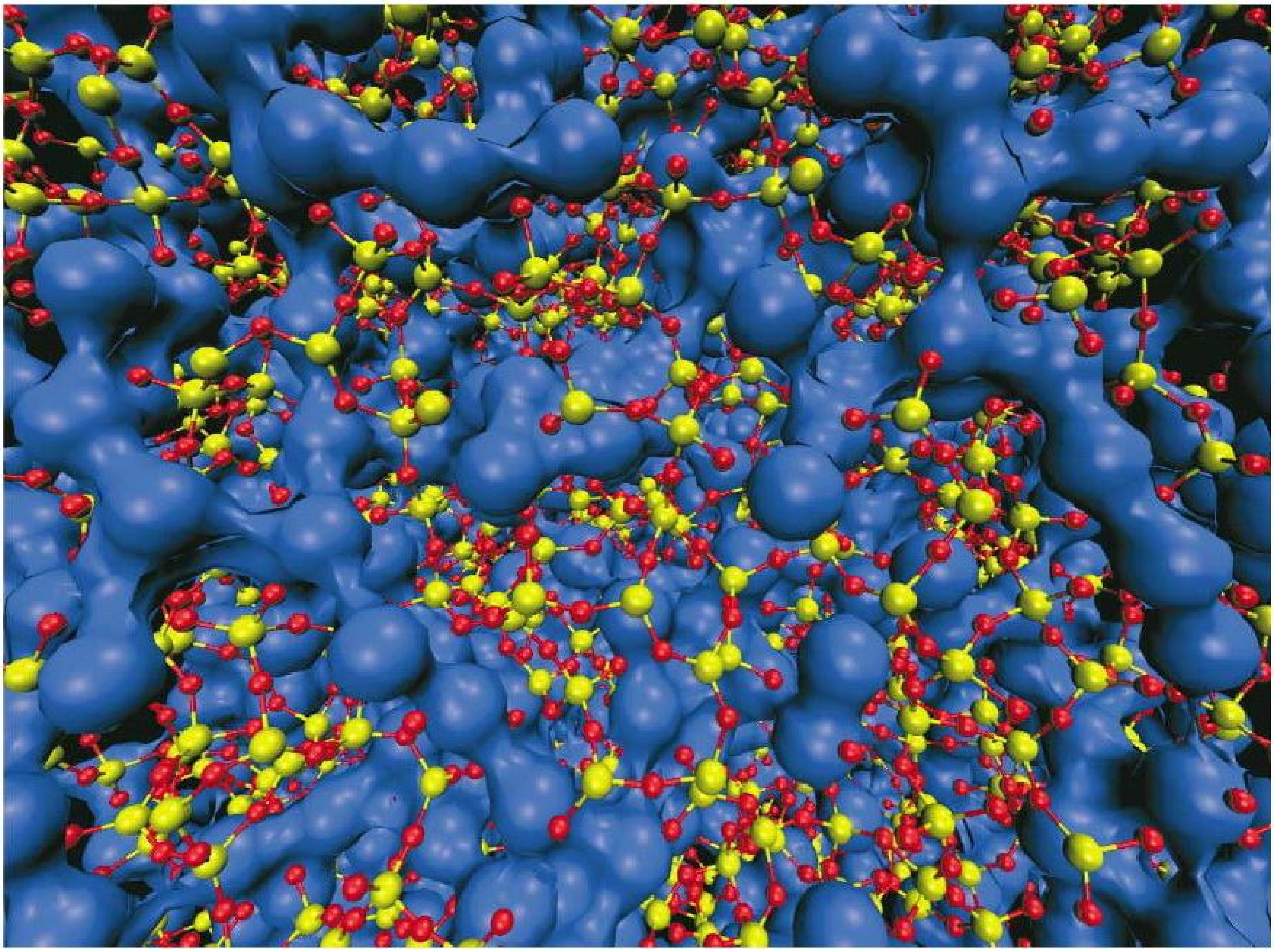

Fig 3.7 – Molecular dynamics snapshot of the structure of sodium trisilicate at 2100 K at the density 2.2 g/cm^3: The blue spheres that are connected to each other represent the Na atoms. The SiO_4-network is drawn by yellow (Si) and red (O) spheres that are connected to each other by covalent bonds shown as sticks between Si and O spheres [3.7].

Chapter 4

Deviations from the standard tunneling model in the mixed glasses

4.1 Comparison between experimental data and STM predictions for the multi-component glasses

In spite of the important contribution of the STM to the description of a wide range of physical properties of glasses at very low temperatures, the 2LS model cannot explain all universalities and features as seen experimentally. Currently there is a number of experiments that show quantitative and qualitative deviations from the STM theory [4.1].

For example, the plateau in the thermal conductivity and the bump ("boson peak") in C_p/T^3, where C_p is the specific heat, around 10 K for all glasses and which cannot be understood in terms of a constant density of tunneling states [4.2].

According to the STM the temperature dependence of the sound velocity $\delta v(T)/v$ and of the dielectric constant $\delta\epsilon'(T)/\epsilon'$ of glass at zero magnetic field has a -2:1 ratio of the slopes in a semi-logarithmic plot. However, the slope ratio found in most experiments on multi-component glasses is rather found to be -1:1, approximately. In addition, it appears that the slopes are slightly different at different frequencies, a fact which is not expected within the STM [4.1]. Moreover, at temperature $T \leq 10$ mK the experimental curves saturate to a constant value, that asks for a high value of the low-energy cut-off: Δ_{0min} ~10 mK [4.3, 4.4]

In the work of Rogge *et al.* [4.5] the dielectric constant of some SiO_x samples is reported at various intensities of the electric field, from 0.33 to 593 kV/m. The minimum in the dielectric constant vs T and the saturation temperature are shifted towards higher temperature values as the electric field is increased; a fact which shows the need to take non-linearities into account. The slope ratio is also different from the theoretically predicted one (-2:1).

Fig. 4.1 (inset) shows the behavior of the T dependent part of ϵ', $\Delta\epsilon'/\epsilon' = [\epsilon'(T) - \epsilon'(T_0)]/\epsilon'(T_0)$, (where $T_0(\omega)$ is the characteristic minimum) for vitreous SiO_2 at a frequency of 1 kHz and zero magnetic field [4.6]. A minimum is observed at a temperature of about 90 mK, in agreement with the results of Frossati et al. [4.7]. The saturation of the dielectric response at low temperature may be explained by a value of Δ_{0min}/k_B which is comparable to the saturation temperature. This means that the density of states ends at this energy and lower temperatures will not activate any more 2LS's; thus resulting in a constant dielectric response. The parameter Δ_{0min} refers to the largest tunneling barrier in the glass.

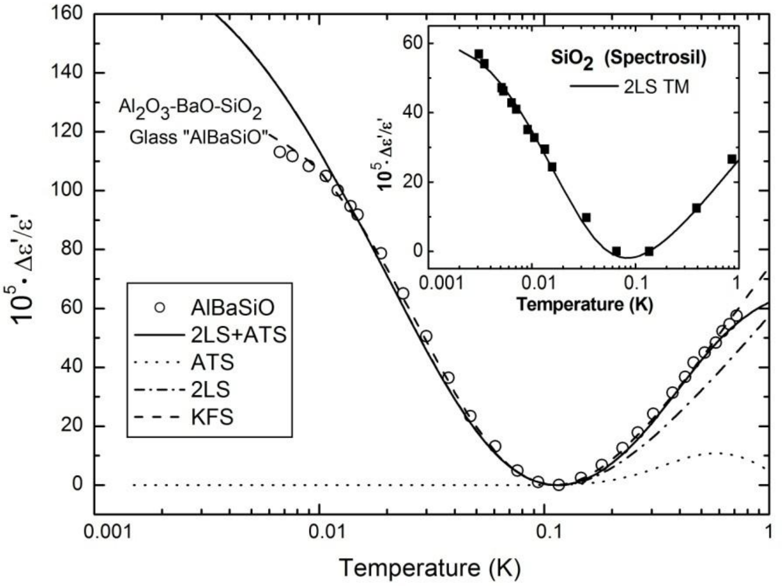

Figure 4.1 – Dielectric signature of pure a-SiO_2 (inset) and AlBaSiO (main) glasses. SiO_2 data [4.6], fitted with Eq.s (2.24-25), display a -2:1 2LS STM behavior. Data for AlBaSiO [4.3] display rather a -1:1 behavior, yet could be fitted with Eq. (2.24, 2.25) (dashed line) [4.4, 4.11] with a large $\Delta_{0min} = 12.2$ mK 2LS tunneling parameter. We have fitted all data with a more realistic $\Delta_{0min} = 3.9$ mK (for the 2LS contribution) and best fit parameters from Table 4.1 (for the ATS) using Eq.s (2.24, 2.25) and (4.20) (driving frequency $\omega = 1$) kHz.

This -2:1 slope ratio behaviour is observed in pure *a*-SiO_2 [4.6] (with the parameters of Table 4.1, *x*=0, from our own best fit to Eq.s (2.24-25) – the sum of resonant and relaxation parts). However in most multi-component glasses one often observes a V-shaped curve with a (roughly) -1:1 slope ratio. Fig. 4.1 (main graph) shows this phenomenon for the AlBaSiO (*a*-Al_2O_3-BaO-SiO_2, also known as BAS) glass, which has been extensively investigated in recent times due to its unexpected magnetic field response [4.11]-[4.13].

Interesting and yet-unexplained behaviour was noted within some older data for the mixed glasses of composition $(SiO_2)_{1-x}(K_2O)_x$ and $(SiO_2)_{1-x}(Na_2O)_x$ for variable x. Fig. 4.4 shows the behaviour of the dielectric constant vs T for the glasses of composition $(SiO_2)_{1-x}(K_2O)_x$ containing a molar concentration x of potassium oxide [4.14] Adding K_2O or Na_2O to vitreous SiO_2 increases the dielectric response (Fig. 4.4), increases the specific heat

(Fig 4.8), decreases the thermal expansion coefficient, and leaves the thermal conductivity essentially unchanged [4.14]. The specific heat $C_p(T)$ for these glasses is larger than for pure silica and the behavior of the plots is very strange for different molar concentrations of potassium or sodium oxide. The heat capacity decreases and then again increases with increasing molar concentration x of K_2O. For the dielectric response it is seen that a S_- /S_+ slope ratio of roughly -1:1 is observed, with the slope definitely changing with x (and faster for $T > T_0$): it qualitatively increases with increasing concentration of K_2O, and this increase has frequency- and temperature-dependence. The minimum in the dielectric constant observed near 0.1 K is typical for glassy solids. One can notice that above the minimum, which corresponds to the relaxation part, ϵ' is increasing faster than the resonant part below minimum. This strongly indicates that not only magnetic and electric fields can influence the properties of glasses, but the concentration of these composite materials can too. The dielectric response shown in Fig. 4.4 arises from the addition of K_2O. The rather large concentrations of K_2O or Na_2O seemingly introduce a new set of TS's. [4.14]

These data, thus far unexplained by the 2LS STM, call for an extension of the accepted TM and we shall now show that a simple explanation can be given in terms of the very same new (*anomalous*) tunneling systems (ATS) that have been advocated by Jug to explain the magnetic response of AlBaSiO and other multi-component glasses [4.12, 4.13] (see also later Chapters of this Thesis). In view of the interest for these materials in low-T thermometry, and on fundamental grounds, such explanation appears overdue to us. Moreover, ‘‘*additional*’’ TS (beside the standard 2LS) of the type here advocated were already called for in [4.14] by MacDonald *et al.* and in earlier papers too. Black and Halperin in [4.15] suggested a new type of TS from an estimation of tunneling-model parameters and from comparison of specific-heat experiments. The specific heat and density of states have contributions from both the 2LS and additional excitations which we call ‘‘*anomalous*’’ tunneling systems (ATS). The spin-phonon coupling of the anomalous systems must be weaker than that of the standard 2LS. On the other hand, the anomalous systems must be sufficiently strongly coupled so as to have relaxation times which are shorter than the duration of the heat-pulse experiments.

In a rather general approach, the TS can be thought of as arising from the shape of the theoretical energy-landscape $E(\{\mathbf{r}_1\})$ of a glass as T is lowered below the glass freezing transition T_f. Many local and global minima develop in $E(\{\mathbf{r}_i\})$ as $T \to 0$, the lowest-energy minima of interest being made up of n_w=2, 3,... local wells separated by shallow barriers. These local multi-welled potentials are our TS and it seems reasonable that the n_w = 2 - welled potentials will be ubiquitous in this picture. These should be thought of as an effective representation of local ‘‘tremblements’’ of the equilibrium positions $\{\mathbf{r}_i^{(0)}\}$ of some of the glass ions' positions (unlike in the disordered crystal case, where the TS ought to be rather well-localized dynamical entities). Hence, just as the $n_w = 2$ - welled case is possible, so ought to be the n_w=3, 4,… – welled situations which would also be local rearrangements involving a few atoms/ions. So long as their energy parameters obey the usual uniform distribution advocated by the STM, however, most of these n_w - welled potentials should present the very same physics as the n_w=2 cases and thus in practice the n_w distribution cannot be resolved experimentally in a pure glass.

All changes if the glass is made up by a mixture of network-forming (NF) ions (like those of the SiO_4 or $(AlO_4)^-$ tetrahedral groups) as *well as* of network-modifying (NM) ions (like K^+ or Na^+, or Ba^{2+}, Fe^{2+},...) which, these last ones, could act as nucleating centers for a partial *devitrification* of the glass, as is known to occur in the multi-component materials [4.16-4.19]. Simulations and experiments in the multi-silicates have shown that NM-species in part destroy the networking capacity of the NF-ions and form their own pockets and channels inside the NF-network [3.7, 3.8]. Hence, $n_w = 3, 4 \ldots$ **multi-welled systems** inside these NM-pockets and -channels should follow some new energy-parameters' distribution form when some degree of **devitrification** occurs, leading to entirely new physics.

Fig.4.2 presents a cartoon of our modeling of the real multi-component glasses. Within the homogeneous networked background, where only 2LS are borne, there appear regions - whether real micro- or nano-crystals or simply “regions of enhanced regularity” (RER) which are crystalline fluctuations of the supercooled liquid – in which a new type of TS are nucleated.

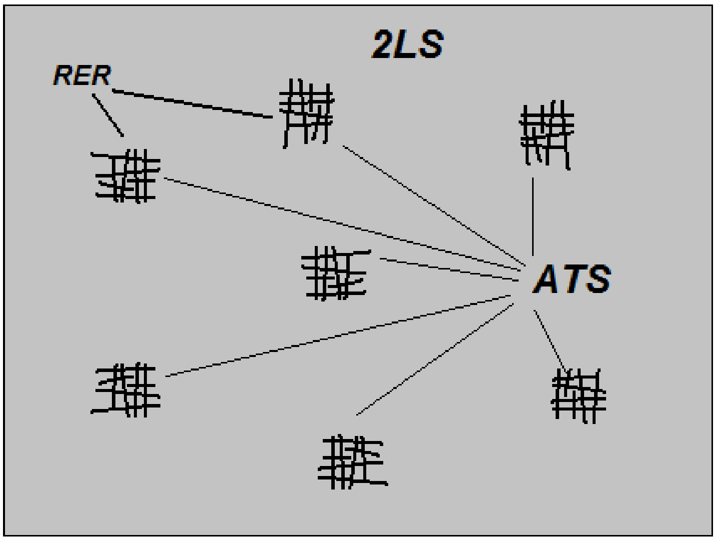

Figure 4.2 – A cartoon of our model of the real glass. Beside the homogeneously networked background (where only 2LS are allowed), the NM-regions allow the formation of crystalline or quasi-crystalline regions where a new type of TS is borne.

4.2 Creating the theory of the ‘‘anomalous’’ tunneling systems

It has been proposed by Jug in 2004 that precisely this situation occurs inside the magnetic-sensitive multi-component glasses [4.12, 4.13], and in this Chapter we show how this theory explains the $B = 0$ dielectric data of Fig.s 4.1, 4.4 – 4.5 and 4.8 as well.

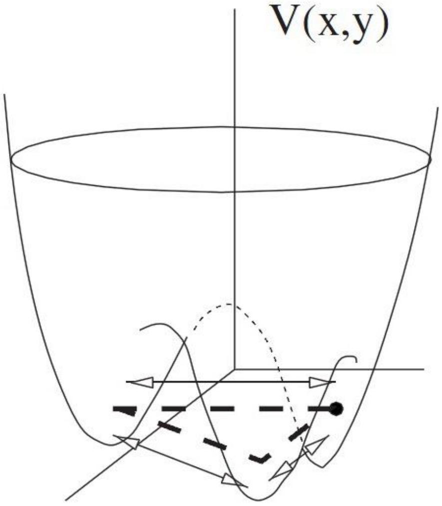

Figure 4.3 – The particle moving in the three-welled potential (not in vacuum, but embedded in a reacting atomic surround).

Instead of the standard 1D double-welled (W-shaped) potential, which continues to describe the ordinary 2LS TS inherent to the a-SiO$_2$ network, we take a fictitious particle of charge q moving in a n_w-welled 3D potential of the type displayed, for $n_w = 3$ and in the 2D space, in Fig. 4.3. The hopping Hamiltonian for a single, non interacting ATS has the form $H_0 = \sum_{i=1}^{3} E_i c_i^\dagger c_i + \sum_{i\neq j} D_0 c_i^\dagger c_j + h.c.$ This local Hamiltonian can also be written in matrix coordinate representation, with $|i\rangle$ $(i = 1,2,3)$ denoting the single-well ground states:

$$H_0 = \begin{pmatrix} E_1 & D_0 & D_0 \\ D_0 & E_2 & D_0 \\ D_0 & D_0 & E_3 \end{pmatrix} \tag{4.1}$$

Here, E_1, E_2, E_3 are random energy asymmetries chosen to satisfy $\sum_{i=1}^{3} E_i = 0$ and taken from an appropriate distribution (see below), together with the tunneling parameter $D_0 > 0$. The latter is chosen positive (contrary to custom in the 2LS TM) due possibly to the softness of the NM-potential, since indeed in general $D_0 \simeq a\hbar\omega_0 e^{-bV_B/\hbar\omega_0}$, a and b being numbers such that for $V_B \gtrsim \hbar\omega_0$ and $b = O(1)$ this positive value of D_0 can arise. This choice is still compatible with the concept of tunneling and yields very large values of $D_0 \sim \hbar\omega_0$.

The best justification, however, for the choice $D_0 > 0$ arises from the following considerations, taken from the work of Sussmann in the 1960s [4.20]. If one considers the problem of a charged particle (e.g. an electron) trapped (at a vacancy or impurity) inside a crystalline solid, then one finds that the atomic orbitals of the embedding crystalline surround make it possible for the particle to develop a degenerate ground state with a non-zero dipole moment. This, Sussmann showed, was possible for the cases where there are three (C_3 symmetry) or four (tetrahedral symmetry) mutually equidistant nearest neighbours. In the C_3 case we have the Hamiltonian (4.1) with all E_i equal and $D_0 > 0$. For the fictitious particle of the TS in a glass the perfect symmetry is lost, but the positiveness of D_0 for the tunneling particle remains, leading to the lowest-lying energy level situation we now envisage.

For this form of the Hamiltonian we have $n_w = 3$ low-lying states, with (see below) $\mathcal{E}_0 < \mathcal{E}_1 \ll \mathcal{E}_2$, where:

$$\mathcal{E}_k = 2D_0\sqrt{1 - \frac{\sum_{i\neq j} E_i E_j}{6D_0^2}}\cos\left(\frac{1}{3}\theta + \theta_k\right) \tag{4.2}$$

$$cos\theta = \frac{E_1 E_2 E_3}{2D_0^3}\left(1 - \frac{\sum_{i\neq j} E_i E_j}{6D_0^2}\right)^{-3/2}$$

with $k = 0, 1, 2$ and $\theta_k = 0, +\frac{2}{3}\pi, -\frac{2}{3}\pi$ distinguishing the three lowest eigenstates.

In the $E_i \to 0$ and $D \equiv \sqrt{E_1^2 + E_2^2 + E_3^2} \ll D_0$ (near-degenerate situation) limits we can approximate the $n_w = 3$ - eigenstate system with an *effective 2LS* having gap $\Delta\mathcal{E} = \mathcal{E}_1 - \mathcal{E}_0$:

$$\Delta\mathcal{E} \simeq \sqrt{E_1^2 + E_2^2 + E_3^2} + O(E_1 E_2 E_3 / D^2) \simeq D \tag{4.3}$$

The condition for the existence of the gap in the absence of a magnetic field, and which vanishes in the symmetric situation by yielding a degenerate ground state, is satisfied. For convenience we have introduced a slight redefinition of D and D_0:

$$\frac{2}{\sqrt{6}}D \to D, \qquad \frac{2}{\sqrt{3}}D_0 \to D_0 \tag{4.4}$$

Another assumption, and the last one, requires that the energy asymmetries $\{E_i\}$ be taken out of a joint probability distribution taking partial devitrification into account:

$$P_{ATS}(E_1, E_2, E_3; D_0) = \frac{P^*}{(E_1^2 + E_2^2 + E_3^2)D_0} \tag{4.5}$$

For the real glasses (composite materials often consisting of a hard gel and containing micro-crystals [4.21], or simply regions of enhanced regularity (RER)) it would seem appropriate to resort to a distribution like equation (4.5), which favours near-degenerate energy asymmetries (due to the micro-crystals or RER). In the case of the commercial ceramic glass ‘Ceran’ (used in the ceramic-glass electric hob industry) it is known that the remarkable thermo-mechanical properties of the material are due to the presence of true micro-crystals embedded in an amorphous glassy matrix [4.22]. Actually, given that the glassy state appears well below the freezing temperature T_f of a liquid with crystal-like fluctuations developing all over for $T<T_f$, it would appear that the RER should be ubiquitous in any glass, whether ideal or real. It is then a matter of their size for the ATS to show up in experiments.

The density of states (DOS) is now obtained by the calculation of:

$$\mathrm{g}_{\mathrm{ATS}}(E) \simeq \int_{D_{0min}}^{\infty} dD_0 \int dE_1 dE_2 dE_3 \;\; P_{ATS}(\{E_i\}; D_0)\, \delta(E_1 + E_2 + E_3)\;\; \delta(E - \Delta\mathcal{E}) \qquad (4.6)$$

The condition $\sum_{i=1}^{3} E_i = 0$ indicates that the integration is efficient in terms of variables defined by this condition. Therefore, it is possible to change variables using polar coordinates and expressing the old coordinates in terms of an angle and a distance:

$$\begin{aligned} E_1 &= D\left(-\frac{1}{\sqrt{2}}\cos\psi + \frac{1}{\sqrt{6}}\sin\psi\right) \\ E_2 &= D\left(-\frac{2}{\sqrt{6}}\sin\psi\right) \\ E_3 &= D\left(\frac{1}{\sqrt{2}}\cos\psi + \frac{1}{\sqrt{6}}\sin\psi\right) \end{aligned} \qquad (4.7)$$

This gives us a simplified form for the DOS:

$$\mathrm{g}_{\mathrm{ATS}}(E) \simeq \int_0^{2\pi} d\psi \int_{D_{min}}^{\infty} dD D \int_{D_{0min}}^{\infty} dD_0 \frac{P^*}{D_0 D^2} \delta(E - \Delta\mathcal{E}) \qquad (4.8)$$

The integration in ψ may be carried out first and is equal to 2π, since the integrand is not dependent of the angle due to complete angular symmetry of the problem in this approximation. If $E > D_{min}$, since $\Delta\mathcal{E} = D$ and does not depend on D_0, it is possible to perform the integration in D first, which allows us to find:

$$\mathrm{g}_{\mathrm{ATS}}(E) \simeq \frac{2\pi P^*}{E} \int_{D_{0min}}^{\infty} \frac{dD_0}{D_0} \qquad (4.9)$$

This integral has a logarithmic divergence due to the upper limit of integration which a priori has been chosen as ∞. The divergence may be eliminated by introducing an upper integration cutoff D_{0max}. In fact, the expression for D_0 ($D_0 \simeq \hbar\omega_0 \exp\left(-\sqrt{\frac{2d^2 m V_B}{\hbar^2}}\right)$), when D_0 assumes all possible values up to +∞, is not physical. Therefore, the introduction of an upper bound of integration seems reasonable. With this upper limit of the values that D_0 can assume, one can perform the integration in D_0 for determining the density of states:

$$\mathrm{g}_{\mathrm{ATS}}(E) \simeq \frac{2\pi P^*}{E} \int_{D_{0min}}^{D_{0max}} \frac{dD_0}{D_0} = \begin{cases} \dfrac{2\pi P^*}{E} \ln\left(\dfrac{D_{0max}}{D_{0min}}\right), & E > D_{min} \\ 0, & E < D_{min} \end{cases} \qquad (4.10)$$

As one can see, the DOS for the ATS's is no longer a constant as for the 2LS STM.

4.3 Dielectric constant

If we think about the new system like an *effective 2LS* with a gap $\Delta\mathcal{E}$, as in Eq. (4.3), we can assume that there are effectively two levels with values $\mathcal{E}_{1,2} = \pm\frac{1}{2}\Delta\mathcal{E} = \pm\frac{1}{2}\sqrt{E_1^2 + E_2^2 + E_3^2}$

Introducing the electric field shifts $\bar{p}_i\bar{F}$ to the diagonal terms E_i of the Hamiltonian H_0, we can estimate the gap $E(\bar{F})$ for the ATS and the partition function $Z(\bar{F})$ of the system in the presence of an electric field $\bar{F}$.

$$\tilde{E}(\bar{F}) = \sqrt{(E_1 - \bar{p}_1\bar{F})^2 + (E_2 - \bar{p}_2\bar{F})^2 + (E_3 - \bar{p}_3\bar{F})^2} \qquad (4.11)$$

$$Z(\bar{F}) \cong e^{-\beta\mathcal{E}_1} + e^{-\beta\mathcal{E}_2} = 2\cosh\left(\frac{\beta\tilde{E}(\bar{F})}{2}\right), \text{ where } \beta = 1/k_BT \qquad (4.12)$$

$\bar{p}_i = q\bar{a}_i$ - is the single-well dipole, q - charge of the fictitious particle, $\bar{a}_i$ – distance from the 3LS centre. The polarization in the electric field is found as:

$$\langle p_\alpha\rangle_{F\neq 0} = -\frac{\partial}{\partial F_\alpha}\left(-\frac{\partial}{\partial\beta}\ln Z(\bar{F})\right) = \frac{\partial}{\partial F_\alpha}\left[\frac{\tilde{E}}{2}\tanh\left(\frac{\beta\tilde{E}}{2}\right)\right]$$

$$= \frac{1}{2\tilde{E}}\left(\tanh\left(\frac{\beta\tilde{E}}{2}\right) + \frac{\beta\tilde{E}}{2}\cosh^{-2}\left(\frac{\beta\tilde{E}}{2}\right)\right)\cdot\left(\sum_{i=1}^{3} -\tilde{E}_i p_{i\alpha}\right) \qquad (4.13)$$

where $p_{i\alpha} = \frac{\partial\tilde{E}_i}{\partial F_\alpha}$.

The linear-response resonant and relaxation contributions to the polarizability for a single ATS are given by:

$$\alpha_{\mu\nu} = \frac{\partial}{\partial F_\nu}\langle p_\mu\rangle\Big|_{F=0}$$

$$\alpha_{\mu\nu}^{RES} = \int_0^\infty \frac{dE}{2E}\,\mathcal{G}_{\mu\nu}\left(\left\{\frac{E_i}{E}\right\};\boldsymbol{p}_i\right)\tanh\left(\frac{E}{2k_BT}\right)\delta(E - \Delta\mathcal{E}) \qquad (4.14a)$$

$$\alpha_{\mu\nu}^{REL} = \frac{1}{4k_BT}\int_0^\infty dE\left(\sum_{i,j}\frac{E_iE_j}{E^2}p_{i\mu}p_{j\nu}\right)\cosh^{-2}\left(\frac{E}{2k_BT}\right)\delta(E - \Delta\mathcal{E}) \qquad (4.14b)$$

where $\mathcal{G}_{\mu\nu}\left(\left\{\frac{E_i}{E}\right\};\boldsymbol{p}_i\right)$ is a geometrical intra-ATS dipole-dipole correlator:

$$\mathcal{G}_{\mu\nu}\left(\left\{\frac{E_i}{E}\right\};\boldsymbol{p}_i\right)=\sum_{i=1}^{3}p_{i\mu}p_{j\nu}-\sum_{i,j}\frac{E_iE_j}{E^2}p_{i\mu}p_{j\nu} \tag{4.15}$$

Equations (4.14 a, b) must now be averaged over the random energies' distribution and over the dipoles' orientations. For a collection of ATS with n_w=3, this averaging can be done resorting to the decoupling:

$$\overline{\mathcal{G}_{\mu\nu}\delta(E-\Delta\mathcal{E})}\simeq\overline{\mathcal{G}_{\mu\nu}}\cdot\overline{\delta(E-\Delta\mathcal{E})} \tag{4.16}$$

where $[\overline{\delta(E-\Delta\mathcal{E})}]_{av}=\mathrm{g}_{ATS}(E)$ is the orientation-averaged DOS. Moreover [4.23]: $\overline{\mathcal{G}_{\mu\nu}}=\frac{1}{3}\overline{p_1^2}\delta_{\mu\nu}\left(3-\frac{1}{E^2}\sum_i\frac{3}{2}E_i^2\right)$, $\sum_{i,j}E_iE_j\overline{p_{i\mu}p_{j\nu}}=\frac{1}{3}\overline{p_1^2}\delta_{\mu\nu}\left(\sum_i\frac{3}{2}E_i^2\right)$, where $\overline{p_1^2}$ - is an averaged dipole for the ATS, $\delta_{\mu\nu}$ is Kronecker's symbol.

If the energy gap is $E\cong D$, the resonant and relaxation contributions after averaging over the orientation have the following forms:

$$\alpha_{\mu\nu}^{RES}=\frac{\overline{p_1^2}}{3}\int_0^{\infty}dE\,\frac{2E^2-D^2}{2E^3}\tanh\left(\frac{E}{2k_BT}\right)\delta(E-D) \tag{4.17a}$$

$$\alpha_{\mu\nu}^{REL}=\frac{\overline{p_1^2}}{3}\frac{1}{4k_BT}\int_0^{\infty}dE\,\frac{D^2}{E^2}\cosh^{-2}\left(\frac{E}{2k_BT}\right)\delta(E-D) \tag{4.17b}$$

The relative change of the dielectric constant is expressed by $\frac{\epsilon(T)-\epsilon_r\epsilon_0}{\epsilon_r\epsilon_0}=x_{ATS}\frac{\alpha(T)}{\epsilon_r\epsilon_0}$, where x_{ATS} is the volume concentration of the ATS's.

At this point we can carry out the averaging over energy's disorder, using the new distribution for the ATS, Eq. (4.5), to get the relative change of the dielectric constant. The relaxation contribution must be multiplied by a frequency- and relaxation time-dependent term:

$$\left.\frac{\Delta\epsilon'}{\epsilon'}\right|_{ATS}=\left.\frac{\Delta\epsilon'}{\epsilon'}\right|_{ARES}+\left.\frac{\Delta\epsilon'}{\epsilon'}\right|_{AREL}$$

$$\left.\frac{\Delta\epsilon'}{\epsilon'}\right|_{ARES}=\frac{\pi\tilde{P}^*\overline{p_1^2}}{3\epsilon_0\epsilon_r}\int\limits_0^{\infty}dE\,\frac{1}{E^2}\tanh\left(\frac{E}{2k_BT}\right) \tag{4.18a}$$

$$\left.\frac{\Delta\epsilon'}{\epsilon'}\right|_{AREL}=\frac{\pi\tilde{P}^*\overline{p_1^2}}{4\epsilon_0\epsilon_r}\frac{1}{k_BT}\int\limits_{Dmin}^{\infty}\frac{dE}{E}\cosh^{-2}\left(\frac{E}{2k_BT}\right)\frac{1}{1+\omega^2\tau_{Amax}^2} \tag{4.18b}$$

Here $\tilde{P}^*=x_{ATS}\,P^*\ln\left(\frac{D_{0max}}{D_{0min}}\right)$. We have neglected, for low-ω, the frequency-dependence in the RES part, τ_{Amax} is the largest phenomenological ATS relaxation time given by [4.23]

$$\tau_{Amax}^{-1} = \frac{D^5}{\Gamma \tanh\left(\frac{D}{2k_BT}\right)} \tag{4.19}$$

τ_{Amax} is the relaxation time at zero field, it has been found by Jug [4.23] from the relaxation theory of ATS in a magnetic field. We put $y = E/D_{min}$, that makes energy dimensionless:

$$\left.\frac{\Delta\epsilon'}{\epsilon'}\right|_{ARES} = \frac{\pi\tilde{P}^*\overline{p_1^2}}{3\epsilon_0\epsilon_r D_{min}} \int_1^\infty \frac{dy}{y^2}\tanh\left(\frac{D_{min}}{2k_BT}y\right) \tag{4.20a}$$

$$\left.\frac{\Delta\epsilon'}{\epsilon'}\right|_{AREL} = \frac{\pi\tilde{P}^*\overline{p_1^2}}{2\epsilon_0\epsilon_r D_{min}}\left(\frac{D_{min}}{2k_BT}y\right) \int_1^\infty \frac{dy}{y}\cosh^{-2}\left(\frac{D_{min}}{2k_BT}y\right)\frac{1}{1+\omega^2\tau_{Amax}^2} \tag{4.20b}$$

Moreover, D_{min} is the lowest energy gap of the multilevel ATS, Γ is an appropriate elastic constant and $\tilde{P}^*$ is the (slightly renormalised) probability per unit volume that an ATS occurs in the NM pockets and channels, with $\overline{p_1^2}$ the average square ATS dipole moment. This description is linked to a distribution function (4.5) for these ATS favouring near-degenerate energy gaps (D bound from above by D_{min}). In turn, this produces an overall density of states $g(E) = g_{2LS} + g_{ATS}(E) \simeq 2\bar{P} + \left(2\pi\tilde{P}^*/E\right)\Theta(E - D_{min})$ that is roughly of the form advocated in [4.14] and by some other preceeding Authors (e.g. [2.21, 4.25]) to explain anomalies not accounted for by the standard 2LS TM.

Manipulation of the expressions in (4.20 a, b) shows that:

1) The RES contribution from the ATS has the leading behavior (for $T < D_{min}/2k_B$, $\epsilon'|_{ARES}$ is a constant)

$$\left.\frac{\Delta\epsilon'}{\epsilon'}\right|_{ARES} \simeq \begin{cases} 0, & if\ T < \frac{D_{min}}{2k_B} \\ \frac{\pi\tilde{P}^*\overline{p_1^2}}{6\epsilon_0\epsilon_r k_BT}\ln\left(\frac{2k_BT}{D_{min}}\right), & if\ T > \frac{D_{min}}{2k_B} \end{cases} \tag{4.21a}$$

2) the REL contribution is, instead, characterised by the leading form

$$\left.\frac{\Delta\epsilon'}{\epsilon'}\right|_{AREL} \simeq \begin{cases} 0, & if\ \omega\tau_{Amax} \gg 1 \\ \frac{\pi\tilde{P}^*\overline{p_1^2}}{\epsilon_0\epsilon_r k_BT}\ln\left(\frac{k_BT}{D_{min}}\right), & if\ \omega\tau_{Amax} \ll 1 \end{cases} \tag{4.21b}$$

Thus, the V-shaped semi-logarithmic curve is somewhat lost. However adding the 2LS (Eqs. (2.24-25)) and ATS (Eqs. (4.20 a, b)) contributions together one does recover a V-shape with a slope $S_- \simeq -2S$ basically unchanged for $T < T_0$ and an augmented slope $S_+ = S + S_{ATS}$ for $T > T_0$ with $S_{ATS} = 7\pi\tilde{P}^*\overline{p_1^2}/6\epsilon_0\epsilon_r k_BT$ that for $T < D_{min}/k_B$ may approach $2S$ and thus (qualitatively) a -1:1 slope ratio.

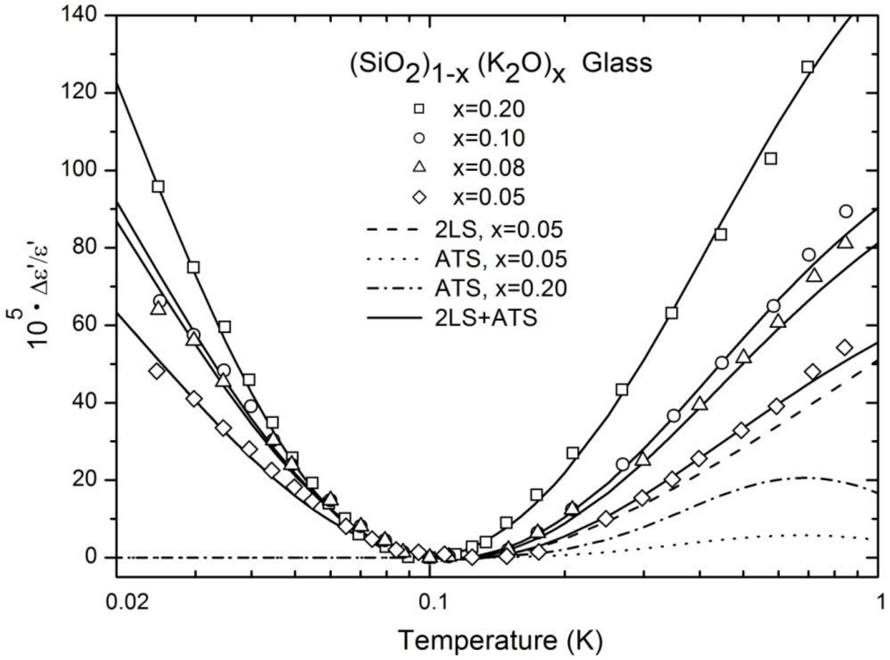

Figure 4.4 – Dielectric response of $(SiO_2)_{1-x}(K_2O)_x$ glasses as function of T and x [4.14]. Fitting parameters from Table 4.1 using Eq. (2.24-25) and (4.20 a, b) from our theory (driving frequency ω = 10 kHz).

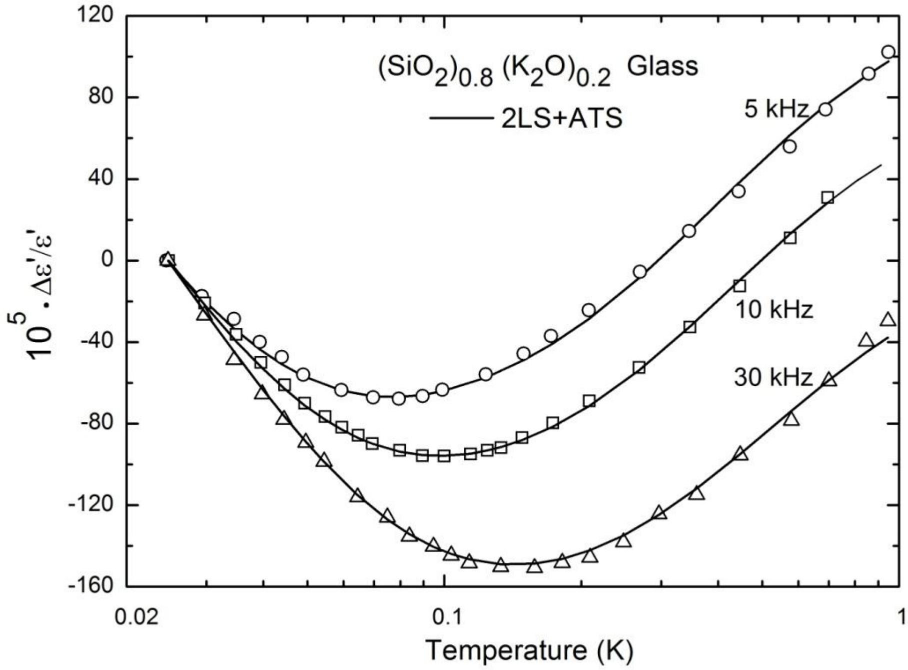

Figure 4.5 – Dielectric response of the mixed-composition glasses $(SiO_2)_{1-x}(K_2O)_x$ as function of T and ω for x=0.2 [4.14]. Fitting parameters are from Table 4.1 using Eq. (2.24-25) and (4.20 a, b) from our theory.

We have fitted expressions (2.24-25) and (4.20 a, b) to the data for AlBaSiO [4.3] in Fig. 4.1 (main) and to the x-dependent data for $(SiO_2)_{1-x}(K_2O)_x$ in Fig.s 4.4 and 4.5, obtaining in all cases very good agreement between theory and experiments [4.24]. Fig. 4.5 shows the fit of our theory to the frequency-dependent data for x=0.2. In all these best fits we have kept the value of Δ_{0min}= 3.9 mK fixed, as obtained from our pure a-SiO$_2$ fit, and the value of D_{min} also independent of x and ω. The idea is that these parameters are rather local ones and should not be influenced by NF/NM dilution. Table 4.1 reports all the (2LS and ATS) parameters used for our best fits and Fig. 4.7 shows the dependence of the extracted prefactors with x.

Table 4.1 – Extracted parameters from the dielectric response of the glasses; K-Si stands for the $(SiO_2)_{1-x}(K_2O)_x$ glasses. In all of the best fits we have employed the values Δ_{0min}= 3.9 mK and Δ_{0max}= 10 K extracted from fitting the pure a-SiO$_2$ data of Fig. 4.1 (inset).

Glass type	x,	A_{2LS}, 10^{-5}	γ, 10^{-8} sK^3	A_{ATS}, 10^{-5}	D_{min}, K	Γ, 10^{-6} sK^5
SiO$_2$	0	47.2	5.30	-	-	-
AlBaSiO	-	116.2	13.40	264.7	0.65	69.73
K-Si	0.05	104.1	1.33	75.5	0.87	3.55
K-Si	0.08	146.5	1.23	130.0	0.87	3.97
K-Si	0.10	158.5	1.15	160.0	0.87	5.08
K-Si	0.20	239.5	0.82	281.9	0.87	6.44

It can be seen that, as expected, the ATS prefactor $A_{ATS} = \pi\tilde{P}^*\overline{p_1^2}/\epsilon_0\epsilon_r D_{min}$ scales linearly with x, an excellent confirmation that the ‘‘additional’’ TS of [4.12, 4.13] are precisely our ATS forming within the micro-crystallites or RER borne by the NM-pockets and channels. It can be seen, instead, from our fits that the 2LS prefactor $A_{2LS} = \bar{P}\overline{p_0^2}/\epsilon_0\epsilon_r$ also increases, though less rapidly, with x (a decrease like 1-x would be expected). We propose (adopting a NF/NM percolation picture) that new, ‘‘induced’’ 2LS form with alkali dilution near the NF/NM surface of the NF percolating clusters as x is increased from 0.

This leads to the expression $A_{bulk}(1-x) + A_{surf}P(x)x^f$ for the 2LS prefactor, with A_{bulk}, A_{surf} and f fitting parameters and $P(x)$ the percolation probability function ($P(x) \simeq 1$ for small x). Our best fit leads to $f = 0.81$, in rather good agreement with the heuristic expression $f = 1 - (D - D_s)\nu$ (D is the fractal dimension of the percolating cluster, $D_s < D$ of its ‘‘elastic’’ surface (not necessarily the hull),ν is the connectedness length's exponent) one would infer from elementary fractal or percolation theory.

The expression for *f* is derived as follows [4.23]. Imagine (Fig. 4.6) the NM-regions percolating through the NF-bulk with a concentration x, so that their typical volume scales like $V_c \approx l^D$, where $l \approx x^\nu$ is their typical linear size. The number of 2LS on the surface of these clusters will scale like $N_{2LS}^{(s)} \approx xP(x)l^{D_s}$ and so their density like $\frac{N_{2LS}^{(s)}}{V_c} \approx xP(x)x^{(D_s-D)\nu} = P(x)x^f$ with the given expression for *f*.

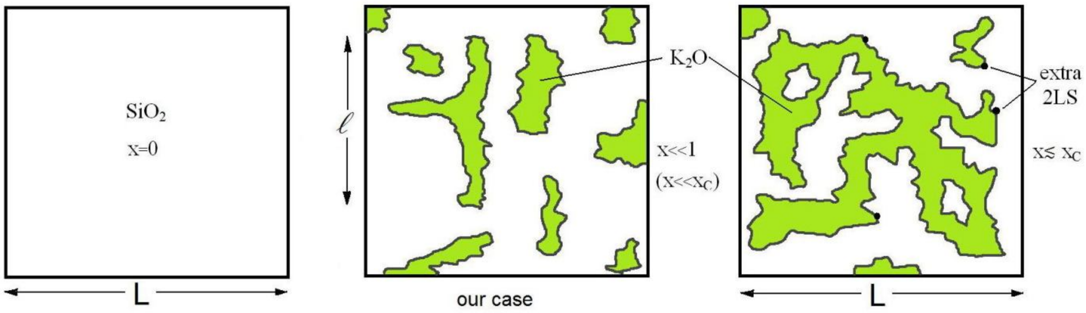

Figure 4.6 – A cartoon of the fractal (presumably percolating) geometry of the NM-pockets and channels, the clusters growing with increasing *x*.

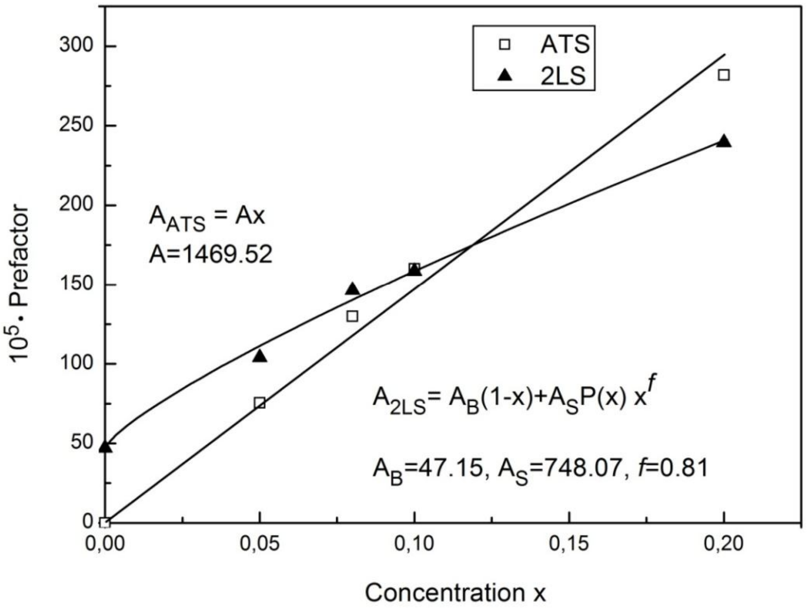

Figure 4.7 – The 2LS and ATS prefactor parameters ($\times\ 10^5$) for all glasses (from Table 4.1) as a function of *x*. Our data fit well with our theoretical expectations (full lines).

4.4 Heat capacity

The heat capacity's low-temperature dependence in zero field for glasses is usually given by the following expression:

$$C_p(T) = B_{ph}T^3 + B_{2LS}T \tag{4.22}$$

The first term accounts for the Debye-type contribution from the acoustic phonons and dominates above 1 K, and the second term is usually attributed to the specific low-energy excitations of all vitreous solids - the 2LS's. B_{ph} and B_{2LS} are constants. This expression describes well the experimental data for pure silica glass at zero field (Fig.4.8 black circles: x=0 with parameters from Table 4.2), but it fails for the multi-component glasses like AlBaSiO, BK7, Duran [4.12] and $(K_2O)_{1-x}(SiO_2)_x$. [4.14]

Typically, the heat capacity's experimental data for the multi-component glasses in zero field denote a kind of 'shoulder' at intermediate-low temperatures. This suggests a density of states, for at least some of the independent tunneling units in the glass, of the form $\mathrm{g}(E,0) \simeq 1/E$, in contrast to the standard TM $\mathrm{g}(E) \simeq const.$, which ensues from the standard distribution. Indeed, this was the very first observation that led to the hypothesis of the ATS formulated by Jug.

To find out the precise expression for the heat capacity of the ATS we use the model of ATS described in Section 4.2 [4.12, 4.13]. The heat capacity is determined as the second derivative of the free energy with respect to temperature:

$$C_p^{ATS}(T) = -T\frac{\partial^2 F_{ATS}(T)}{\partial T^2} \tag{4.23}$$

where $F_{ATS}(T)$ is the free energy of the ATS, where we neglect the third, highest, energy level (effective 2LS approximation):

$$F_{ATS}(T) = -k_BT\ln\left(e^{-\frac{\mathcal{E}_1}{k_BT}} + e^{-\frac{\mathcal{E}_2}{k_BT}}\right) = -k_BT\ln\left(2\cosh\left(\frac{E}{2k_BT}\right)\right) \tag{4.24}$$

The heat capacity is obtained by averaging over the parameter distribution:

$$C_p^{ATS}(T) = k_B\int_0^\infty dE\, \mathrm{g}_{ATS}(E)\left(\frac{E}{2k_BT}\right)^2\cosh^{-2}\left(\frac{E}{2k_BT}\right) \tag{4.25}$$

where the density of states $\mathrm{g}_{ATS}(E)$ has the following form (see Section 4.2):

$$\mathrm{g}_{ATS}(E) = \int dD\int dD_0 P(D,D_0)\delta(E-D) \simeq \begin{cases} \frac{2P^*}{E}, & E > D_{min}, \\ 0, & E < D_{min}. \end{cases} \tag{4.26}$$

and D_{min} is a lower cutoff.

The final expression for the heat capacity results in:

$$C_p^{ATS}(T) = B_{ATS}\left[\ln\left(2\cosh\left(\frac{D_{min}}{2k_BT}\right)\right) - \frac{D_{min}}{2k_BT}\tanh\left(\frac{D_{min}}{2k_BT}\right)\right] \tag{4.27}$$

where the prefactor for the ATS is $B_{ATS} = 2\pi P^* k_B n_{ATS}\rho(x)\ln\left(\frac{D_{0max}}{D_{0min}}\right)$, n_{ATS} - is the ATS mass concentration, $\rho(x)$ - mass density.

For $k_BT \gtrsim D_{min}$ this is indeed roughly a constant and gives the observed 'shoulder' in $C_p(T)$ when the contribution $B_{ph}T^3$ (from virtual phonons) as well as the standard $B_{2LS}T$ are added.

Both prefactors, for 2LS and ATS, are dependent on the molar concentration x, just as we found before: $B_{2LS} \sim B_{bulk}(1-x) + B_{surf}P(x)x^f$, $B_{ATS} \sim x$. Also γ_{ph} should be re-evaluated. With increasing concentration x for the $(SiO_2)_{1-x}(K_2O)_x$ glass, the number of phonons from the NM component (K_2O) increases linearly with the concentration x, and for the NF component (SiO_2) it should decrease linearly like (1-x). As we assumed in the previous Section, there are percolation effects between NM and NF systems, which make room for some percolation clusters and surfaces, where phonons also might create a contribution someway proportional to $C_{ph}P(x)x^f$.

For some glasses, moreover, a non-negligible concentration of Fe^{3+} impurities is reported, which is a consequence of the industrial production process: 102 ppm for AlBaSiO and 126 ppm for Duran [4.26], 100 ppm for Pyrex 7740 and 12 ppm for Pyrex 9700 [2.3, 2.10]. All glasses may have some $[FeO_4]^0$ impurities substitution centers (in the glass, similar to a liquid, in concentrations much much lower than the nominal Fe concentrations). The Fe^{3+} cation and the O^{2-} anion, on which the hole is localized (forming the O^- that is O^{2-} + hole subsystem), form a bound small polaron. In this configuration the Fe^{3+} cation is subject to a crystal field with an approximate C_3 symmetry axis along the Fe^{3+} - O^- direction. This axis plays a quantization role for the Fe^{3+} electronic spin. The hole is assumed to be tunneling between two neighboring oxygen ions, switching the quantization axis between two directions and therefore entangling the spin states. We should, therefore, also take into account the contribution from Fe-impurities to the heat capacity from [4.27] and for $B = 0$. The spin Hamiltonian of the $[FeO_4]^0$ center at $B = 0$ is $H_{S-S} = V_z s_z S_z$, where: V_z - is the principal value of the dipole interaction matrix, s_z and S_z - are the spin operators of the O^- and Fe^{3+} ions, respectively. In the absence of a magnetic field there are only two ground state energy levels $E_{1,2} = \pm\frac{5}{4}|V_z|$. The distribution function $G(V_z)$ must approach zero while its argument approaches either zero or infinity and have a maximum at a definite argument value V_0. The simplest one-parameter function demonstrating such properties is a Poisson distribution:

$$G(V_z) = \frac{4V_z^2}{V_0^3}\exp\left(-\frac{2V_z}{V_0}\right), \qquad V_z \in (-\infty; 0], \qquad V_0 < 0 \tag{4.28}$$

The contribution from the $[FeO_4]^0$ ensemble to the specific heat is as follows:

$$C_{Fe^{3+}}(T) = -T\frac{\partial^2 F_{Fe^{3+}}}{\partial T^2} \tag{4.29}$$

where $F_{Fe^{3+}}(T)$ is the free energy of the $[FeO_4]^0$ ensemble, that one finds as:

$$F_{Fe^{3+}} = -k_B T \ln\left(e^{-E_1/k_BT} + e^{-E_2/k_BT}\ \right)$$
$$= -k_B T \ln\left(2\cosh\left(\frac{E}{2k_BT}\right)\right) \tag{4.30}$$

(here $E = \frac{5}{4}|V_z|$).

Using the distribution function for $G(V_z)$, as well as the expressions for $C_{Fe^{3+}}(T)$) and $F_{Fe^{3+}}(T)$, one can obtain the expression for the specific heat from the few $[FeO_4]^0$ centres, which should be added to the total heat capacity C_p:

$$C_p^{Fe^{3+}}(T) = \rho(x)x_jk_B\int_0^\infty dV_z\left(\frac{E}{2k_BT}\right)^2\cosh^{-2}\left(\frac{E}{2k_BT}\right)G(V_z)$$
$$= \rho(x)x_jk_B\int_0^\infty dV_z\frac{25V_z^4}{16T^2}\frac{1}{V_0^3}e^{\left(-\frac{2V_z}{V_0}\right)}\cosh^{-2}\left(\frac{5V_z}{8k_BT}\right) \tag{4.31}$$

where x_j – volume concentration of the substituting Fe^{3+}.

So the total heat capacity will be the sum of all these contributions ((4.22), (4.27) and (4.31)):

$$C_p(T) = B_{ph}T^3 + B_{2LS}T + C_p^{ATS}(T) + C_p^{Fe^{3+}}(T) \tag{4.32}$$

Making use of expression (4.32) we can fit the experimental data for the specific heat for the $(SiO_2)_{1-x}(K_2O)_x$ glasses from [4.14]. In order to fit the a-SiO_2 data we use only formula (4.22), that fits well the pure silica's data within the 2LS model.

The specific heat data [4.14] for $(SiO_2)_{1-x}(K_2O)_x$ glasses were obtained using a signal-averaging technique. The samples of $(SiO_2)_{1-x}(K_2O)_x$ glass have different concentrations of their K_2O component, from 0 to 20%, they were roughly cubic in shape and about 1 cm in size. The OH content was about 20 ppm. The specific heat $C_p(T)$ of these samples is presented in Fig. 4.8.

As one can see, the specific heat for $(SiO_2)_{1-x}(K_2O)_x$ glass at small temperatures is larger than that for pure silica, already with the smallest 5% concentration of K_2O. The heat capacity decreases and then again increases with increasing of molar concentration x of K_2O. The additional heat capacity arises from the addition of K_2O and from the Fe^{3+} impurities, contained in small concentrations, but contributing to the low and middle range of temperatures.

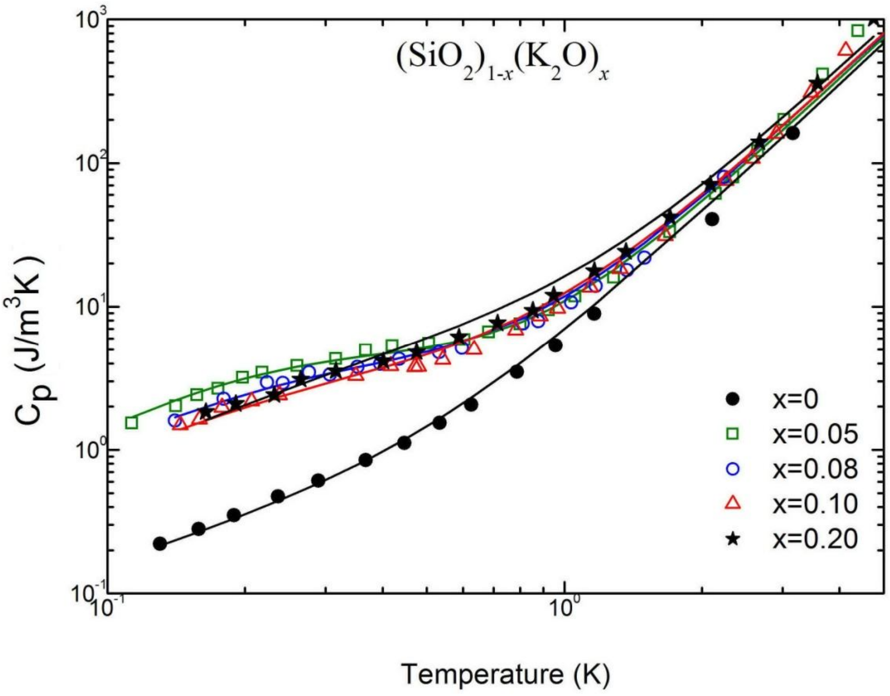

Figure 4.8 – The temperature dependence of the specific heat for a-SiO_2 (black circles) and for the $(SiO_2)_{1-x}(K_2O)_x$ glasses [4.14]. The lines are the theoretical curves, generated by Eq. (4.32)

Table 4.2 – Extracted parameters from the heat capacity of the SiO_2 and $(SiO_2)_{1-x}(K_2O)_x$ glasses, with $D_{min} = 0.87$ K and $V_0 =- 0.42$ K as fixed.

glass type	x	$B_{ph} \times 10^8$, $Jg^{-1}K^{-4}$	$B_{2LS} \times 10^8$, $Jg^{-1}K^{-2}$	$B_{ATS} \times 10^8$, $Jg^{-1}K^{-1}$	$x_j\, k_B \times 10^8$, $Jg^{-1}K^{-1}$	x_j, ppm
SiO_2	0	245.55	70.65	–	–	–
K-Si	0.05	260.92	155.23	22.77	402.0	29.86
K-Si	0.08	266.36	196.11	36.44	241.0	18.15
K-Si	0.10	269.46	221.62	45.55	138.0	10.54
K-Si	0.20	281.42	337.19	91.11	38.0	3.00

Both prefactors, for 2LS and ATS, are dependent of the molar concentration x, and just as we have found before: $B_{2LS} \sim B_{bulk}(1-x) + B_{surf}P(x)x^f$, $B_{ATS} \sim x$. These dependences are show in Fig.4.9. Also γ_{ph} should change by increasing the concentration of impurities.

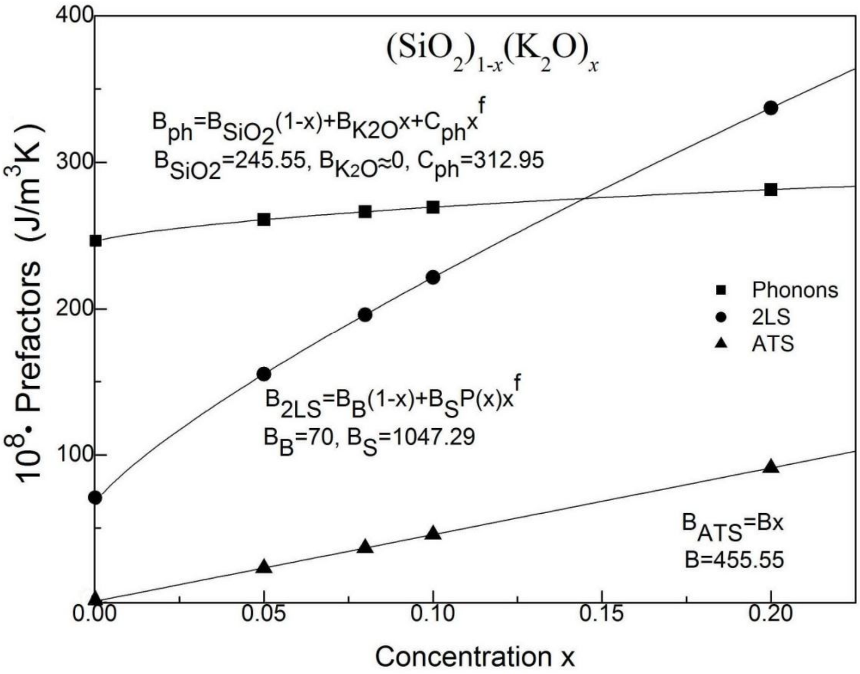

Figure 4.9 – The 2LS and ATS prefactor parameters ($\times 10^8$) for all glasses (from Table 4.2) as a function of x. Our data fit well with our theoretical expectations with $f = 0.81$ (full lines).

With increasing concentration x for the $(SiO_2)_{1-x}(K_2O)_x$ glasses the number of phonons from the NM component (K_2O) increases linearly with the concentration, and for the NF component (SiO_2) should be decreasing linearly like (1-x). As we supposed before, there are percolation mixing effects between the NM and the NF systems, which creates some percolation clusters at their surfaces, where phonons (or fractons) also might be created in a way proportional to $C_{ph}P(x)x^f$.

In summary, we have shown that there is direct evidence in zero magnetic field already for the multi-welled ATS and with the new distribution function advocated to explain the magnetic-field effect in the multi-component glasses (see following Chapters). The relevance of the multi-welled TS in the multi-component glasses is a new and unexpected finding in this field of research. Our work predicts that the magnetic response of the alkali-silicate glasses should be important and scale like the molar alkali concentration x. At the same time the -1 : 1 slope ratio problem of the standard TM has been given a simple explanation in terms of our two-component tunneling model.

Using the results of this analysis (and for AlBaSiO the results of the analysis in a magnetic field) we can estimate the value of the dipole moment associated with the ATS, $p_{eff} = \sqrt{\overline{p_1^2}}$. For AlBaSiO, using the value of $\tilde{P}^*$ extracted from C_p [4.12] and that of A_{ATS}

given in Table 4.1 we extract $p_{eff} = 0.41$ D. For $(SiO_2)_{1-x}(K_2O)_x$, we notice from the definitions in this Chapter that the ratio of dielectric and heat capacity prefactors:

$$\frac{A_{ATS}}{B_{ATS}} = \frac{\rho(x)}{2\epsilon_0 \epsilon_r k_B D_{min}} \overline{p_1^2} \tag{4.33}$$

is almost independent of the K_2O concentration x. From our extracted values in Tables 4.1 and 4.2 and the measured values of $\rho(x)$ [4.14] we extract $p_{eff} = 0.045$ D independently of x. Considering the elementary dipole's value $ea_0 = 2.54$ D, these small values of p_{eff} for the ATS confirm that their new physics must come from the coherent tunneling of small ionic clusters (the very same origin for the large values of D_{min} and (later Chapters of this work) for $D_{0min,max}$). Indeed, the cluster of N coherently tunneling particles has a dipole moment $p_{eff} = \left|\sum_{i=1}^{N} \vec{p}_i\right|$ that can become much smaller than ea_0 as N grows large. The fact, that we extract values of p_{eff} much smaller than ea_0, confirms this picture already in the $B = 0$ case.

Chapter 5

Extension of the tunneling model: effect of a magnetic field

The linear dependence in $\pm \ln T$ of the dielectric constant $\epsilon'(T)$ makes glassy material useful in low-temperature thermometry and, normally, structural window-type glasses are expected to be isotropic insulators that do not present any remarkable magnetic-field response phenomena (other than a weak response to the inherent trace paramagnetic impurities). However, recent studies of some multi-component glasses developed for low-temperature thermometry [5.1-5.4] have shown a remarkable and unexplainable anomalous magnetic-field-dependent behaviour. The multi-component AlBaSiO glass (or BAS), presents at very low temperatures (1<T<100 mK) an unexpected enhanced dielectric response to very weak magnetic fields already (B~10 mT, the magnetic field of the earth being ~40 mT) [4.3, 4.11].

AlBaSiO is contaminated with ca.100 ppm Fe-impurities; other, also much cleaner, multi-component borosilicate glasses (BK7, less than 6 ppm [5.5], and Duran, ~120 ppm [4.26] of paramagnetic Fe) show similar magnetic anomalies, thus excluding the paramagnetic impurities as their source. The fact that the magnetic response does not scale with the paramagnetic impurity concentration indicates that the phenomenon is not paramagnetic-impurity related. Moreover, similar effects have been confirmed concomitantly [5.6] in studies of the iron-free structural glass a-$SiO_{2+x}C_yH_z$ in the range 50<T<400 mK and with B up to 3T.

The unexpected magnetic response of the cold glasses calls for an extension of the STM.

A fist attempt to explain this unusual phenomenon, consisting of a 3D version of the 2LS STM, is the work of Ketteman, Fulde and Strehlow (KFS) [4.4]. The fictitious tunneling particle is imagined as moving in a hat-like type potential, shown in Fig 5.1a, with two potential barriers in azimuth direction along the rim of the hat and two non-equivalent minima, between which the tunneling can occur along different paths. Under these conditions the particle couples orbitally to the magnetic field through the Aharonov-Bohm (AB) effect

[5.7]. A field B applied along the z axis forces the charged particle to circular motion in the perpendicular plane having radius r. In the general case when the field B has an arbitrary angle α with the plane of motion, the magnetic flux through the circular orbit of a TLS is given by $= B\pi r^2 \cos \alpha$.

In analogy to the STM , the ground state and the first excited state of this 3D 2LS can be well approximated by a superposition of the ground states of each potential well's harmonic oscillator, if $V_B \gg \hbar\omega_0 > \Delta$, where ω_0 is the oscillator frequency and $V_B \approx (1/8)m\omega_0^2\pi^2r^2$ is the potential barrier; r is a radius. The energy eigenvalues are found to be $E_\pm = \left[\hbar\omega_0 + \Delta \pm \mathrm{E_g}(\phi)\right]/2$ and periodic in the magnetic flux ϕ/ϕ_0 as seen in Fig.5.1b. $\phi_0 = h/q$ is the appropriate flux quantum. The energy gap is expressed by $E_\mathrm{g}(\phi) = \sqrt{\Delta^2 + t(\phi)^2}$, where $t(\phi) = \Delta_0 \cos(\pi\phi/\phi_0)$ is now the magnetic flux-dependent tunneling splitting, that replaces the tunneling parameter Δ_0 of the STM. The parameter distribution function is assumed to be the same as for the STM (2.8).

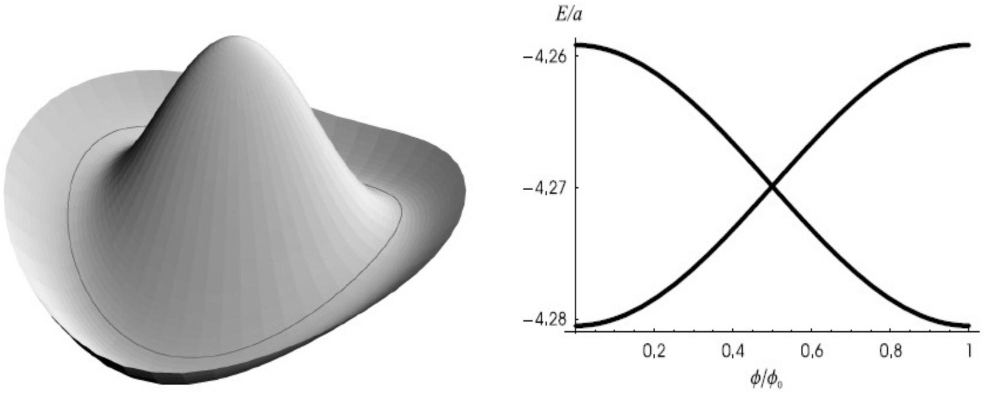

a) b)

Figure 5.1 – a) Hat-like potential. The double-well potential for a charged particle confined to a circular path is indicated by the thin line; b) the two lowest energy eigenvalues as a function of the flux ratio ϕ/ϕ_0 [4.4]

In the low-temperature resonant regime at zero field, the temperature dependence of the dielectric constant $\epsilon'_{RES}(T, \phi = 0)$ can be described well by assuming $\bar{P}p^2/\epsilon_0 = 1.03 \times 10^{-2}$ and a high value of $\Delta_{0min}/k_B = 12.2$ mK [4.4]. The deviation from the logarithmic temperature dependence of ϵ'_{RES} is observed in a magnetic field where $\epsilon'_{RES}(T, \phi = \phi_0/2)$ becomes maximal. To explain within this model the maximum in the real part of the dielectric constant at $B \approx 0.1$ T, as experimentally observed for AlBaSiO samples, the required charge of the tunneling particle must be assumed to be of order $|q| \sim 10^5|e|$, e being the electron's charge. Such a large value of q was interpreted as resulting from the *coherent* tunneling state of a mesoscopic ($\sim 10^5$ 3D 2LS) cluster of TS [5.8]. The KFS model does not find support from either the theoretical or the experimental side. For one, if this explanation were the correct one, then also pure a-SiO$_2$ would display magnetic effects as for the other multi-component silicates, a fact that so far has not been experimentally reported. There must be, therefore, something new and specific of the multi-component glasses, that is at the origin of the magnetic effects.

The amplitude of the two-pulse dipole echo in the multi-component nonmagnetic glasses mentioned above exhibited also a strong non-monotonic dependence on the magnetic field even in weak fields (about 10 mT), whilst pure a-SiO$_2$ gave no response at all. These experiments are a confirmation of how the TS in glasses behave as pseudo spin-S entities, $S \geq \frac{1}{2}$. Wurger, Fleischmann and Enss (WFE) [5.9] suggested that this unusual magnetic field effect is caused by the presence of tunneling atoms with non-spherical nuclei carrying an *electric quadrupole moment* in the glass, because a-SiO$_2$ does not contain nuclei with spin $I > \frac{1}{2}$, while all other glasses do and in good concentrations. The interaction of the quadrupole moment with the gradient of the static microscopic electric field in the two wells of double-well potentials creates an energy-level fine-structure splitting in a 2LS transforming the 2LS into a multi-level system (albeit with a very small fine energy structure in $B = 0$).

The WFE nuclear-quadrupole model is capable to explain some of the experimental data of the two-pulse dipole echoes, in particular the results for the echo in vitreous glycerol ($C_3H_8O_3$) [5.10]. It was shown, that the replacement of hydrogen, having zero quadrupole moment, by deuterium, with a nonzero quadrupole moment, increases the echo amplitude by more than a factor 10. However, the weak magnetic-field non-monotonic dependence of the echo in non-deuterated glycerol could not be explained in such a way.

To explain this phenomenon Bazrafshan et al. [5.11] suppose that the magnetic field dependence of the echo amplitude in a-$C_3H_8O_3$ is caused by the extra weak dipole-dipole interaction of the nuclear magnetic moments of the hydrogen atoms. This interaction also creates a hyperfine structure of the two levels in the 2LS, which depends on the applied magnetic field through the very weak nuclear Zeeman coupling. In the papers [5.12, 5.13] the two-pulse echo amplitude was numerically calculated in part-deuterated a-glycerol $C_3D_5H_3O_3$, assuming that the tunneling motion in the two-level systems is the rotation of the glycerol molecule as a whole. Later in [5.14] an analytical theory of the magnetic field dependence of the two-pulse echo amplitude in glasses with dipole-dipole interaction of nuclear spins was developed. Without any assumption about the microscopic tunneling mechanism of the hydrogen atoms in glycerol and other fitting parameters than a prefactor, it also shows a reasonable agreement with the experimental data.

The nuclear-quadrupole model seems to be adequate to explain the polarization echo experiments (though it predicts many oscillations when only one, typically, or at most two are observed as a function of B), but it fails to describe the B-field dependence of the dielectric constant even qualitatively. A static (ω=0) calculation of the dielectric constant's dependence in the presence of quadrupole moment couplings has shown the wrong form of the B- and T-dependence of $\delta\epsilon' /\epsilon'$ compared to experiments and, most importantly, that the order of magnitude of the magnetic $\delta\epsilon' /\epsilon'$ is a factor 10^6 weaker than observed [5.15].

In the work of Burin et al. [5.16] it is shown how a strong magnetic field dependence of the electric susceptibility in ultra-cold glasses can be qualitatively understood by taking into account the interactions of TS in the presence of nuclear quadrupolar moments as suggested by Würger *et al* [5.9]. In multi-component glasses the quadrupolar effects may be caused by Na, K, Al and B nuclei. The basic point is that the number of different energy levels of a TS increases, even by effect of small applied magnetic field. The magnetic field influences the energy spectrum since the particle obtains a Zeeman energy depending on the nuclear spin projection. The magnetic field produces a Zeeman splitting. It is larger than the quadrupolar splitting, when the magnetic field increases. The interactions of a nuclear quadrupole electrical moment with the crystal field and of a nuclear magnetic moment with magnetic field transform the two-level tunneling systems into multi-level tunneling systems. Increasing the number of different energy levels of a TS modifies the concentration of resonant tunneling pairs and leads to observable effects. This model tries to explain the behavior of the real and imaginary parts of the dielectric constant of the system to an applied magnetic field. But in this model the increasing in the dielectric constant with magnetic field was found in orders of magnitude too small compared with the available experiments. By the authors' opinion it asks for larger values of the quadrupole splitting.

The nuclear-quadrupole approach, in whichever form, also fails to explain the decrease of the dielectric constant, with $\delta\epsilon' /\epsilon'$ becoming negative after the first positive enhancement, as the magnetic field further increases. A major setback is however represented by recent echo experiments with the doped crystals KCl:Li (also good realizations of the 2LS STM) in which selected samples with the isotopes ^{6}Li or ^{7}Li have been studied experimentally [5.17]. These isotopes have very different nuclear quadrupole moments (Q(^{6}Li)= – 0.001 barn and Q(^{7}Li)= – 0.040 barn), ^{6}Li having by far the smallest and thus KCl crystals with such selected interstitials ought to reveal the weakest magnetic-field response in the echo. The opposite was observed, instead, KCl:^{6}Li giving the most spectacular oscillations in the magnetic field and also waiting time oscillations. This puts serious doubts on the validity of the WES nuclear-quadrupole explanation.

For the explanation of the magnetic field effect for the dielectric constant of the a-$SiO_{2+x}C_yH_z$ glass (a system completely devoid of nuclear-quadrupole carrying species) J. Le Cochec, F. Ladieu and P. Pari in the work [5.6] proposed a model with two local potential sites separated by a disordered barrier as demonstrated in Fig. 5.2. Tunneling between the two sites of the (quasi-symmetric) 2LS separated by the distance a is strongly affected by the potential barrier's disorder. This is modeled by a three-dimensional network of impurities (the unit length of which is the elastic mean free path λ_{el}) and Δ_0 results from the coherent sum of all quantum paths along the impurity network. This model can be compared with our 3-welled tunneling model (previous and following Chapters), where the "rugged barrier" can be represented the 3-rd, 4-th and so on potential wells with somewhat higher energy value. The shift of the dielectric constant $\delta\epsilon'(B)$ depends on the magnetic field B through $\Delta_{0max}(B)$, that means the tunnel transparency is affected by the magnetic field. Numerically it was found that $\langle \delta \ln[\Delta_0(H)] \rangle \propto a/\lambda_{el}$. For the extrapolation of the experimental data one can account $a \simeq 5\lambda_{el} \simeq 1$ nm, giving an elementary dipole $p_0 \simeq 10\ D$. But in the mechanism described above the behavior of $\delta\epsilon'(B)$ is a monotonous one on B, i.e., it cannot account for the peaked structure around $B = 0.03$ T reported in [4.3].

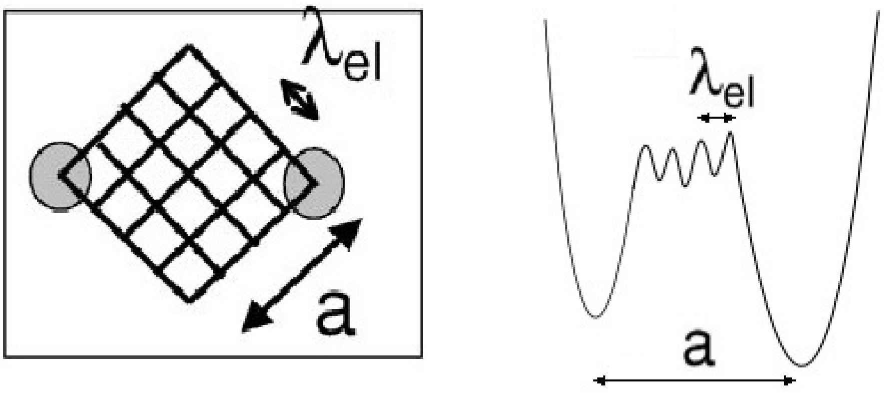

a) b)

Figure 5.2 – Schematic view of the disorder lying within the tunnel barrier of size ~a between the two sites (gray circles) of a 2LS: the potential fluctuations are modeled by a set of ''impurities'' of interspacing λ_{el} whose energies are drawn at random either well above or well below that of the 2LS [5.6]; b) 2D representation.

A successful interpretation of the $\delta\epsilon'(B)/\epsilon'$ non-monotonous changes for AlBaSiO in a field has been reported in the work of A. Borisenko and A. Bakai [5.18] Their approach relies on the idea that paramagnetic tunneling states (PTS) might exist in the glasses due to localized electrons or holes associated with chemical species having valence different from those of the host atoms. Thus, a distribution is envisaged for 2LS-like tunneling charged particles (typically holes) carrying also a spin-$\frac{1}{2}$ and thus a magnetic moment. The tunneling of this very localized, charged and spin-$\frac{1}{2}$ particle in shallow double-well 1D potentials is treated approximately and results in a reasonable agreement with experiment. The tunneling motion leads to the non-conservation of the magnetic moment due to the disorientation of the hole-associated electronic quadrupole moment by the random "crystal" field. This feature gives rise to the non-monotonic magnetic field dependence of the dielectric susceptibility of the PTS ensemble. Also, good agreement with the magnetic-field dependence of the heat capacity C_p and of the polarization echo experiments for some Fe-contaminated multi-silicates has been reported. However, no explanation for the magnetic effects in vitreous glycerol or in the cleaner multi-silicates (BK7) is offered by this PTS approach.

No one of the present theories, invented to describe the magnetic field effect in glasses at very low temperatures, could explain all of the experimentally observed effects in glasses at the same time. In the following Chapters will be shown how our own multi-welled tunneling model can explain all of the low temperature magnetic effects in glasses discovered so far.

Chapter 6

The multi-welled tunneling model for real glasses in a magnetic field

In this Chapter we extend the novel anomalous tunneling model introduced in Chapter 4 in order to explain the low temperature properties observed in glasses in the presence of weak to moderate magnetic fields. The magnetic field makes the dependence of the specific heat of the multi-compound glasses non-monotonous with the increasing field. Data from [4.26] for the AlBaSiO and Duran glasses indicate strong deviation from Eq. (4.22) at zero magnetic field already. The data show that starting from the curve at zero field, the specific heat initially increases with increasing of the magnetic field, and then decrease at high fields (Fig. 6.1 a, b). A behaviour of this type has been observed for the multi-compound glasses AlBaSiO and Duran, and has been rather well reproduced and explained by the theoretical approach using the ATS model proposed by Jug in 2004 [4.12].

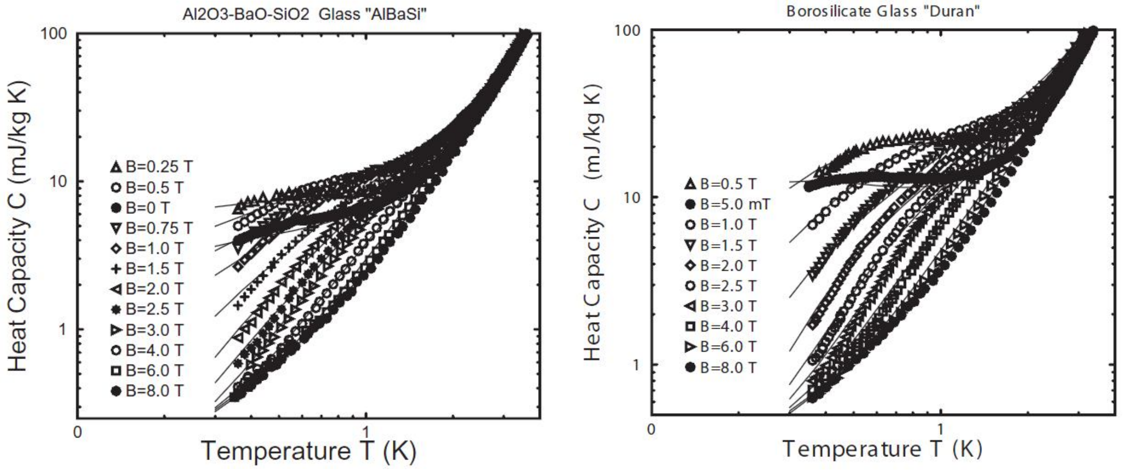

a) b)

Figure 6.1 – Double-logarithmic plot of heat capacity C_p/T as a function of temperature T and magnetic field B for the heat capacity of the AlBaSiO (a) and Duran (b) glasses [4.12].

One way to explain the effects of the magnetic field (orbital, Aharonov-Bohm type coupling) is to consider the motion of a fictitious charge q particle in a n_w-welled potential, with $n_w \geq 3$. The barrier V_B through which the fictitious particle tunnels might be taken to be relatively shallow, so that $V_B \approx \hbar\omega_0$, ω_0 being the frequency of a single-well ground state, whilst tunneling still takes place. This makes the present explanation rather different from the hat-like model of [4.4], where the ordinary $V_B \gg \hbar\omega_0$ situation (deep wells) is envisaged. As was explained in the previous Chapter 4, more realistically a situation of this type arises when the (fictitious) particle is embedded in an atomic medium, as the work of Sussmann [4.20] has shown.

Each fictitious charged particle's move encloses the magnetic flux, resulting in local tunneling currents. They couple to the magnetic field through the particle's orbital motion: a three-welled potential landscape's minimum is described in Fig. 4.3.

The zero field Hamiltonian (4.1) changes in the presence of the field by developing a phase factor of the Aharonov-Bohm type, and becomes thus

$$H_0 = \sum_{i=1}^{3} E_i c_i^\dagger c_i + \sum_{i \neq j} D_0 e^{i\phi_{ij}} c_i^\dagger c_j + h.c. \tag{6.1}$$

The phase ϕ_{ij} (also known as Peierls phase) is given by:

$$\phi_{ij} = \pm \frac{2\pi}{3} \frac{\Phi(B)}{\Phi_0} = -\phi_{ij} = \frac{q}{c} \int_i^j d\mathbf{l} \cdot \mathbf{A} = \pm \frac{\phi}{3} \tag{6.2}$$

where Φ_0 is the appropriate flux quantum equal to $hc/|q|$, q being the fictitious tunneling particle's charge, and $\Phi(B) = \mathbf{B} \cdot \mathbf{S}_\Delta = BS_\Delta \cos\beta$ is the magnetic flux through each tunneling unit, β being the tiling angle of the planar loop of surface S_Δ with respect to $\mathbf{B}$. $\mathbf{A}$ is a magnetic vector potential, $d\mathbf{l}$ is an infinitesimal vector element of the loop contour around its surface S_Δ .

This local Hamiltonian can also be written in matrix representation, with $|i\rangle$ $(i = 1, 2, 3)$ denoting the single-well ground state:

$$H_0 = \begin{pmatrix} E_1 & D_0 e^{i\phi/3} & D_0 e^{-i\phi/3} \\ D_0 e^{-i\phi/3} & E_2 & D_0 e^{i\phi/3} \\ D_0 e^{i\phi/3} & D_0 e^{-i\phi/3} & E_3 \end{pmatrix} \tag{6.3}$$

The ground states of the three potential minima are random numbers, that can be chosen to satisfy the condition $\sum_{i=1}^{3} E_i = 0$ and $D \equiv \sqrt{E_1^2 + E_2^2 + E_3^2} \ll D_0$ (where E_i can be both positive and negative) together with $D_0 > 0$, as it was assumed in Chapter 4 in relation with Sussmann's work [4.20].

The distribution function considered here is the very same used in the absence of magnetic field, Eq. (4.5), which corresponds to a distribution of ATS's, which, as it was described before, can be realized within the multi-compound glasses due to NM species micro-phasing in the glass network.

Considering the spectrum of the Hamiltonian in Eq. (6.3) as a function of the AB phase ϕ, it is possible to find an exact solution for the multi-welled tunneling Hamiltonian using Cardano's trigonometric solution method for the cubic equation:

$$\mathcal{E}_k = 2D_0\sqrt{1-\frac{\sum_{i\neq j} E_i E_j}{6D_0^2}}\cos\left(\frac{1}{3}\theta+\theta_k\right) \tag{6.4}$$

$$\cos\theta = \left(\cos\phi + \frac{E_1E_2E_3}{2D_0^3}\right)\left(1-\frac{\sum_{i\neq j} E_i E_j}{6D_0^2}\right)^{-3/2},$$

with $k = 0,1,2$ and $\theta_k = 0, +\frac{2\pi}{3}, -\frac{2\pi}{3}$ distinguishing the three lowest eigenstates.

We have $n_w = 3$ low-lying states periodic in ϕ (Fig. 6.2). The magnetic-field period, however, for $S_\Delta \approx 10$ Å^2, $q = -2|e|$ and $\mathbf{B}$ orthogonal to the ATS surface, is huge in the absence of macro/mesoscopic ATS-correlations: $B \approx 10^4$ T. We can thus concentrate on the relevant regime $\phi \to 0$, $E_i \to 0$, where $\mathcal{E}_0 < \mathcal{E}_1 \ll \mathcal{E}_2$.

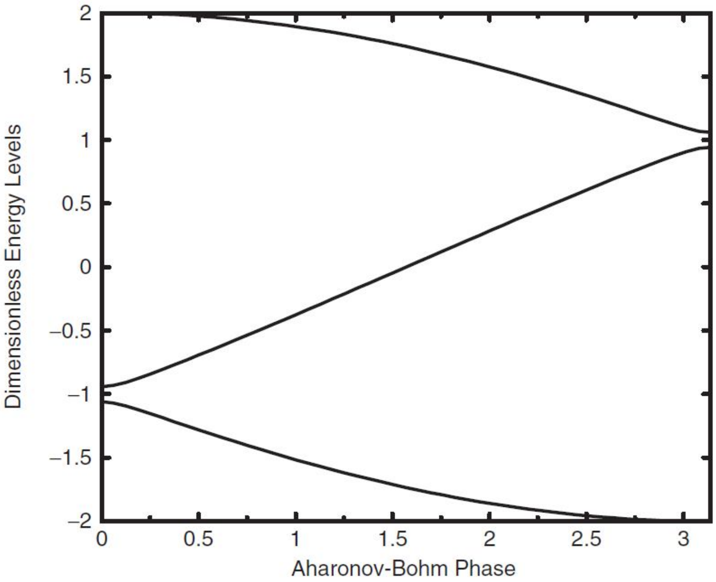

Figure 6.2 – The three energy levels as a function of Aharonov-Bohm phase ϕ for a choice of E_1, E_2, E_3 with $D/D_0 = 0.01, D_0 = 1$.

The chosen distribution function favours to the situation where $D \to 0$, but this choice also implies an enhanced probability of finding tunneling units that show a strong Aharonov-Bohm effect; in fact, this situation makes the interference trajectories almost equal in terms of path integrals, as is implied by the Aharonov-Bohm effect. If the distribution is not singular in D, but is as was assumed for the 2LS model, the amount of tunneling systems which experiences a strong Aharonov-Bohm effect is small and thus the effect of the magnetic field on the mono-component glasses would be much less stronger than in the case of the multi-component glasses.

Considering the weak magnetic field regime at low temperature, we obtain an effective 2LS by reducing again three levels to a two-level model with energy gap equal to $\Delta\mathcal{E} = |\mathcal{E}_1 - \mathcal{E}_0|$ that now depends on the phase $\phi(B)$, which is supposes to be small. This approximation is justified if we consider that the third level is much higher in energy than the other two. Using known trigonometric formulas, the shape of the energy gap between levels $\mathcal{E}_1$ and $\mathcal{E}_0$ can be obtained, remembering that the angle θ is small and also using the redefinition (4.4):

$$\Delta\mathcal{E} \simeq \sqrt{D_0^2\phi^2 + (E_1^2 + E_2^2 + E_3^2) + \mathrm{O}(E_1E_2E_3/D^2)} \simeq \sqrt{D_0^2\phi^2 + D^2} \tag{6.5}$$

So in this effective-2LS picture the energy gap opens with increasing magnetic field B, from a minimal energy gap D at zero magnetic field, instead of closing like in other orbital-model approaches [4.4, 5.6, 5.9]. The linear approximation ensuing from (6.5) is reasonable when ϕ is consider to be small, but not vanishingly so.

Introducing a magnetic field, the density of states changes and is given by the integrals (4.6) and (4.8), but now with the new energy gap (6.5):

$$\mathrm{g}_{ATS}(E,\phi) \simeq 2\pi \int_{Dmin}^{\infty} dD\, D \int_{-\infty}^{+\infty} dD_0 \frac{P^*}{D_0 D^2}\,\delta\left(E - \sqrt{D_0^2\phi^2 + D^2}\right) \tag{6.6}$$

Solving for this integral, we can replace the original variable that contains the dependence on the magnetic field. Using the representation:

$$\delta\big(f(D)\big) = \sum\nolimits_a \frac{\delta(D - D_a)}{|f'(D_a)|}$$

where D_a are the zeros of $f(D)$, one finds that:

$$\mathrm{g}_{ATS}(E,\phi) \simeq 2\pi\, P^* \int_{D_{0min}}^{D_{0max}} \frac{dD_0}{D_0}\frac{E}{\sqrt{E^2 - D_0^2\phi^2}} \int_{Dmin}^{\infty} \frac{dD}{D}\,\delta(D - D_1) \tag{6.7}$$

where $D_1 = \sqrt{E^2 - D_0^2\phi^2}$, so can obtain an integral with one variable less:

$$\mathrm{g}_{ATS}(E,\phi) \simeq 2\pi\, P^* \int_{-\infty}^{+\infty} \frac{dD_0}{D_0}\frac{E}{E^2 - D_0^2\phi^2}\,\theta(D_0 - D_{0min}) \times$$

$$\times\,\theta(D_{0min} - D_0)\,\theta\left(\frac{1}{\phi}\sqrt{E^2 - D_{min}^2} - D_0\right) \tag{6.8}$$

The integral (6.8) can be solved easily for three intervals $E < E_{c1}$, $E_{c1} \le E \le E_{c2}$ and $E > E_{c2}$. There are two critical values of the energy gap, $E_{c1} = \sqrt{D_{min}^2 + D_{0min}^2\phi^2}$ and

$E_{c2} = \sqrt{D_{0max}^2 \phi^2 + D_{min}^2}$, where the density of state changes. Solving the integral (6.8) we obtain the density of states with energy as well as the magnetic field dependence:

$$g_{ATS}(E,\phi) = \begin{cases} 0, & \text{for } E < E_{c1} \\ \dfrac{2\pi P^*}{E} \ln\left(\dfrac{\sqrt{(E^2 - D_{0min}^2\phi^2)(E^2 - D_{min}^2)}}{D_{0min}\, D_{min}\, \phi}\right), & \text{for } E_{c1} \le E \le E_{c2} \\ \dfrac{2\pi P^*}{E} \ln\left(\dfrac{D_{0max}}{D_{0min}} \sqrt{\dfrac{E^2 - D_{0min}^2\phi^2}{E^2 - D_{0max}^2\phi^2}}\right), & \text{for } E > E_{c2} \end{cases} \qquad (6.9)$$

The ATS density of states, as can be seen from Fig. 6.3, consists of two parts, defined by two different ranges of possible values of energy. There is a range of possible energies, where the density of states increases with increasing magnetic field; this is partly responsible for the initial increasing of specific heat at low field.

In Fig. 6.3 (a, b) a plot of $g_{ATS}(E,\phi)$ is shown as a function of energy E and AB-phase ϕ of a single ATS. It can be seen that for $\phi = 0$ the form $g_{ATS}(E,\phi) = const/E$ is recovered, cut off by a D_{min} below which no ATS states can exist (disorder gap). As soon as the magnetic field is switched on, the sharp peak near D_{min} in $g_{ATS}(E,\phi)$ is eroded away, with most states in the DOS being transferred to higher energy from the immediate neighborhood of the disorder gap at very small values of ϕ. When ϕ increases the ATS DOS is rapidly washed away and vanishes. With increasing the energy E the ATS DOS decreases, the peak moves to higher values of ϕ and the DOS stretches (Fig. 6.3 a). This behaviour of the $g_{ATS}(E,\phi)$ explains in a qualitative way the experimental observations. All the magnetic properties of glasses have a similar shape of the curve vs B. It is due to the form of the DOS $g_{ATS}(E,\phi)$, which they reproduce through the appropriate energy convolution.

The linear-response resonant and relaxation contributions to the polarizability for a single ATS in the magnetic field are also given by (4.14 a, b), but now with the new, magnetic field dependent, energy gap.

Equation (4.15) with the magnetic dependent energy gap for a general number of wells n_w has the form:

$$\overline{\mathcal{G}_{\mu\nu}\left(\left\{\frac{E_i}{E}\right\}, \boldsymbol{p}_i\right)} = \frac{n_w}{n_w - 1} \frac{1}{3} \overline{p_1^2} \frac{(n_w - 2)E^2 + D_0^2\phi^2}{E^2} \delta_{\mu\nu} \qquad (6.10)$$

which shows that there is a magnetic-field enhanced term only when $n_w > 2$. For 3LS with $n_w = 3$ equation (6.10) becames:

$$\overline{\mathcal{G}_{\mu\nu}\left(\left\{\frac{E_i}{E}\right\}, \boldsymbol{p}_i\right)} = \frac{1}{3} \overline{p_1^2} \frac{E^2 + D_0^2\phi^2}{E^2} \delta_{\mu\nu} = \frac{1}{3} \overline{p_1^2} \frac{2E^2 - D^2}{E^2} \delta_{\mu\nu} \qquad (6.11)$$

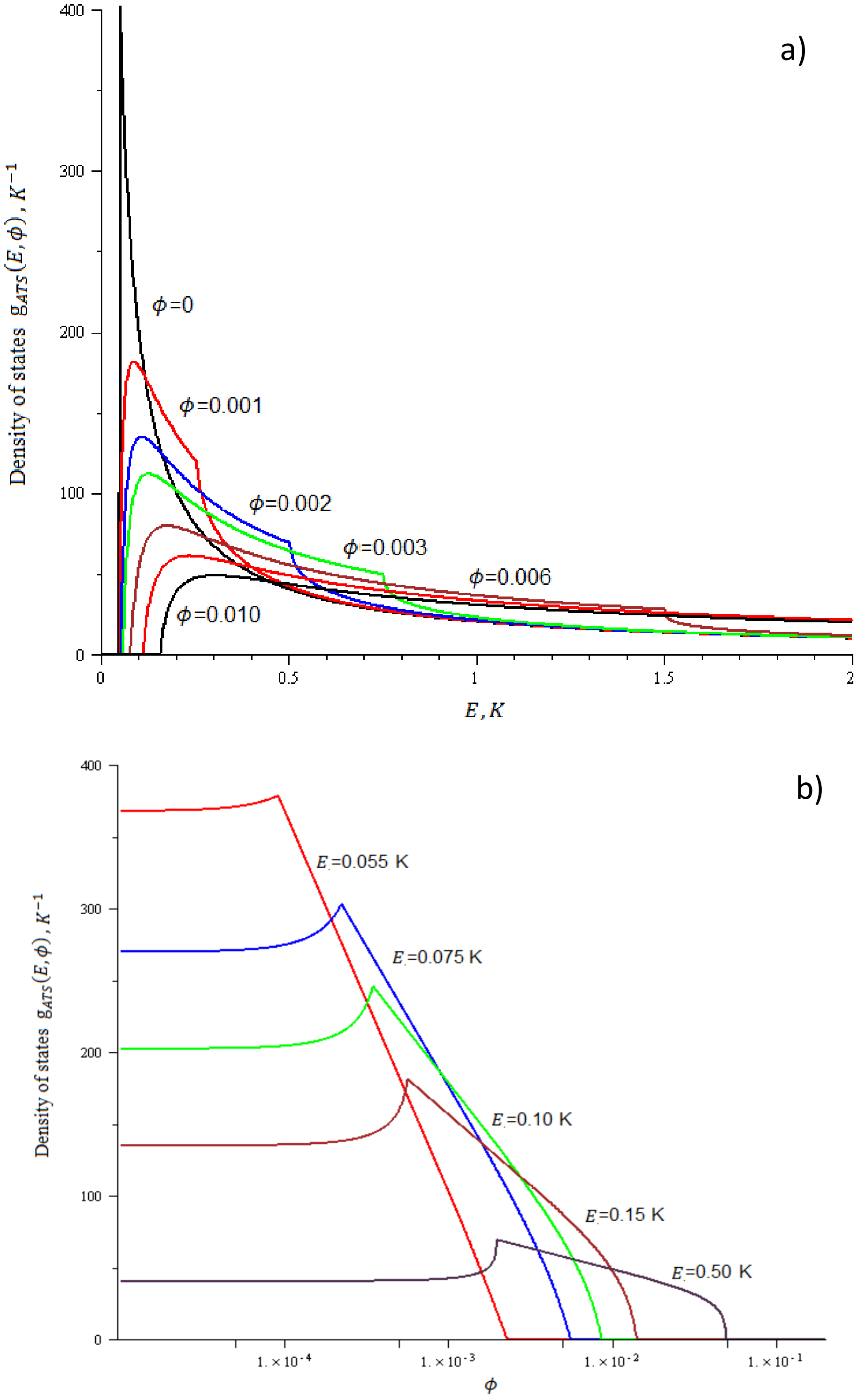

Figure 6.3 – a) Variation with the magnetic Aharonov-Bohm phase ϕ of the density of states $g_{ATS}(E,\phi)$ associated with anomalous tunneling systems (ATS) as a function of the energy E (for $D_{0max} = 30D_{0min}$ and for $\frac{D_{min}}{D_{0min}} = 0.03$); b) the density of states $g_{ATS}(E,\phi)$ as a function of the magnetic Aharonov-Bohm phase ϕ for different energies. The peak at some field value is reproduced in several experiments.

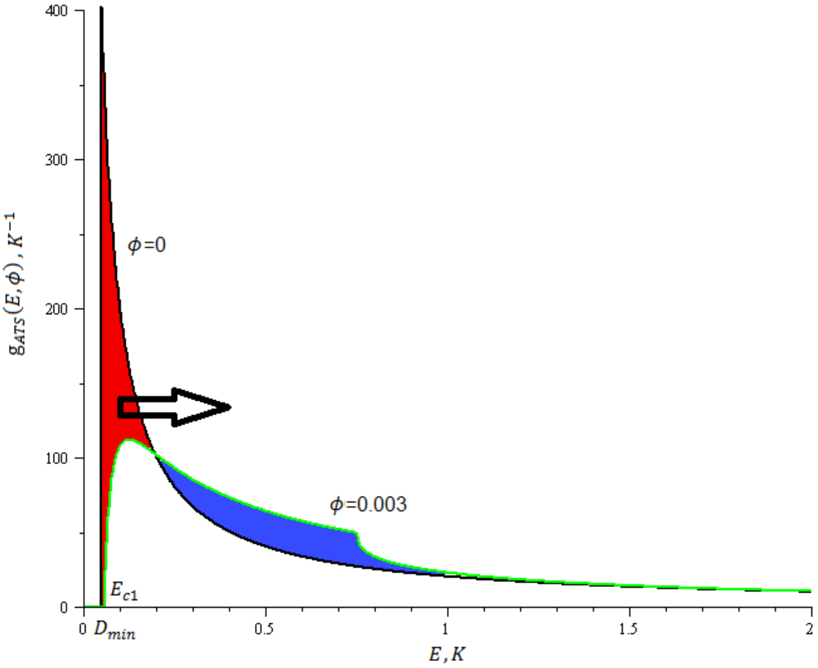

Figure 6.4 – The physical origin of the magnetic field effect. The area under each curve is the total number of states available (per ATS); so, switching on a magnetic field - however small - means that a large number of $B = 0$ states within a narrow energy range near D_{min} (red shaded area) get tossed to a widespread band of higher energies (blue shaded area) for $B > 0$.

Inserting (6.11) and (6.5) into (4.14 a, b), one finds the resonant and relaxation contributions to the polarizability for a single ATS in the magnetic field:

$$\alpha_{RES} = \frac{\overline{p_1^2}}{4}\int_0^{\infty} dE\,\frac{2E^2 - D^2}{E^3}\tanh\left(\frac{E}{2k_BT}\right)\delta\left(E - \sqrt{D^2 + D_0^2\phi^2}\right) \qquad (6.12a)$$

$$\alpha_{REL} = \frac{\overline{p_1^2}}{8k_BT}\int_0^{\infty} dE\,\frac{D^2}{E^2}\cosh^{-2}\left(\frac{E}{2k_BT}\right)\delta\left(E - \sqrt{D^2 + D_0^2\phi^2}\right) \qquad (6.12b)$$

Considering the low-temperature regime, the linear (for weak to moderate magnetic fields) regime for the lowest energy gap, Eq. (6.5), approximates well the true energy gap between the first and second energy levels until some value of the Aharonov-Bohm phase is reached, where the linear approximation begins to break down. The true energy gap $\Delta\mathcal{E} = |\mathcal{E}_1 - \mathcal{E}_0|$ shows a smooth inflection of its curvature away from the linear approximation near $\phi \approx 1$. The "linear" approximation (6.5) is shown in Fig. 6.5 by a dash-dot line. For high magnetic field it is necessary to take into account higher order corrections in ϕ, which are yet analytically tractable. Expanding equation (6.4) to fourth order in θ and ϕ one finds the following next-order approximation:

$$\Delta\mathcal{E} \simeq \sqrt{D^2 + D_0^2\phi^2 - \frac{1}{27}D_0^2\phi^4} \tag{6.13}$$

The new approximation displays one more change of curvature, just like the true gap (dashed line in Fig.6.5), but still breaks down at higher values of ϕ. A higher order term in this expansion would therefore be needed, but would create serious difficulties in the calculations. Moreover, for very large ϕ the gap between levels $\mathcal{E}_0$ and $\mathcal{E}_1$ increases whilst the level $\mathcal{E}_2$ becomes closer to $\mathcal{E}_1$, and that also should be taken into account (see Fig. 6.2).

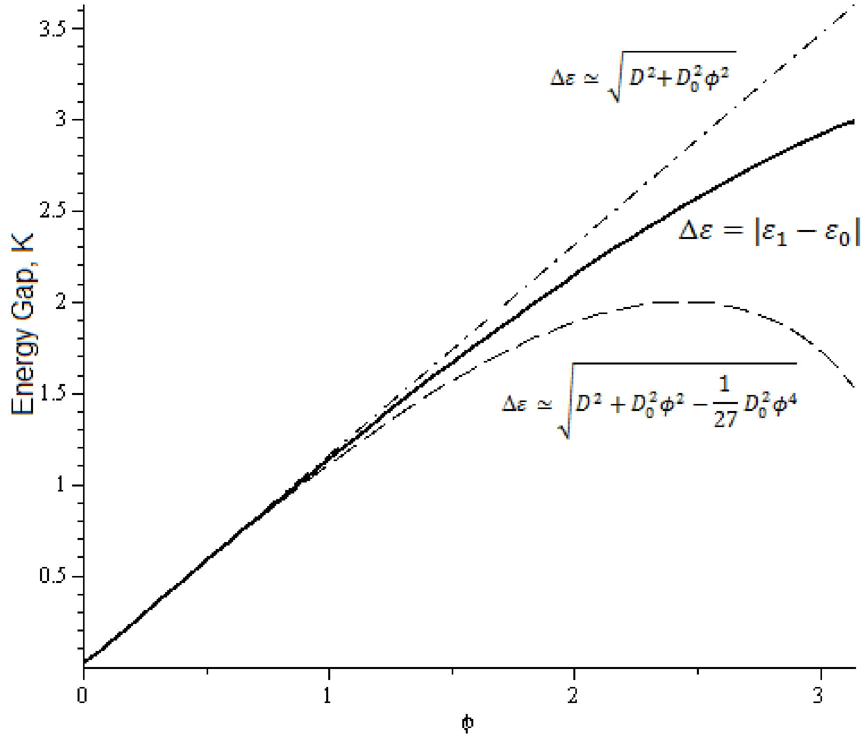

Figure 6.5 – Energy gap as a function of the magnetic AB phase ϕ: solid line – the true gap $\Delta\mathcal{E} = |\mathcal{E}_1 - \mathcal{E}_0|$, dash-dot line – the “linear” approximation (6.5), dashed line – the second order approximation (6.13).

To simplify the ensuing calculations and integration over the distribution function it is thus possible to make the replacement $\phi^2 - \frac{1}{27}\phi^4 = \tilde{\phi}^2$, that gives us the known form:

$$\Delta\mathcal{E} \simeq \sqrt{D^2 + D_0^2\tilde{\phi}^2} \tag{6.14}$$

Considering, that $= 2\pi\frac{\Phi(B)}{\Phi_0} = 2\pi\frac{1}{\Phi_0}\frac{q}{e}BS_\Delta\cos\beta = \frac{2\pi}{\sqrt{2}}\frac{1}{\Phi_0}\frac{q}{e}S_\Delta B = \sqrt{2}\pi\frac{B}{B^*}$ – where we have supposed that the following replacement $\langle\cos^2\beta\rangle = 1/2$ can be made for the orientation averaging, and where $B^* = \frac{\Phi_0}{\frac{q}{e}S_\Delta}$ is a characteristic field value, – we can rewrite $\tilde{\phi}^2$ as:

$$\tilde{\phi}^2 = 2\pi^2\left(\frac{B}{B^*}\right)^2\left(1-\frac{2\pi^2}{27}\left(\frac{B}{B^*}\right)^2\right)$$

$$\tilde{\phi}^2 = 2\pi^2\left(\frac{1}{\Phi_0}\frac{q}{e}S_\Delta\right)^2 B^2\left(1-\frac{2\pi^2}{27}\left(\frac{B}{B^*}\right)^2\right) \qquad (6.15)$$

When the value of the magnetic field becomes of the order of the parameter B^*, then the non-linear approximation makes an effect and the energy gap changes its curvature. The parameter B^* is roughly monitored experimentally and can thus give us some information about the value of the charge q of the fictitious particle and its magnetic-flux threaded surface, S_Δ.

The second order approximation can qualitatively explain the further increase of the dielectric constant and loss at higher magnetic fields, as observed in some of the experiments.

In the next Chapters we will present the results of our theory for the dielectric constant and the dielectric loss in a magnetic field, and for several multi-component glasses.

Chapter 7

Results for the magnetic field dependence of the dielectric constant

The expression of the resonant part of the polarizability (6.12a) should be averaged over the probability distribution of parameters (4.5). Averaging over the probability distribution $\int_{D_{0min}}^{\infty} dD_0 \int dE_1 dE_2 dE_3\ P_{ATS}(\{E_i\}; D_0)\, \delta(E_1 + E_2 + E_3)$ can be simplified as described in Chapter 4 to the expression $\int_0^{2\pi} d\psi \int_{D_{min}}^{\infty} dDD \int_{D_{0min}}^{\infty} dD_0 \frac{P^*}{D_0 D^2} = 2\pi P^* \int_{D_{min}}^{\infty} \frac{dD}{D} \int_{D_{0min}}^{\infty} \frac{dD_0}{D_0}$. Using definition of the energy gap (6.5) the Eq. (6.12a) divides into the sum of two integrals:

$$\alpha_{RES}(T,B) = \frac{\pi}{2} P^* \overline{p_1^2} \int_0^{\infty} dE \frac{1}{E^3} \tanh\left(\frac{E}{2k_B T}\right) \int_{D_{min}}^{\infty} \frac{dD}{D} \int_{D_{0min}}^{\infty} \frac{dD_0}{D_0} [E^2 - D_0^2 \phi^2] \times \delta(E - \Delta\mathcal{E})$$

$$= \alpha_1(T,B) + \alpha_0(T,B)$$

$$\alpha_0(T,B) = \phi^2 \frac{\pi}{2} P^* \overline{p_1^2} \int_0^{\infty} \frac{dE}{E^3} \tanh\left(\frac{E}{2k_B T}\right) \int_{D_{min}}^{\infty} \frac{dD}{D} \int_{D_{0min}}^{D_{0max}} dD_0\, D_0\, \delta(E - \Delta\mathcal{E}) \qquad (7.1a)$$

$$\alpha_1(T,B) = \frac{\pi}{2} P^* \overline{p_1^2} \int_0^{\infty} \frac{dE}{E} \tanh\left(\frac{E}{2k_B T}\right) \int_{D_{min}}^{\infty} \frac{dD}{D} \int_{D_{0min}}^{D_{0max}} \frac{dD_0}{D_0} \delta(E - \Delta\mathcal{E}) \qquad (7.1b)$$

with the energy gap $\Delta\varepsilon = \sqrt{D^2 + D_0^2 \phi^2}$.

We can evaluate the integral over D using the property of the δ-function $\delta(f(D)) = \sum_a \frac{\delta(D - D_a)}{|f'(D_a)|}$, where D_a are the zeroes of $f(D)$, to find:

$$\delta\left(E - \sqrt{D^2 + D_0^2 \phi^2}\right) = E \frac{\delta(D - D_a)}{\sqrt{E^2 - D_0^2 \phi^2}} \qquad (7.2)$$

$$\alpha_0(T,B) = \phi^2 \frac{\pi}{2} P^* \overline{p_1^2} \int_0^{\infty} \frac{dE}{E^3} \tanh\left(\frac{E}{2k_B T}\right) \int_{D_{0min}}^{D_{0max}} dD_0 \frac{E D_0}{\sqrt{E^2 - D_0^2 \phi^2}} \int_{D_{min}}^{\infty} \frac{dD}{D} \delta(D - D_a)$$

where $D_a = \sqrt{E^2 - D_0^2 \phi^2}$,

$$\alpha_0(T,B) = \phi^2 \frac{\pi}{2} P^* \overline{p_1^2} \int\limits_0^\infty \frac{dE}{E^2} \tanh\left(\frac{E}{2k_BT}\right) \int\limits_{-\infty}^{+\infty} \frac{D_0\, dD_0}{E^2 - D_0^2\phi^2}\, \theta(D_0 - D_{0min})$$

$$\times\, \theta(D_{0max} - D_0)\,\theta\left(\frac{1}{\phi}\sqrt{E^2 - D_{min}^2} - D_0\right) \tag{7.3}$$

Similarly to the calculation for the density of states (6.9), the integral (7.3) can be divided into three integrals on the intervals $E < E_{c1}$, $E_{c1} \le E \le E_{c2}$ and $E > E_{c2}$, where $E_{c1} = \sqrt{D_{min}^2 + D_{0min}^2\phi^2}$ and $E_{c2} = \sqrt{D_{0max}^2\phi^2 + D_{min}^2}$. On the interval $E < E_{c1}$ the integral is equal to zero. Carrying out this operation the integral (7.3) can be reduced:

$$\alpha_0(T,B) = \phi^2 \frac{\pi}{2} P^* \overline{p_1^2} \int\limits_{E_{c1}}^{E_{c2}} \frac{dE}{E^2} \tanh\left(\frac{E}{2k_BT}\right) \int\limits_{D_{0min}}^{\frac{1}{\phi}\sqrt{E^2 - D_{min}^2}} \frac{D_0\, dD_0}{E^2 - D_0^2\phi^2}$$

$$+ \frac{\pi}{2} P^* \overline{p_1^2} \int\limits_{E_{c2}}^{\infty} \frac{dE}{E^2} \tanh\left(\frac{E}{2k_BT}\right) \int\limits_{D_{0min}}^{D_{0max}} \frac{D_0\, dD_0}{E^2 - D_0^2\phi^2}$$

$$= \frac{\pi}{2} P^* \overline{p_1^2} \left[\int\limits_{E_{c1}}^{E_{c2}} \frac{dE}{E^2} \tanh\left(\frac{E}{2k_BT}\right) \frac{1}{2} \ln\left(\frac{E^2 - D_{0min}^2\phi^2}{D_{min}^2}\right) \right.$$

$$\left. + \int\limits_{E_{c2}}^{\infty} \frac{dE}{E^2} \tanh\left(\frac{E}{2k_BT}\right) \frac{1}{2} \ln\left(\frac{E^2 - D_{0min}^2\phi^2}{E^2 - D_{0max}^2\phi^2}\right) \right] \tag{7.4}$$

Repeating the previous procedure for $\alpha_0(T,B)$, one obtains the final formula for $\alpha_1(T,B)$:

$$\alpha_1(T,B) = \frac{\pi}{2} P^* \overline{p_1^2} \int\limits_0^\infty \frac{dE}{E} \tanh\left(\frac{E}{2k_BT}\right) \int\limits_{D_{0min}}^{D_{0max}} \frac{dD_0}{D_0} \frac{E}{\sqrt{E^2 - D_0^2\phi^2}} \int\limits_{D_{min}}^{\infty} \frac{dD}{D} \times \delta(D - D_a)$$

$$\alpha_1(T,B) = \frac{\pi}{2} P^* \overline{p_1^2} \int\limits_{E_{c1}}^{E_{c2}} dE \tanh\left(\frac{E}{2k_BT}\right) \int\limits_{D_{0min}}^{\frac{1}{\phi}\sqrt{E^2 - D_{min}^2}} \frac{dD_0}{D_0} \frac{1}{E^2 - D_0^2\phi^2} +$$

$$+ \frac{\pi}{2} P^* \overline{p_1^2} \int\limits_{E_{c2}}^{\infty} dE \tanh\left(\frac{E}{2k_BT}\right) \int\limits_{D_{0min}}^{D_{0max}} \frac{dD_0}{D_0} \frac{1}{E^2 - D_0^2\phi^2}$$

$$= \frac{\pi}{2} P^* \overline{p_1^2} \left[\int\limits_{E_{c1}}^{E_{c2}} \frac{dE}{E^2} \tanh\left(\frac{E}{2k_BT}\right) \frac{1}{2} \ln\left(\frac{(E^2 - D_{0min}^2\phi^2)(E^2 - D_{min}^2)}{D_{0min}^2\phi^2 D_{min}^2}\right) \right.$$

$$\left. + \int\limits_{E_{c2}}^{\infty} \frac{dE}{E^2} \tanh\left(\frac{E}{2k_BT}\right) \frac{1}{2} \ln\left(\frac{D_{0max}^2(E^2 - D_{0min}^2\phi^2)}{D_{0min}^2(E^2 - D_{0max}^2\phi^2)}\right) \right] \tag{7.5}$$

For the whole mass of the glass:

$$\frac{1}{V}\sum_{1}^{N_{ATS}}\left(\alpha_1(T,B)+\alpha_0(T,B)-\alpha(T,0)\right)=\frac{\mathcal{N}_{ATS}}{V}\Delta\alpha=x_{ATS}\Delta\alpha$$

where x_{ATS} - is the concentration of ATS and $\alpha(T,0)$ is:

$$\alpha(T,0)=\frac{\pi}{2}P^{*}\overline{p_1^2}\ln\left(\frac{D_{0max}}{D_{0min}}\right)\int_{E_{c2}}^{\infty}\frac{dE}{E^2}\tanh\left(\frac{E}{2k_BT}\right) \qquad (7.6)$$

The relative change of the dielectric constant is expressed by equations (7.4), (7.5) and (7.6):

$$\frac{\Delta\epsilon'(T,B)}{\epsilon'}=x_{ATS}\frac{\Delta\alpha(T,B)}{\epsilon_0\epsilon_r}=\frac{x_{ATS}}{\epsilon_0\epsilon_r}\left(\alpha_1(T,B)+\alpha_0(T,B)-\alpha(T,0)\right) \qquad (7.7)$$

Equation (7.7) describes well the experimental data for different glasses, as is shown in Figs. (7.1-7.3) and with the fitting parameters presented in Tables (7.1-7.2).

For the sake of clarity, the data and curves in Figs. 7.2 and 7.3 have been shifted apart vertically.

Table 7.1 – Fitting parameters for dielectric constant in a magnetic field for three different types of glasses.

Material and Temperature		$\pi x_{ATS}P^{*}\overline{p_1^2}/\epsilon_r\epsilon_0$	D_{min}, K	$D_{0min}\left\|\frac{q}{e}\right\|S_\Delta$, KÅ^2	$D_{0max}\left\|\frac{q}{e}\right\|S_\Delta$, KÅ^2
BK7 15 mK		$0.089\cdot10^{-5}$	0.03	$1.668\cdot10^{5}$	$4.576\cdot10^{5}$
Duran 15 mK		$0.052\cdot10^{-5}$	0.021	$2.457\cdot10^{5}$	$4.151\cdot10^{5}$
AlBaSiO	50 mK	$0.89\cdot10^{-5}$	0.015	$2.440\cdot10^{5}$	$3.080\cdot10^{5}$
	94 mK	$3.75\cdot10^{-5}$	0.025	$1.225\cdot10^{5}$	$1.589\cdot10^{5}$
	120 mK	$3.09\cdot10^{-5}$	0.0227	$1.767\cdot10^{5}$	$2.248\cdot10^{5}$

Table 7.2 – Fitting parameters for the $SiO_{2+x}C_yH_z$ glass for different temperatures.

Temperature	$\pi x_{ATS}P^{*}\overline{p_1^2}/\epsilon_r\epsilon_0$	D_{min}, K	$D_{0min}\left\|\frac{q}{e}\right\|S_\Delta$, KÅ^2	$D_{0max}\left\|\frac{q}{e}\right\|S_\Delta$, KÅ^2
50 mK	$4.38\cdot10^{-5}$	0.015	$0.076\cdot10^{3}$	$3.047\cdot10^{4}$
70 mK	$12.22\cdot10^{-5}$	0.0486	$0.600\cdot10^{3}$	$2.662\cdot10^{4}$
100 mK	$13.63\cdot10^{-5}$	0.0486	$3.035\cdot10^{3}$	$7.616\cdot10^{4}$

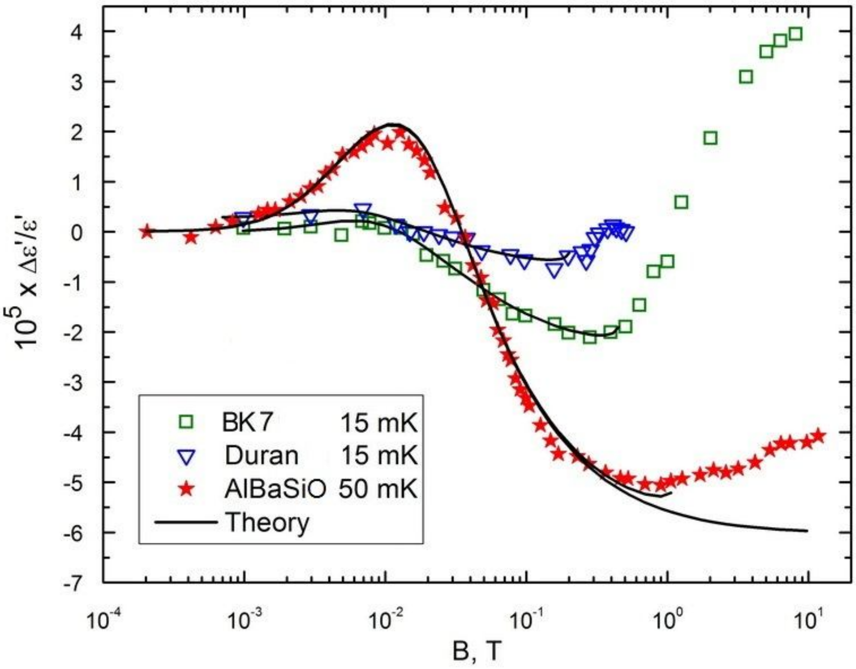

Figure 7.1 – The relative dielectric constant variation as a function of the magnetic field for AlBaSiO [7.1], BK7 [5.5] and Duran [7.1] glasses. With best-fit parameters as in Table 7.1, the curves are the results of our theory in the "weak field" approximation with (and, for AlBaSiO, without) higher order correction.

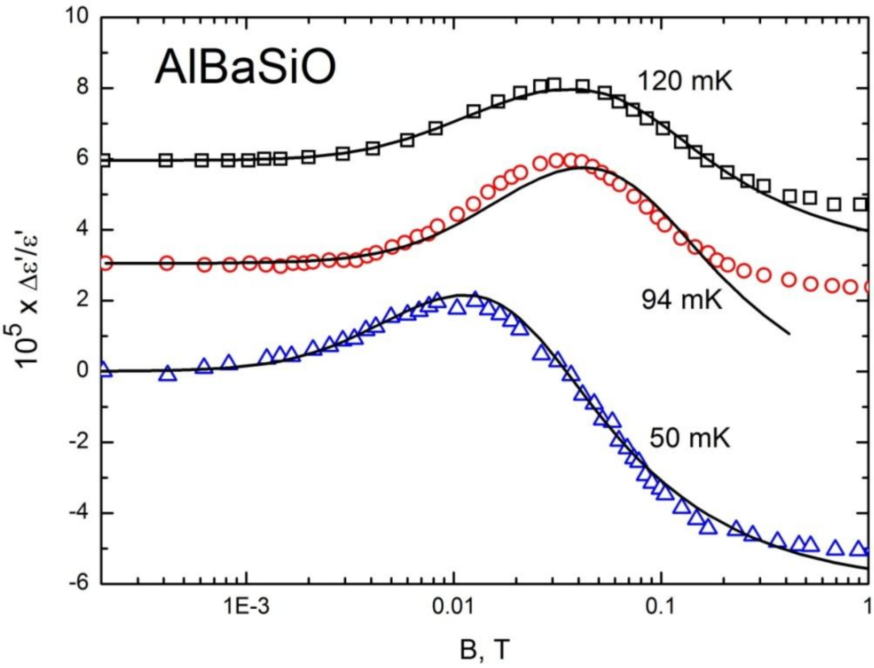

Figure 7.2 – Relative dielectric constant variation as a function of the magnetic field and temperature for AlBaSiO glass [7.1]. With fitting parameters as in Table 7.1, the curves are the result of our theory in the "weak field" approximation.

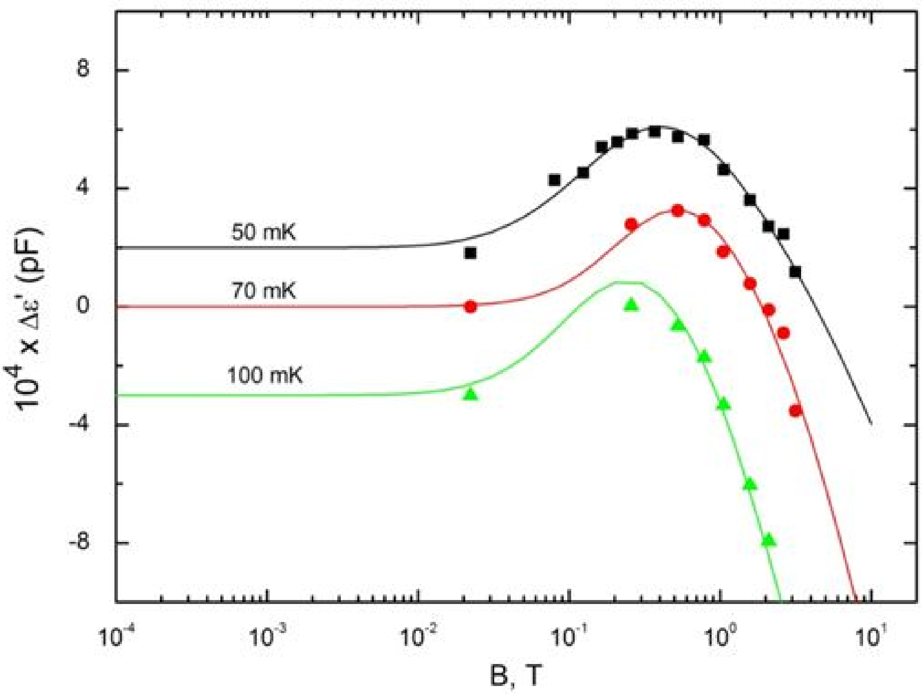

Figure 7.3 – Dielectric constant variation as a function of the magnetic field and temperature for the $SiO_{2+x}C_yH_z$ glass [5.6]. Fitting parameters as in Table 7.2

Chapter 8

Results for the dielectric loss in a magnetic field

The dielectric loss (or loss angle δ) for a dielectric substance is a measure of the power lost in dissipation and is obtained as the following expression:

$$\tan\delta \equiv \frac{\epsilon''}{\epsilon'} \cong \frac{\epsilon''}{\epsilon_0 \epsilon_r} \tag{8.1}$$

where $\epsilon'' = \epsilon_{REL}\frac{\omega\tau}{1+\omega^2\tau^2}$ is the imaginary part of the dielectric constant, typically evaluated in the relaxation time approximation (Chapter 2). It should be pointed out that the 2LS STM does not describe well the temperature- and frequency-dependence of ϵ'' in glasses, as is portrayed in Fig. 8.1. The reason is that the theory works well only in the low-frequency regime. Since $\epsilon''(\omega)$ should be linked to the real part ϵ' of the dielectric constant through the Kramers-Kroning relation :

$$\epsilon''(\omega) = -\frac{2\omega}{\pi}\int_0^\infty d\omega' \frac{\epsilon'(\omega') - 1}{\omega'^2 - \omega^2} \tag{8.2}$$

one can see that the knowledge of the low-frequency behaviour of $\epsilon'(\omega)$ is not enough to reproduce the correct form of $\epsilon''(\omega, T)$. However, inclusion of the ATS contributions does seem to improve the agreement between theory and experiment, as least in the case of BK7, which is probably the best approximation to a fully networked glass.

The relaxation part of the dielectric constant for the whole volume of glass depends on the concentration x_{ATS} of ATS's and is expressed by:

$$\epsilon_{REL} - 1 \cong x_{ATS}\alpha_{REL} \tag{8.3}$$

where α_{REL} should be averaged over all parameters by means of the distribution function (4.5); following similar calculations as in the previous Chapters we get:

$$\alpha_{REL} = \frac{\pi P^* \overline{p_1^2}}{4k_B T}\int_0^\infty \frac{dE}{E^2}\cosh^{-2}\left(\frac{E}{2k_B T}\right)\int_{D_{min}}^\infty \frac{dD_0}{D_0}\int_{D_{0min}}^\infty \frac{dD}{D}D^2$$
$$\times \frac{\omega\tau_{ATS}}{1+\omega^2\tau_{ATS}^2}\delta\left(E - \sqrt{D^2 + D_0^2\phi^2}\right) \tag{8.4}$$

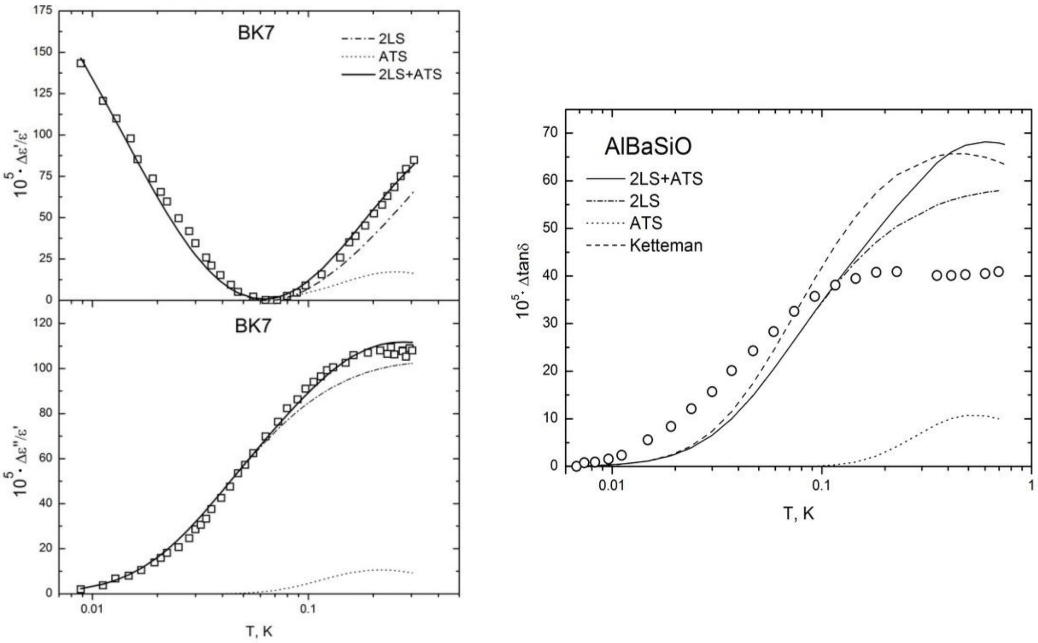

Figure 8.1 – The dielectric loss at 1 kHz for the BK7 and AlBaSiO glasses [7.1]. Fitting parameters for BK7: $A_{2LS} = 215 \cdot 10^{-5}$, $\Delta_{0min} = 3.9$ mK, $\gamma = 0.255 \cdot 10^{-7}\mathrm{sK}^3$ (calculated from [7.1]), $A_{ATS} = 303 \cdot 10^{-5}$, $D_{min} = 0.29$ K, $\Gamma = 0.862 \cdot 10^{-6}\mathrm{sK}^5$. For AlBaSiO the parameters are as from Chapter 4, Table 4.1. "Kettemann" means with parameters from [4.4].

The relaxation time for ATS at low temperature and in a magnetic field is now found to be given by the following expression [4.23]:

$$\tau_{ATS}^{-1} = \tau^{-1}(E,\phi) = \frac{E^3\left(D_0^2\phi^2 + \frac{5}{6}D^2\right)}{\Gamma\tanh\left(\frac{E}{2k_BT}\right)} = \frac{E^3\left(E^2 - \frac{1}{6}D^2\right)}{\Gamma\tanh\left(\frac{E}{2k_BT}\right)} = \tau^{-1}(E,D) \quad (8.5)$$

in which the AB phase ϕ is directly proportional to the magnetic field B. It appears, therefore, that the total dielectric relaxation time, obtained through its inverse:

$$\frac{1}{\tau_{tot}} = \frac{1}{\tau_{2LS}} + \frac{1}{\tau_{ATS}(\phi)} \quad (8.6)$$

must diminish in a non-trivial manner as the magnetic field is switched on. This very interesting prediction of the present theory appears to be confirmed explicitly, albeit only qualitatively, in the laboratory and for some multi-silicate glasses so far only via the work of a Russian group at liquid-He temperatures [8.1]. A systematic study of the magnetic-field dependence of τ_{tot} in the multi-component glasses is still lacking.

The probability distribution function for the ATS dielectric relaxation times turns out to be rather different from that of the standard 2LS case, one finds indeed [4.23]:

$$P(E,\tau) = \frac{\pi P^* \tau_{min}}{5E(\tau - \tau_{min})(\tau_{max} - \tau)} \quad (8.7)$$

(with suitable ϕ -dependent boundaries) where τ_{max} is the maximum ATS relaxation time of Chapter 4 and $\tau_{min} = (5/6)\tau_{max}$. The ATS relaxation-time distribution is therefore very narrow-ranged in τ and also very singular (albeit in the $B = 0$ case only). This has important experimental consequences which will be discussed elsewhere.

It is however not convenient to switch to τ as an integration variable. Then one writes, integrating over D_0 first:

$$\delta\left(E - \sqrt{D^2 + D_0^2\phi^2}\right) = \frac{E}{\phi\sqrt{E^2 - D^2}}\delta\left(D_0 - \frac{1}{\phi}\sqrt{E^2 - D^2}\right) \tag{8.8}$$

Thus the integral (8.4) becomes:

$$\alpha_{REL} = \frac{\pi P^* \overline{p_1^2}}{4k_B T}\int_0^\infty \frac{dE}{E}\cosh^{-2}\left(\frac{E}{2k_B T}\right)\int_0^\infty dD\frac{D}{E^2 - D^2}\frac{\omega\tau_{ATS}}{1 + \omega^2\tau_{ATS}^2}$$
$$\times\,\theta(D - D_{min})\theta\big(D - D_1(E)\big)\theta(D_2(E) - D) \tag{8.9}$$

The integral (8.9) has two special points $D_1(E) = \sqrt{E^2 - D_{0max}^2\phi^2}$ and $D_2(E) = \sqrt{E^2 - D_{0min}^2\phi^2}$, hence $D_1(E) < D_2(E)$. This conditions divide the integral (8.9) into two terms with different intervals in the energy value: $E_{c1} \le E \le E_{c2}$ and $E \ge E_{c2}$, and the integal for $E \le E_{c1}$ vanishes:

$$\alpha_{REL} = \frac{\pi P^* \overline{p_1^2}}{4k_B T}\left[\int_{E_{c1}}^{E_{c2}} \frac{dE}{E}\cosh^{-2}\left(\frac{E}{2k_B T}\right)\int_{D_{min}}^{D_2(E)} dD\frac{D}{E^2 - D^2}\frac{\omega\tau(E,D)}{1 + \omega^2\tau^2(E,D)}\right.$$
$$\left.+\int_{E_{c2}}^{\infty} \frac{dE}{E}\cosh^{-2}\left(\frac{E}{2k_B T}\right)\int_{D_1(E)}^{D_2(E)} dD\frac{D}{E^2 - D^2}\frac{\omega\tau(E,D)}{1 + \omega^2\tau^2(E,D)}\right] \tag{8.10}$$

Substituting (8.5), (8.10) to (8.3) and then to (8.1) we receive the final formula for the dielectric loss variation in a magnetic field:

$$\Delta\tan\delta = \frac{x_{ATS}\pi P^* \overline{p_1^2}}{4\epsilon_0\epsilon_r}\frac{1}{k_B T}\left[\int_{E_{c1}}^{E_{c2}} \frac{dE}{E}\cosh^{-2}\left(\frac{E}{2k_B T}\right)\int_{D_{min}}^{D_2(E)} dD\frac{D}{E^2 - D^2}\frac{\omega\tau(E,D)}{1 + \omega^2\tau^2(E,D)}\right.$$
$$\left.+\int_{E_{c2}}^{\infty} \frac{dE}{E}\cosh^{-2}\left(\frac{E}{2k_B T}\right)\int_{D_1(E)}^{D_2(E)} dD\frac{D}{E^2 - D^2}\frac{\omega\tau(E,D)}{1 + \omega^2\tau^2(E,D)}\right] \tag{8.11}$$

The fitting of relative dielectric loss variation in a magnetic field is shown in Fig. 8.2, using the best-fit parameters from Table 8.1.

One can see that, once again, the experimental data are very well reproduced by the present theory and with fitting parameters very similar to those extracted from the study of the dielectric constant (Chapter 7).

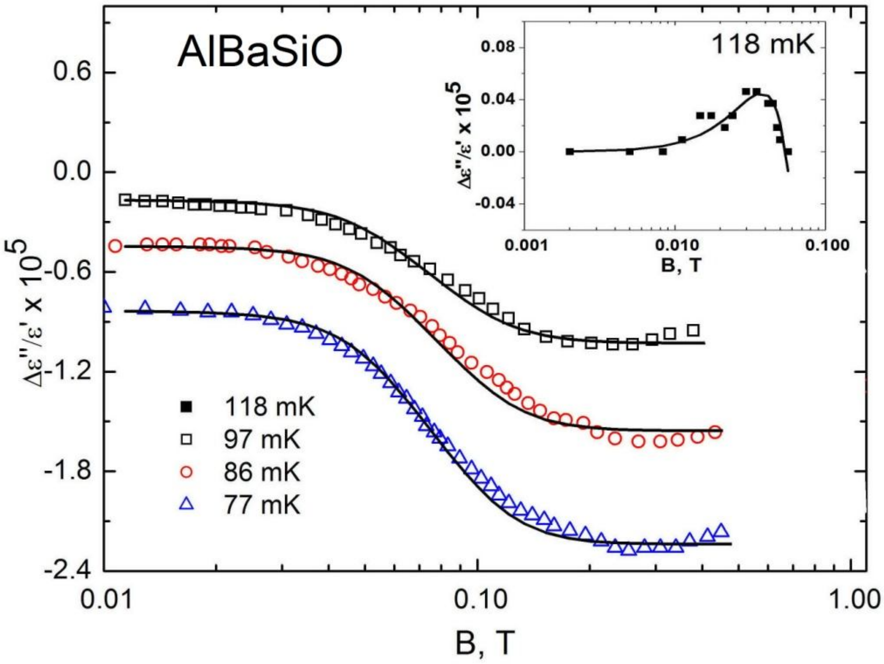

ı)

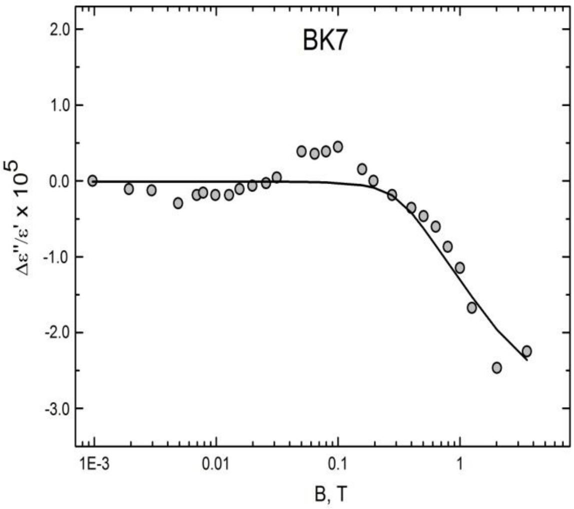

b)

Figure 8.2 – The relative dielectric loss as a function of the magnetic field and temperature in the AlBaSiO (a) and BK7 (b) glasses (data from [7.1]). The continuous curves are from the present theory. In the inset of (a) we show that a faint peak seen experimentally at very weak fields can also be explained by the theory.

Table 8.1 – Fitting parameters for the dielectric loss in a magnetic field in the AlBaSiO and BK7 glasses.

Tempe-rature	$\pi x_{ATS} P^* \overline{p_1^2} / \epsilon_r \epsilon_0$	D_{min}, K	$D_{0min} \left\|\frac{q}{e}\right\| S_\Delta$, KÅ^2	$D_{0max} \left\|\frac{q}{e}\right\| S_\Delta$, KÅ^2	$\Gamma = \gamma' k_B^5$, (sK^5)$^{-1}$
AlBaSiO					
77 mK	$1.54 \cdot 10^{-5}$	0.0209	$1.98 \cdot 10^4$	$4.96 \cdot 10^5$	$5.0 \cdot 10^9$
88 mK	$1.35 \cdot 10^{-5}$	0.0206	$1.98 \cdot 10^4$	$4.96 \cdot 10^5$	$4.0 \cdot 10^9$
96 mK	$1.10 \cdot 10^{-5}$	0.0213	$1.98 \cdot 10^4$	$4.96 \cdot 10^5$	$4.4 \cdot 10^9$
BK7					
15 mK	$2.02 \cdot 10^{-5}$	0.0287	$0.69 \cdot 10^3$	$0.66 \cdot 10^4$	$3.34 \cdot 10^9$

Chapter 9

Results for the dipole-echo in a magnetic field

9.1 The polarization echo experiment

The experimental detection of electric and phonon echoes in glasses has become one strong convincing argument for the two-level systems' existence. Echoes in glasses are similar to other echo phenomena such as spin echo, photon echo etc. But only at very low temperatures the relaxation of the tunneling systems becomes so slow that coherent phenomena like polarization echoes become observable in the insulating glasses.

The essence of the effect is the following (see Fig. 9.1). A glass sample is subjected to two short electromagnetic pulses at the frequency of about 1 GHz separated by a time interval τ_{12}. The duration τ_1 and τ_2 of these pulses should be much shorter that all relaxation processes in the observed system. The macroscopic polarization produced by the first pulse vanishes rapidly due to the distribution of parameters of the tunneling systems in glasses. This phenomenon is similar to the well-known free-induction decay observed in nuclear magnetic resonance experiments. The "phase" (energy-level populations) of each tunneling system develops freely between the two exciting pulses. The second pulse causes an effective time reversal for the development of the phase of the tunneling systems. The initial macroscopic polarization of the glass is recovered roughly at a time τ_{12} after the second pulse. Since the thermal relaxation processes and (see later) spectral diffusion are strongly temperature dependent, polarization echoes in glasses can be observed in practice only at very low temperatures, typically below 100 mK. The echo amplitude is proportional to the number of tunneling systems that are in or near resonance with the exciting microwave pulse and that do not lose their phase coherence during the time $2\tau_{12}$ [9.1].

It should be pointed out that, due to the wide distribution for the parameters of the two-level systems in glasses, the description of polarization echoes in glasses is much more complicated than in the case of nuclear spin systems. In analogy to the two-pulse echo in magnetic resonance experiments this phenomenon is referred to as the spontaneous echo.

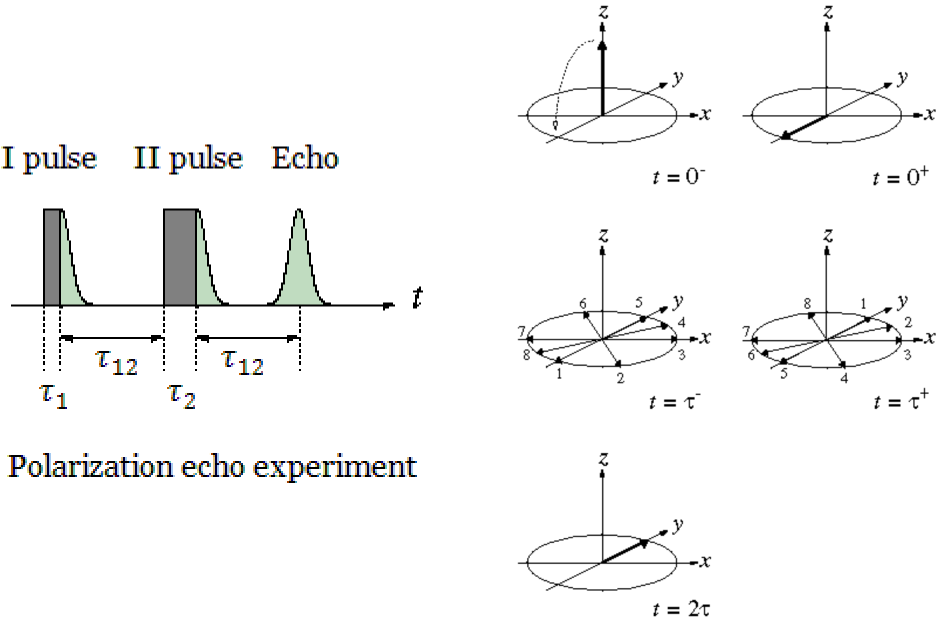

Figure 9.1 – The two-pulse polarization echo experiment. Hahn's vector interpretation on the right hand side is for NMR's spin-echo experiment.

The polarization echo phenomenon can help to understand more about the microscopic structure of tunneling systems in glasses and gives different kinds of information. The amplitude of the echo as a function of the strength of the applied resonant field gives a measure of the induced electric dipole moment, or of the phonon coupling constant. The echo amplitude as a function of pulse separation in a two- or three-pulse experiment can be used to give the relaxation times T_2 (spin-spin) or T_1 (spin-lattice) respectively. The analysis of these experiments follows that for the equivalent magnetic case, except that the TS problem is complicated by three factors. First, the elastic or electric dipoles are not aligned with respect to the driving field and a calculation of the echo signal involves an average over their orientations. Secondly, for a given pumping frequency ω there exists a distribution of induced moments (elastic or electric) and relaxation times, which should be included in the analysis. Finally, in electric echo experiments the local field seen by the TS is not equal to the applied field, and a local-field correction factor must be used when evaluating absolute values of the dipole moment [4.10].

In the polarization echo experiments at radio frequencies and at low temperature of about 10 to 100 mK it has been shown that the tunneling systems in glasses couple directly to the magnetic field [9.2]. Unexpectedly, the amplitude of two-pulse echoes in the AlBaSiO glass was found to be strongly dependent on the applied magnetic field showing a non-monotonic (even oscillatory) field variation. In subsequent papers [5.9, 5.14] such behavior was attributed to the existence of nuclear electric quadrupole moments (NEQM) for some tunneling particles (having nuclear spin $I \geq 1$) interacting with the magnetic field and with gradients of the internal microscopic electric field. The NEQM model is based on the consideration that the levels of tunneling particles with non-zero nuclear quadrupole moment exhibit a quadrupole splitting, which is different in the ground state and in the excited state of a tunneling 2LS. The magnetic field causes an additional Zeeman splitting of these levels giving rise to interference effects. In turn, these effects cause the non-monotonic magnetic field variation of the echo amplitude.

The amplitude (or integrated amplitude) of two-pulse polarization echoes of four types of silicate glasses is shown in Fig. 9.2 (a) as a function of magnetic field [9.2]. In contrast to many other low-temperature properties of glasses the influence of the magnetic field on the amplitude of spontaneous echoes is obviously not universal. BK7 and Duran show similar effects, although the concentration of magnetic impurities differs by at least a factor of 20. Perhaps the most remarkable result of the measurements is the fact that Suprasil I shows no measurable magnetic field effect. While Duran, BAS and BK7 contain nuclei with non-zero nuclear quadrupole moment, Suprasi I is virtually free of such nuclei. This fact is used to provide justification for the nuclear quadrupole model [5.9]. The variation of the echo amplitude with the applied magnetic field is similar for Duran, BK7 and BAS, but not identical. All three samples exhibit a principal maximum at $B = 0$, but only BK7 has a relevant second maximum and a hint to an oscillation in B. At high fields the amplitude of the echo rises above its value at zero magnetic field and seemingly saturates.

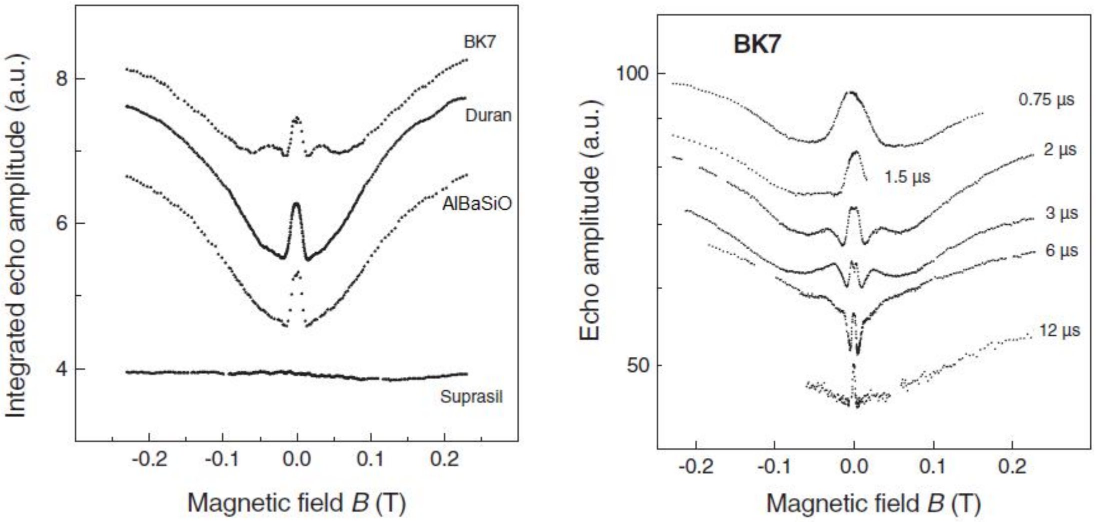

a) b)

Figure 9.2 – a) The integrated echo amplitude as a function of the magnetic field for different silicate glasses: BK7, Duran, AlBaSiO and Suprasil I. All data were taken at 12 mK, $\tau_{12} = 2$ ms, and roughly 1 GHz, except for Duran, where the delay time was $\tau_{12} = 1.7$ ms [9.2]. b) The amplitude of two-pulse echoes in BK7 glass as a function of the magnetic field for different values of the waiting time τ_{12} between pulses. All data sets were taken at 4.6 GHz and 12 mK except that for $\tau_{12} = 2$ ms which was taken at 0.9 GHz. [9.2]

In Fig. 9.2 (b) is shown the amplitude of spontaneous echoes in the BK7 glass as a function of the applied magnetic field for different delay times τ_{12} between the exciting pulses [9.2]. We can see obvious differences for different values of τ_{12}.and that a second maximum (the "oscillation") is not always present.

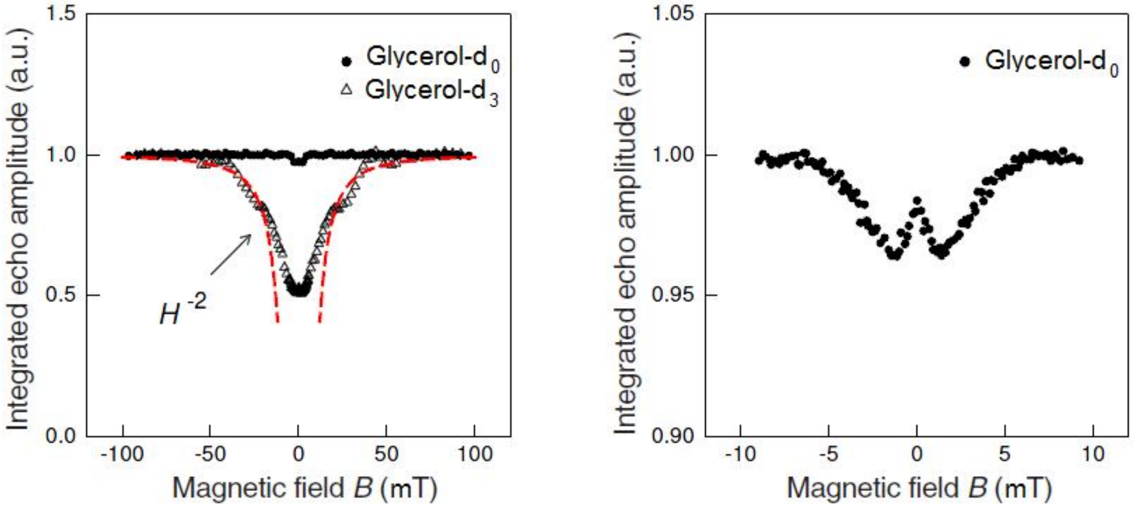

Figure 9.3 – The integrated echo amplitude as a function of the magnetic field at $T = 13$ mK, generated in partially deuterated glycerol (Glycerol-d_3) and ordinary glycerol (Glycerol-d_0.). On the left-hand side the figure shows that the echo amplitude for deuterated Glycerol-d_3 is much more sensitive to the magnetic field in comparison with non-deuterated Glycerol-d_0 shown at the right-hand side [9.3]

The most remarkable fact about the recent experiments on echoes from glasses in a magnetic field is that the magnetic effect is not confined to the inorganic, silicate glasses. Figure 9.3 shows the amplitude of spontaneous echoes in partially deuterated and in ordinary amorphous glycerol as a function of the magnetic field [9.3]. In the case of ordinary glycerol there is very small change of the echo amplitude with B. However, for partially deuterated glycerol a change is much more noticeable, of a different shape and duration. This experiment seemingly provides proof that the magnetic effect is of nuclear origin, for the two amorphous glycerol samples differ in the content of isotopes carrying a NEQM.Glycerol-d_0 has none (other than the natural abundance of deuterium, some 125 ppm, and of ^{17}O, about 500 ppm, concentrations which are however a factor 10 too weak to account for the observed magnetic effect), whilst Glycerol-d_3 contains 37.5% D (I=1) and 62.5% H (I=1/2). However, Glycerol-d_8 (nominally 100% D) displays a magnetic effect that is only 10% larger than in Glycerol-d_3 [9.5], hinting to the fact that the effect does not scale with NEQM concentration.

As reproduced in Fig. 9.4, the integrated echo amplitude as a function of the waiting time τ_{12} in amorphous partially deuterated glycerol-d_5 (that is $C_3O_3H_3D_5$ instead of ordinary $C_3O_3H_8$) shows exponential decay with spectacular oscillations at zero applied magnetic field.

Conversely, all oscillations disappear for the relatively weak magnetic field of 150 mT [9.4, 9.5]. These findings are extraordinary, especially when combined with the observation that for all multi-silicate glasses the oscillations of the echo amplitude in τ_{12} are absent for all values of the magnetic field.

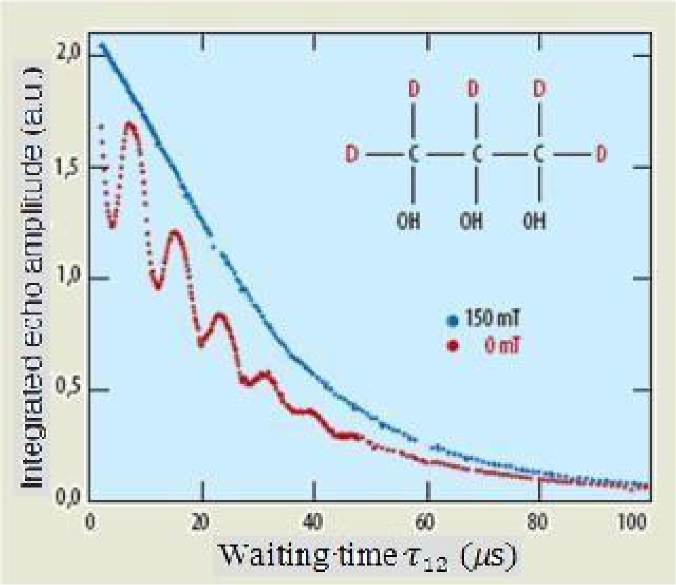

Figure 9.4 – The integrated echo amplitude as a function of the waiting time τ_{12} at zero magnetic field (red curve) and in weak magnetic field 150 mT as generated in deuterated Glycerol-d$_5$ [9.4]

All these findings are collectively hard to explain on the basis of the 2LS STM or starting from more microscopic models and so far only the NEQM has been able to provide the beginning of a rationale for some of these startling experimental results.

9.2 Density matrix formalism for the echo signal

A detailed and general theoretical discussion of spontaneous echoes in glasses has been given by Gurevich *et al.* [9.6] in terms of the density matrix approach for the 2LS STM. Below we reproduce and improve the main result of these Authors.

The contribution to the macroscopic dipole moment of the system from one 2LS is

$$\mathbf{p} = -\mathrm{Tr}\left(\rho \frac{\delta H}{\delta \boldsymbol{F}}\right) \tag{9.1}$$

where ρ is the density matrix averaged over the phonons (the 2LS density matrix) and $\boldsymbol{F} = \boldsymbol{F}_0(t)\cos\omega t$ is the pulsed external electric field. H is the Hamiltonian of the system, which consists of the sum of 2LS's Hamiltonian H_{2LS}, the Hamiltonian H_{int} of the 2LS interaction with the external electric field $F(t)$ and the Hamiltonian H_{ph} of the 2LS-phonon interaction:

$$H = H_{2LS} + H_{int} + H_{ph} \tag{9.2}$$

$$H_{2LS} = \frac{1}{2}\begin{pmatrix} \Delta & -\Delta_0 \\ -\Delta_0 & -\Delta \end{pmatrix},\ H_{int} = \boldsymbol{F} \cdot \mathbf{p}_0 \begin{pmatrix} 1 & 0 \\ 0 & -1 \end{pmatrix},\ H_{ph} = \Lambda_{ik} U_{ik}^{ph} \begin{pmatrix} 1 & 0 \\ 0 & -1 \end{pmatrix} \tag{9.3}$$

where $\mathbf{p}_0 = (1/2)\,\partial\Delta/\partial F$ is the local bare electric dipole, Λ_{ik} is the tensor of strain potential of the 2LS and U_{ik}^{ph} is the strain tensor at the location of the 2LS. Changing Hamiltonian H to its proper diagonal representation, we get:

$$H = \frac{1}{2}\begin{pmatrix} \mathrm{E} & 0 \\ 0 & -\mathrm{E} \end{pmatrix} + \frac{1}{2}\begin{pmatrix} \boldsymbol{\mu} & 2\boldsymbol{\mu}' \\ 2\boldsymbol{\mu}' & -\boldsymbol{\mu} \end{pmatrix} \cdot \boldsymbol{F} + \Lambda_{ik} U_{ik}^{ph} \begin{pmatrix} \Delta/E & \Delta_0/E \\ \Delta_0/E & -\Delta/E \end{pmatrix} \tag{9.4}$$

where $E = \sqrt{\Delta^2 + \Delta_0^2}$, $\boldsymbol{\mu} = 2\Delta\mathbf{p}_0/E$, $\boldsymbol{\mu}' = \Delta_0\mathbf{p}_0/E$

The density matrix can be represented in the form [9.6]:

$$\rho = \begin{pmatrix} n & -ibe^{-i\omega t} \\ ib^* e^{-i\omega t} & 1-n \end{pmatrix} \tag{9.5}$$

where n is the average population of the 2LS upper level and b is the off-diagonal part that is non zero only for the near-resonant 2LS, for which $E \approx \hbar\omega$. Substituting (9.5) to (9.1) one obtains the electric dipole moment:

$$\mathbf{p} = -\frac{1}{2}\mathrm{Tr}\left(\begin{pmatrix} n & -ibe^{-i\omega t} \\ ib^* e^{-i\omega t} & 1-n \end{pmatrix} \cdot \begin{pmatrix} \boldsymbol{\mu} & 2\boldsymbol{\mu}' \\ 2\boldsymbol{\mu}' & -\boldsymbol{\mu} \end{pmatrix}\right) =$$

$$= \frac{1}{2}(1-2n)\boldsymbol{\mu} + 2\boldsymbol{\mu}' i \left(be^{i\omega t} - b^* e^{-i\omega t}\right) =$$

$$= \frac{1}{2}(1-2n)\boldsymbol{\mu} - 2\boldsymbol{\mu}' \mathrm{Im}\left(be^{-i\omega t}\right) \tag{9.6}$$

In the resonant approximation the equations for the density matrix elements of the resonant 2LS are given by the following system [9.7]:

$$\begin{cases} \dfrac{\partial n}{\partial t} = -\bar{\gamma}(n - n_0) - \Omega_R\, \mathrm{Re}(b) & (9.7a) \\ \dfrac{\partial b}{\partial t} = i\left[\dfrac{E(t)}{\hbar} - \omega\right] b - \dfrac{\bar{\gamma}}{2} b + \dfrac{\Omega_R}{2}(2n-1) & (9.7b) \end{cases}$$

where $n_0 = \left(1 + e^{E/k_B T}\right)^{-1}$ is the equilibrium population of the 2LS upper level; $\Omega_R = \Delta_0 \mathbf{p}_0 F_0/\hbar E$ is the Rabi frequency of the resonant 2LS. It characterizes the frequency of coherent oscillations of the level populations under the influence of the resonant perturbation. $\bar{\gamma}$ is the 2LS intrinsic damping due to its interaction with phonons, $\bar{\gamma} = 2\tau^{-1}$ (τ being the phonon relaxation time discussed in Chapter 8). Equations (9.7) for the density matrix take into account spectral diffusion [9.8]. Since the energy of the near-resonant 2LS depends on the strain and on the electric field at its location, the quantum transitions of thermal 2LS cause the spacing of the resonant 2LS levels to fluctuate with time:

$$E(t) = E + \hbar\Delta\omega(t) \tag{9.8}$$

where $\hbar\Delta\omega(t)$ is the contribution to the energy of the resonant 2LS by its interaction with surrounding thermal 2LS. It should be stressed that Eqs. (9.7) are written down in a phenomenological way (using arguments involving the Bloch-like equations discussed in Chapter 2) [9.7] rather than derived from first principles.

The system (9.7) can be solved in the absence of a pump field (between pulses) and in the presence of a pump field when pulses are applied, but in the absence of damping $\bar{\gamma}$ and spectral diffusion $\Delta\omega(t)$:

a) in the absence of a pump field:

$$\begin{cases} \dfrac{\partial n}{\partial t} = -\bar{\gamma}(n - n_0) & (9.9a) \\ \dfrac{\partial b}{\partial t} = i\left[\dfrac{E}{\hbar} - \omega + \Delta\omega(t)\right] b - \dfrac{\bar{\gamma}}{2} b & (9.9b) \end{cases}$$

These are simple first order differential equations and the solution of this system is as following:

$$\begin{cases} n(t) = n_0 + [n(0) - n_0] e^{-\bar{\gamma}t} & (9.10a) \\ b(t) = b(0) \exp\left[-\dfrac{\bar{\gamma}}{2} t + izt + i\displaystyle\int_0^t \Delta\omega(t')dt'\right] & (9.10b) \end{cases}$$

where $z = \frac{E}{\hbar} - \omega$. $n(0)$ and $b(0)$ are initial conditions.

b) in the presence of a pump field, but in the absence of damping $\bar{\gamma}$ and spectral diffusion $\Delta\omega(t)$:

$$\begin{cases} \dfrac{\partial n}{\partial t} = -\Omega_R \operatorname{Re}(b) & (9.11a) \\ \dfrac{\partial f}{\partial t} = izf + \dfrac{F}{2}(2n - 1) & (9.11b) \end{cases}$$

To solve this system it is convenient to represent $b = \varphi + i\eta$ ($\varphi = \operatorname{Re}(b)$):

$$\begin{cases} \dfrac{\partial n}{\partial t} = -\Omega_R \varphi & (9.12a) \\ \dfrac{\partial \varphi}{\partial t} + i\dfrac{\partial \eta}{\partial t} = iz\varphi - z\eta + \dfrac{\Omega_R}{2}(2n - 1) & (9.12b) \end{cases}$$

These two equations can be divided in three, thus simplify to get solutions:

$$\begin{cases} \dfrac{\partial n}{\partial t} = -\Omega_R \varphi & (9.13a) \\ \dfrac{\partial \varphi}{\partial t} = -z\eta + \dfrac{\Omega_R}{2}(2n - 1) & (9.13b) \\ \dfrac{\partial \eta}{\partial t} = z\varphi & (9.13c) \end{cases}$$

and the solutions of this system can be found as:

$$\begin{cases} n(t) = C_1 + \frac{\Omega_R}{\Omega_G} C_2 \cos \Omega_G t - \frac{\Omega_R}{\Omega_G} C_3 \sin \Omega_G t & (9.14a) \\ \varphi(t) = C_2 \sin \Omega_G t + C_3 \cos \Omega_G t & (9.14b) \\ \eta(t) = \frac{z}{\Omega_G} C_3 \sin \Omega_G t - \frac{z}{\Omega_G} C_2 \cos \Omega_G t + \frac{\Omega_R}{z}\left(C_1 - \frac{1}{2}\right) & (9.14c) \end{cases}$$

where C_1, C_2, C_3 are unknown constants. To find these constant we impose $t = 0$ in (9.14) and substitute $b(0) = \varphi(0) + i\eta(0)$ and $b^*(0) = \varphi(0) - i\eta(0)$, thus having three unknown constants and three equations. The solutions for the constants are:

$$\begin{cases} C_1 = n(0) - \frac{\Omega_R^2}{\Omega_G^2}\left(n(0) - \frac{1}{2}\right) + z\frac{\Omega_R}{\Omega_G^2}\frac{b(0) - b^*(0)}{2i} & (9.15a) \\ C_2 = \frac{\Omega_R}{\Omega_G}\left(n(0) - \frac{1}{2}\right) - \frac{z}{\Omega_G}\frac{b(0) - b^*(0)}{2i} & (9.15b) \\ C_3 = \frac{b(0) + b^*(0)}{2} & (9.15c) \end{cases}$$

Substituting system (9.15) to (9.14) remembering that $b = \varphi + i\eta$ one finds after long calculations the final solution for the population n and the off-diagonal part b of the density matrix:

$$\begin{cases} n(t) = n(0) - 2\left[n(0) - \frac{1}{2}\right]\frac{\Omega_R^2}{\Omega_G^2}\sin^2\frac{\Omega_G t}{2} - \frac{\Omega_R}{2\Omega_G} f(0)\left[\sin \Omega_G t + i\frac{2z}{\Omega_G}\sin^2\frac{\Omega_G t}{2}\right] & \\ \qquad - \frac{\Omega_R}{2\Omega_G} b^*(0)\left[\sin \Omega_G t - i\frac{2z}{\Omega_G}\sin^2\frac{\Omega_G t}{2}\right] & (9.16a) \\ b(t) = \frac{\Omega_R}{\Omega_G}\left(n(0) - \frac{1}{2}\right)\left[\sin \Omega_G t + i\frac{2z}{\Omega_G}\sin^2\frac{\Omega_G t}{2}\right] + b(0)\left[\cos \Omega_G t + \frac{\Omega_R^2}{\Omega_G^2}\sin^2\frac{\Omega_G t}{2}\right. & \\ \qquad \left. + i\frac{z}{\Omega_G}\sin \Omega_G t\right] - b^*(0)\frac{\Omega_R^2}{\Omega_G^2}\sin^2\frac{\Omega_G t}{2} & (9.16b) \end{cases}$$

where in all the above equations $\Omega_G = \sqrt{\Omega_R^2 + \mathrm{z}^2}$ is a generalized Rabi frequency.

The duration of the pulses is so short that we can neglect damping and spectral diffusion during the pulses. Assuming that the values at the beginning of the first pulse were $n(0) = n_0$ and $f(0) = 0$ and using the above equations (9.10) and (9.16), at the end of the second pulse we have:

$$n(\tau_1 + \tau_{12} + \tau_2) = n_0 - 2\frac{\Omega_R^2}{\Omega_G^2}\left(n_0 - \frac{1}{2}\right)\sin^2\frac{\Omega_G \tau_1}{2} e^{-\overline{\gamma}\tau_{12}} - 2\frac{\Omega_R^2}{\Omega_G^2}\left(n_0 - \frac{1}{2}\right)\sin^2\frac{\Omega_G \tau_2}{2}$$
$$+4\frac{\Omega_\mathrm{R}^4}{\Omega_\mathrm{G}^4}\left(n_0 - \frac{1}{2}\right)\sin^2\frac{\Omega_G \tau_1}{2}\sin^2\frac{\Omega_G \tau_2}{2} e^{-\overline{\gamma}\tau_{12}} - \frac{\Omega_R^2}{2\Omega_G^2}\left(n_0 - \frac{1}{2}\right)\left[\left(\sin \Omega_G \tau_2 + 2i\frac{z}{\Omega_G}\sin^2\frac{\Omega_G \tau_2}{2}\right)\right.$$
$$\left. \times \left(\sin \Omega_G \tau_1 + 2i\,\frac{z}{\Omega_G}\sin^2\frac{\Omega_G \tau_1}{2}\right) e^{-\frac{\overline{\gamma}}{2}\tau_{12} + iz\tau_{12} + i\int_0^{\tau_{12}} \Delta\omega(t)dt} + c.c.\right] \qquad (9.17a)$$

$$b(\tau_1 + \tau_{12} + \tau_2) = \frac{\Omega_R}{\Omega_G}\left(n_0 - \frac{1}{2}\right)\left(\sin \Omega_G \tau_2 + 2i\frac{z}{\Omega_G}\sin^2\frac{\Omega_G \tau_2}{2}\right)$$

$$-2\frac{\Omega_R^3}{\Omega_G^3}\left(n_0-\frac{1}{2}\right)\sin^2\frac{\Omega_G\tau_1}{2}\left(\sin\Omega_G\tau_2+2i\frac{z}{\Omega_G}\sin^2\frac{\Omega_G\tau_2}{2}\right)e^{-\frac{\bar{\gamma}}{2}\tau_{12}}+\frac{\Omega_R}{\Omega_G}\left(n_0-\frac{1}{2}\right)$$

$$\times\left(\sin\Omega_G\tau_1+2i\frac{z}{\Omega_G}\sin^2\frac{\Omega_G\tau_1}{2}\right)\left(\cos\Omega_G\tau_2+\frac{\Omega_R^2}{\Omega_G^2}\sin^2\frac{\Omega_G\tau_2}{2}+i\frac{z}{\Omega_G}\sin\Omega_G\tau_2\right)$$

$$\times e^{-\frac{\bar{\gamma}}{2}\tau_{12}+iz\tau_{12}+i\int_0^{\tau_{12}}\Delta\omega(t')dt'}-\frac{\Omega_R^3}{\Omega_G^3}\left(n_0-\frac{1}{2}\right)\sin^2\frac{\Omega_G\tau_2}{2}\left(\sin\Omega_G\tau_1-2i\frac{z}{\Omega_G}\sin^2\frac{\Omega_G\tau_1}{2}\right)$$

$$\times e^{-\frac{\bar{\gamma}}{2}\tau_{12}-iz\tau_{12}-i\int_0^{\tau_{12}}\Delta\omega(t')dt'} \qquad (9.17b)$$

The first term in expression (9.6) for **p** makes no contribution to the total dipole moment of the system after averaging over all the orientations of the 2LS dipoles $\mathbf{p}_0$, because the population of the upper level (9.10a) and (9.17a) is an even function of the cosine of the angle between $\boldsymbol{F}_0$ and $\mathbf{p}_0$ and there is no preferred direction in glass.

A contribution to the echo results only from the last term of the off-diagonal component of the density matrix in equation (9.17a). The first two terms and third term in (9.17b) describe the damping of the polarization after the second and first pulse, respectively. And the fourth term determines the echo signal. At any time $t \geq \tau_1+\tau_{12}+\tau_2$ after the second pulse the last term of the off-diagonal component is as follows:

$$b(t-\tau_1-\tau_{12}-\tau_2)=\frac{\Omega_R^3}{\Omega_G^3}\left(n_0-\frac{1}{2}\right)\sin^2\frac{\Omega_G\tau_2}{2}\left(\sin\Omega_G\tau_1-2i\frac{z}{\Omega_G}\sin^2\frac{\Omega_G\tau_1}{2}\right)$$

$$\times\exp\left(-\frac{\bar{\gamma}}{2}\tau_{12}-iz\tau_{12}-i\int_0^{\tau_{12}}\Delta\omega(t')dt'\right)$$

$$\times\exp\left(-\frac{\bar{\gamma}}{2}(t-\tau_1-\tau_{12}-\tau_2)+iz(t-\tau_1-\tau_{12}-\tau_2)+i\int_{\tau_1-\tau_{12}-\tau_2}^{t}\Delta\omega(t')dt'\right)$$

$$b(t-\tau_1-\tau_{12}-\tau_2)=-\frac{\Omega_R^3}{\Omega_G^3}\left(n_0-\frac{1}{2}\right)\sin^2\frac{\Omega_G\tau_2}{2}\left(\sin\Omega_G\tau_1-2i\frac{z}{\Omega_G}\sin^2\frac{\Omega_G\tau_1}{2}\right)$$

$$\times\exp\left(-\frac{\bar{\gamma}}{2}t+iz(t-2\tau_{12})-i\int_0^{t}\Delta\omega(t')s(t')dt'\right) \qquad 9.18)$$

where we have put $s(t)=\begin{cases}+1, & 0<t<\tau_{12}\\ -1, & t>\tau_{12}\end{cases}$.

The contribution to the signal from one resonant 2LS at the time t after the second pulse is obtained by substituting Eq. (9.18) into the second term of Eq. (9.6):

$$\mathbf{p}=-2\boldsymbol{\mu}'\mathrm{Im}\left(b(t-\tau_1-\tau_{12}-\tau_2)e^{-i\omega t}\right)$$

$$=-\frac{2\Delta_0\mathbf{p}_0}{E}\mathrm{Im}\left(-e^{i\omega t}\frac{\Omega_R^3}{\Omega_G^3}\left(n_0-\frac{1}{2}\right)\sin^2\frac{\Omega_G\tau_2}{2}\left(\sin\Omega_G\tau_1-2i\frac{z}{\Omega_G}\sin^2\frac{\Omega_G\tau_1}{2}\right)\right.$$

$$\left.\times\exp\left(-\frac{\bar{\gamma}}{2}t+iz(t-2\tau_{12})-i\int_0^{t}\Delta\omega(t')s(t')dt'\right)\right)$$

$$= -\frac{\Delta_0 \mathbf{p_0}}{E}\mathrm{Im}\left(e^{i\omega t}\frac{\Omega_R^3}{\Omega_G^3}\tanh\left(\frac{E}{2k_BT}\right)\sin^2\frac{\Omega_G\tau_2}{2}\left(\sin\Omega_G\tau_1 - 2i\frac{z}{\Omega_G}\sin^2\frac{\Omega_G\tau_1}{2}\right)\right.$$
$$\left.\times\exp\left(-\frac{\bar{\gamma}}{2}t + iz(t-2\tau_{12}) - i\int_0^t \Delta\omega(t')s(t')dt'\right)\right) \qquad (9.19)$$

Here $n_0 - \frac{1}{2} = \left(1+e^{E/k_BT}\right)^{-1} - \frac{1}{2} = -\frac{1}{2}\tanh\left(\frac{E}{2k_BT}\right)$.

Now we should make the average over the configuration of the 2LS and over parameters of the distribution function (2.8) for 2LSs' to find the dipole moment along the applied electric field:

$$P_{\|} = \int d\Delta_0 d\Delta \frac{\bar{P}}{\Delta_0}\overline{\mathbf{p}\cdot\hat{n}} = \int d\Delta_0 d\Delta\frac{\bar{P}}{\Delta_0}\overline{\mathbf{p}\cdot\hat{n}}\int_0^{\pi}\int_0^{2\pi}\frac{\sin\theta\, d\theta d\varphi}{4\pi} \qquad (9.20)$$

Making the replacing of $y = \cos\theta$ the integration becomes $\int_0^{\pi}\int_0^{2\pi}\frac{\sin\theta d\theta d\varphi}{4\pi} = \int_0^1 dy$. The Rabi frequency can be written as $\Omega_R = \frac{\Delta_0 F_0 \mathrm{p}_0}{\hbar E}\cos\theta = \frac{\Delta_0 F_0}{\hbar E}\mathrm{p}_0 y$, and $\hat{n}$ is a unit vector. We can now find the value of the average dipole moment near $t = 2\tau_{12}$:

$$P_{\|} = \int dE\int d\Delta_0 d\Delta\frac{\bar{P}}{\Delta_0}\int_0^1 dy\, y\frac{\Delta_0 \mathrm{p}_0}{E}\mathrm{Im}\left(\left(\frac{\Delta_0 F_0 \mathrm{p}_0 y}{\hbar E}\right)^3\frac{e^{i\omega t}}{\Omega_G^3}\tanh\left(\frac{E}{2k_BT}\right)\right.$$
$$\times\sin^2\frac{\Omega_G\tau_2}{2}\left(\sin\Omega_G\tau_1 - 2i\frac{z}{\Omega_G}\sin^2\frac{\Omega_G\tau_1}{2}\right)\delta(E-\sqrt{\Delta^2+\Delta_0^2})$$
$$\left.\times\exp\left(-\frac{\bar{\gamma}}{2}t + iz(t-2\tau_{12}) - i\int_0^t \Delta\omega(t')s(t')dt'\right)\right) \qquad (9.21)$$

$$P_{\|} = \int dE\int d\Delta_0 d\Delta\frac{\bar{P}\Delta_0^3 F_0^3 \mathrm{p}_0^4}{\hbar^3 E}\int_0^1 dy\, y^4\,\mathrm{Im}\left(\frac{e^{i\omega t}}{E\Omega_G^3}\tanh\left(\frac{E}{2k_BT}\right)\sin^2\frac{\Omega_G\tau_2}{2}\right.$$
$$\times\left(\sin\Omega_G\tau_1 - 2i\frac{z}{\Omega_G}\sin^2\frac{\Omega_G\tau_1}{2}\right)\exp\left(-\frac{\bar{\gamma}}{2}t\right)\exp\big(iz(t-2\tau_{12})\big)$$
$$\left.\times\exp\left(-i\int_0^t \Delta\omega(t')s(t')dt'\right)\right)\delta(E-\sqrt{\Delta^2+\Delta_0^2}) \qquad (9.22)$$

This result reproduces (and improves) the derivation by Gurevich et al. [9.6]. It should be stressed that the (normalized in $\omega_0 = E/\hbar$) spectral function $\sigma(\omega_0) = \frac{1}{2}\Omega_R^2/\Omega_G^3$ is in practice, for $\Omega_R \ll \omega$, very narrowly centered at the pumping frequency ω and can therefore be replaced by a Dirac's $\delta(\omega_0 - \omega)$, thus resulting in the strictly-resonant approximation which is normally employed. Things change considerably, however, when the density of states $\mathrm{g}(E)$ is non-uniform, as is the case for the ATS model.

9.3 The polarization echo in a magnetic field: Schrödinger equation formalism

The above result for the echo signal from a collection of 2LS can also be obtained - and from first principles - from a lengthy but straightforward Schrödinger equation treatment in which high-frequency modes are neglected and phonon-damping is treated in a phenomenological way [9.9]. In the most rigorous way, one obtains for the echo signal:

$$\wp_{\|}(t) = \wp_{+}(t)\cos(\omega\Delta\tau) - \wp_{-}(t)\sin(\omega\Delta\tau) \qquad (9.23)$$

where $\Delta\tau = \tau_2 - \tau_1$ (whence $\omega\Delta\tau$ typically as large as 10^2) and where:

$$\wp_{+}(t) = \mathrm{p}_{0\|}\frac{\Delta_0}{E}\tanh\left(\frac{E}{2k_BT}\right)e^{-\frac{\bar{\gamma}t}{2}}\left(\frac{\Omega_R}{\Omega_G}\right)^3 \mathrm{Im}\left\{\sin^2\left(\frac{\Omega_G\tau_2}{2}\right)\left[\sin(\Omega_G\tau_1)\right.\right.$$
$$\left.\left. - 2i\frac{\omega_0-\omega}{\Omega_R}\sin^2\left(\frac{\Omega_G\tau_1}{2}\right)\right]e^{i\omega_0(t-2\bar{\tau}_{12})-i\int_0^t \Delta\omega(t')s(t')dt'}\right\} \qquad (9.24a)$$

$$\wp_{-}(t) = \mathrm{p}_{0\|}\frac{\Delta_0}{E}\tanh\left(\frac{E}{2k_BT}\right)e^{-\frac{\bar{\gamma}t}{2}}\left(\frac{\Omega_R}{\Omega_G}\right)^3 \mathrm{Re}\left\{\sin^2\left(\frac{\Omega_G\tau_2}{2}\right)\left[\sin(\Omega_G\tau_1)\right.\right.$$
$$\left.\left. - 2i\frac{\omega_0-\omega}{\Omega_R}\sin^2\left(\frac{\Omega_G\tau_1}{2}\right)\right]e^{i\omega_0(t-2\bar{\tau}_{12})-i\int_0^t \Delta\omega(t')s(t')dt'}\right\} \qquad (9.24b)$$

in which $2\bar{\tau}_{12} = \tau_1 + \tau_{12} + \tau_2 + \tau_{12} \approx 2\tau_{12}$ is the total elapsed time at the echo signal's centre. The above Eq. (23) gives the expectation value of the polarization per TS in the direction of the applied electric field. It still needs to be averaged wrt all STM parameter distribution and over a uniform orientational distribution of 2LS dipoles $\mathbf{p}_0$. $\frac{\bar{\gamma}}{2} = \tau^{-1}$ is again the phonon relaxation rate (Chapter 8). If $\omega\Delta\tau$ is neglected, then Eq. (9.22) (after averaging) is recovered for $P_{\|} = \overline{\wp_{\|}}$.

We are now in a position to extend [4.23] the polarization echo's theory to the case of the ATS model describing glasses in a magnetic field; the point of view will be taken that a background of ordinary 2LS's - insensitive to the magnetic field.- also exists in the glass.

One starts with a collection of 3LS ($n_w = 3$ is always computationally convenient) as in the previous Chapters, but with the single ATS Hamiltonian written in the energy representation:

$$H' = SHS^{-1} = \begin{pmatrix} \varepsilon_0 & 0 & 0 \\ 0 & \varepsilon_1 & 0 \\ 0 & 0 & \varepsilon_2 \end{pmatrix} + S\begin{pmatrix} -\mathbf{p}_1\cdot\mathbf{F} & 0 & 0 \\ 0 & -\mathbf{p}_2\cdot\mathbf{F} & 0 \\ 0 & 0 & -\mathbf{p}_2\cdot\mathbf{F} \end{pmatrix}S^{-1} \qquad (9.25)$$

where the diagonalizing matrix $S = S(\phi)$ is magnetic-field dependent, the ε_i are the (B-dependent) ATS energy levels and the $\mathbf{p}_i$ are the wells' electric dipoles.As in the treatment of Gurevich *et al.* [9.6] there is also a phonon bath, but this will be treated - as always -

phenomenologically resulting in a phonon-damping exponential. The second term in Eq. (9.25) causes irrelevant energy-level shifts and produces an extra matrix term $\Delta H'(t) = (A_{ij})$ of which the only relevant element (see below) is

$$A_{01} = A_{10}^{*} = \sum_{k=1}^{3} -\mathbf{p}_k \cdot \mathbf{F}_0 \, \mathrm{S}_{0\mathrm{k}}(\phi)\mathrm{S}_{1\mathrm{k}}^{*}(\phi) \, \cos\omega t \qquad (9.26)$$

The A_{ij} cause transitions between the ATS levels 0, 1, 2 when the pulses are applied. In the weak magnetic field limit (most appropriate for the echo experiments) and in the approximation $D \ll D_0$ that we always use (and that is always confirmed by out best fits to the data), one quickly discovers that the second excited level remains unperturbed and one can make use of the "effective 2LS approximation" (where, however, the ground-state wavefunctions of the three wells mix). One can then repeat the Schrödinger equation (or density-matrix, for that matter) calculation carried out for the 2LS case, at the cost of introducing a complex Rabi frequency:

$$\Omega_0 = A_{01}/\hbar \qquad (9.27)$$

The evolution of the generic ATS during and in the absence of pulses can then be followed in much the same way as before, except that in order to simplify the formalism it is convenient to introduce from the outset an orientationally-averaged Rabi frequency (now a real quantity):

$$\Omega_R = \sqrt{\overline{|\Omega_0|^2}} \qquad (9.28)$$

the bar denoting the average wrt 3LS base-triangle's orientations. Replacing Ω_0 with Ω_R before carrying out the averaging of the sample's polarization is our main approximation, allowing for a considerably simplified treatment and leading to the magnetic-field dependent expression [4.23]:

$$\Omega_R = \frac{\mathrm{p}_1 \mathrm{F}_0}{\hbar} \sqrt{\frac{D_0^2\phi^2 + \frac{5}{6}D^2}{6E^2}} \qquad (9.29)$$

Here, p_1 is a single-well (averaged) electric dipole and $E = \hbar\omega_0 = \sqrt{D^2 + D_0^2\phi^2}$ is the usual magnetic-field dependent lower energy gap in the weak field approximation. The above approximation for Ω_0 treats incorrectly the ATS's that have $\mathbf{F}_0$ roughly orthogonal to the ATS base triangle; luckily these have $\Omega_0 \approx 0$ and do not contribute to the echo signal.

Proceeding as for the derivation of Eq. (9.23) [9.9] one finds that there is a magnetic contribution to the (partly averaged) polarization of the sample from the generic ATS given by [4.23]:

$$\Delta\wp_{\parallel}(t) \cong -\frac{\hbar}{\mathrm{F}_0}\tanh\left(\frac{E}{2k_BT}\right)e^{-\frac{\bar{\gamma}}{2}t}\frac{\Omega_R^4}{\Omega_G^3}\mathrm{Im}\left\{\sin^2\left(\frac{\Omega_G\tau_2}{2}\right)\left[\sin(\Omega_G\tau_1)\right.\right.$$
$$\left.\left. -\, 2i\frac{\omega_0-\omega}{\Omega_R}\sin^2\left(\frac{\Omega_G\tau_1}{2}\right)\right]e^{i\phi(t)-i\int_0^t\Delta\omega(t')s(t')dt'}\right\} \qquad (9.30)$$

Now, $\frac{\bar{\gamma}}{2}=\tau^{-1}$ is the magnetic ATS phonon relaxation rate given by Eq. (8.4), the generalized Rabi frequency is again given by $\Omega_G=\sqrt{\Omega_R^2+(\omega_0-\omega)^2}$ and:

$$\phi(t)=\omega_0(t-2\bar{\tau}_{12})+\omega\Delta\tau \qquad (9.31)$$

is the appropriate time argument. From this, it is obvious that the time at which all ATS (regardless of their energy gap $E=\hbar\omega_0$) will be refocused is $t=2\bar{\tau}_{12}$ and this determines the echo's peak position.

The measured echo amplitude's contribution from the magnetic ATS is therefore (allowing for an arbitrary amplification factor A_0):

$$\Delta A(\phi)=A_0\frac{d}{\varepsilon_0\varepsilon_r}x_{ATS}2\pi P^*\int_0^\infty dE\int\frac{dD}{D}\int\frac{dD_0}{D_0}\Theta(D,D_0)$$
$$\times\,\delta\left(E-\sqrt{D^2+D_0^2\phi^2}\right)\Delta\wp_{\parallel}(2\bar{\tau}_{12}) \qquad (9.32)$$

where d is the sample's thickness, $\Theta(D,D_0)$ is the usual theta-function restriction for the integration domain (previous Chapters) and where a final orientational averaging wrt the angle $\beta=\widehat{\mathbf{BS}_\Delta}$ (defining the Aharonov-Bohm phase ϕ, see Eq. (6.2)) is in order. At this point one deals with the delta-function's constraint and the energy parameters integrations in the usual way, to arrive at, after a lengthy calculation:

$$\Delta A(\phi)\cong -A_0\frac{d}{\varepsilon_0\varepsilon_r}x_{ATS}\frac{4\pi\hbar^2P^*}{\mathrm{F}_0}\cos(\omega\Delta\tau)$$
$$\times\left\{\int_{E_{c_1}}^{E_{c_2}}\frac{dE}{E}\int_{D_{min}}^{D_2(\phi)}\frac{dD}{D}\tanh\left(\frac{E}{2k_BT}\right)\frac{E^2}{E^2-D^2}e^{-w2\bar{\tau}_{12}}\Omega_R^2\sigma(E)[\mathrm{S}(\theta_1,\theta_2)\tan(\omega\Delta\tau)\right.$$
$$\left.+\,\mathrm{C}(\theta_1,\theta_2)]+\int_{E_{c_2}}^{\infty}\frac{dE}{E}\int_{D_1(\phi)}^{D_2(\phi)}\frac{dD}{D}\,(\ldots\text{same integrand as above}\ldots)\right\} \qquad (9.33)$$

where we have defined the functions:

$$\sigma(\mathrm{E})=\frac{\Omega_{\mathrm{R}}^2}{2\hbar\Omega_{\mathrm{G}}^3}=\frac{\Omega_R^2}{2\hbar(\Omega_R^2+(\omega_0-\omega)^2)^{3/2}}$$
$$\mathrm{S}(\theta_1,\theta_2)=\sin(\Omega_G\tau_1)\sin^2(\Omega_G\tau_2/2) \qquad (9.34)$$
$$\mathrm{C}(\theta_1,\theta_2)=-2\frac{\omega_0-\omega}{\Omega_R}\sin^2(\Omega_G\tau_1/2)\sin^2(\Omega_G\tau_2/2)$$

with $\theta_{1,2} = \Omega_G \tau_{1,2}$ the so-called pulse areas. $E_{c_{1,2}}$ are as in the previous Chapters, whilst $D_{1,2}(\phi) = \sqrt{E^2 - D_{0max,min}^2 \phi^2}$ and $E = \hbar\omega_0$.

In going from Eq. (9.30) to (9.33) we have tacitly made some assumption on the (fully averaged) spectral diffusion term $e^{-i\int_0^{2\bar{\tau}_{12}} \Delta\omega(t')s(t')dt'}$. The theory of spectral diffusion (SD) for the magnetic multi-welled ATS is a chapter still open, however we can safely assume that what was found by many Authors for NMR's spin-echoes [9.8] and for the 2LS polarization echoes in glasses [9.7, 9.10] holds for the ATS as well. Namely, that there is a wide range of waiting times where the decay of the echo amplitude is a simple exponential in τ_{12} so that one can replace the SD term with $e^{-2\bar{\tau}_{12}/\tau_\phi}$, where $\tau_\phi(T)$ is a SD characteristic time depending only on temperature. There must be a SD time τ_ϕ for the ATS as well as a SD time τ_ϕ for the standard 2LS. For the latter, theory shows [9.7, 9.10] that this parameter is independent of the energy gap E and thus for the ATS we shall assume the same and, moreover, that (like for the phonon damping rate and Rabi frequency) its dependence on the magnetic field is weak or absent. This allows us to lump the SD problem together with phonon damping, yielding an overall exponential relaxation rate:

$$w(E,D) = \tau_\phi{}^{-1} + \tau^{-1}(E,D) \qquad (9.35)$$

in which the SD time is typically much shorter than the phonon-damping time τ and depends only on temperature through [9.11, 9.12]:

$$\tau_\phi{}^{-1} = c_{ATS}T \qquad (9.36)$$

with c_{ATS} an appropriate constant. The assumption of an overall simple-exponential decay of the echo amplitude with τ_{12} is well verified experimentally [9.11, 9.3].

We now make use of Eq. (9.33) to fit the experimental data for the multi-silicates, the idea being that the total amplitude is $A(\phi) = A_{2LS} + \Delta A(\phi)$ (which must be averaged wrt the ATS magnetic orientation angle β).

Fig. 9.5 shows the experimental results for the relative echo amplitude in AlBaSiO as a function of the magnetic field; values of B up to 0.6 T have been explored and for three temperatures [9.2]. The data are fitted with our theory with parameters as reported in Table 9.1. The agreement between theory and experiment is highly satisfactory, given the simplifications used in the theory. There is only one minimum in $A(B)$ and the inset in Fig. 9.5 shows that again it is the ATS density of states (DOS) that is responsible for the magnetic effect (Chapter 6). Indeed, by enforcing the strict-resonance condition $\sigma(E) \to \delta(E - \hbar\omega)$ expression (9.33) collapses to a quantity very much like the DOS (convoluted with slow-varying corrections) and with the same behaviour, thus reproducing the main shape of $\Delta A(B)$.

It is the non-resonant convolution of this quasi-DOS with other E-dependent functions that produces the rounding of the minimum and the B^{-2} saturation. Interestingly, though $\tau_\phi \ll \tau$, the phonon-damping term plays a main role in the rounding of the high-B tail to a B^{-2} (as observed) saturation. The ATS approach predicts also a linear in B intermediate decay regime of the echo amplitude, and this is often experimentally observed [9.2, 9.3].

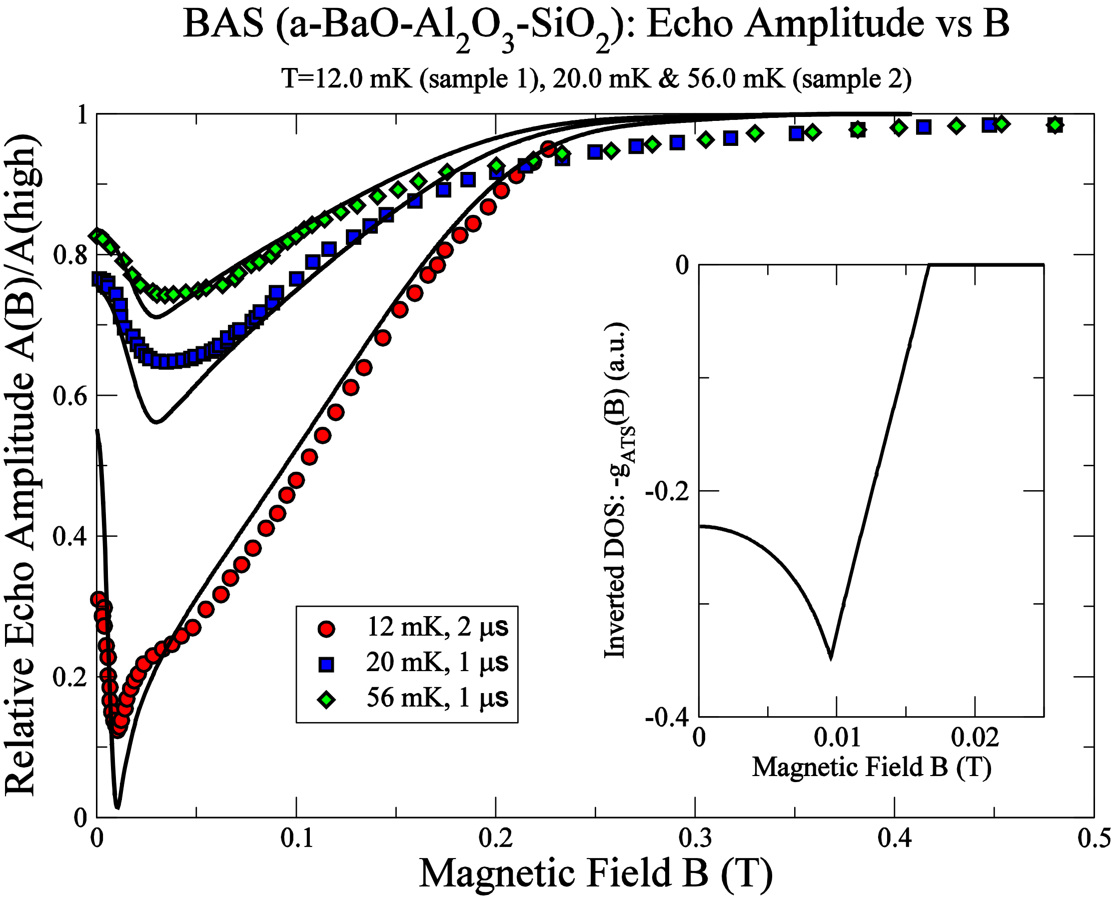

Fig. 9.5 – Magnetic field dependence of the polarization echo amplitude (relative to its value at "high" fields where saturation occurs) for the AlBaSiO glass [9.2] (also referred to as BAS) at given experimental conditions. We believe two separate samples have been used. Continuous curves from our theory. Nominal frequency 1 GHz, $\tau_2 = 2\tau_1 = 0.2$ μs. Inset: behaviour of the ATS DOS for the same parameters (the physical origin of the effect).

Next, in Fig. 9.6 we present the comparison of theory and experiment for data for the echo amplitude in BK7 (good optical glass, hence devoid of microcrystals) at two different values of the waiting time τ_{12}. It is remarkable how our theory, despite the simplifications and the total absence of multi-level physics (as advocated by the NEQM approach), can reproduce all the features of the experimenatl data, including every change of curvature in $A(B)$. A rough fit, not aiming at high χ^2 agreement, reproduces the two maxima (and minima) that the NEQM approach takes as indication of the multiple (rapid) oscillations ensuing from the quantum beatings due to the Zeeman- and NEQM-splitting of the generic 2LS [5.8]. There are never more than two observed minima, in practice, and these can be reproduced by our simple ATS model.

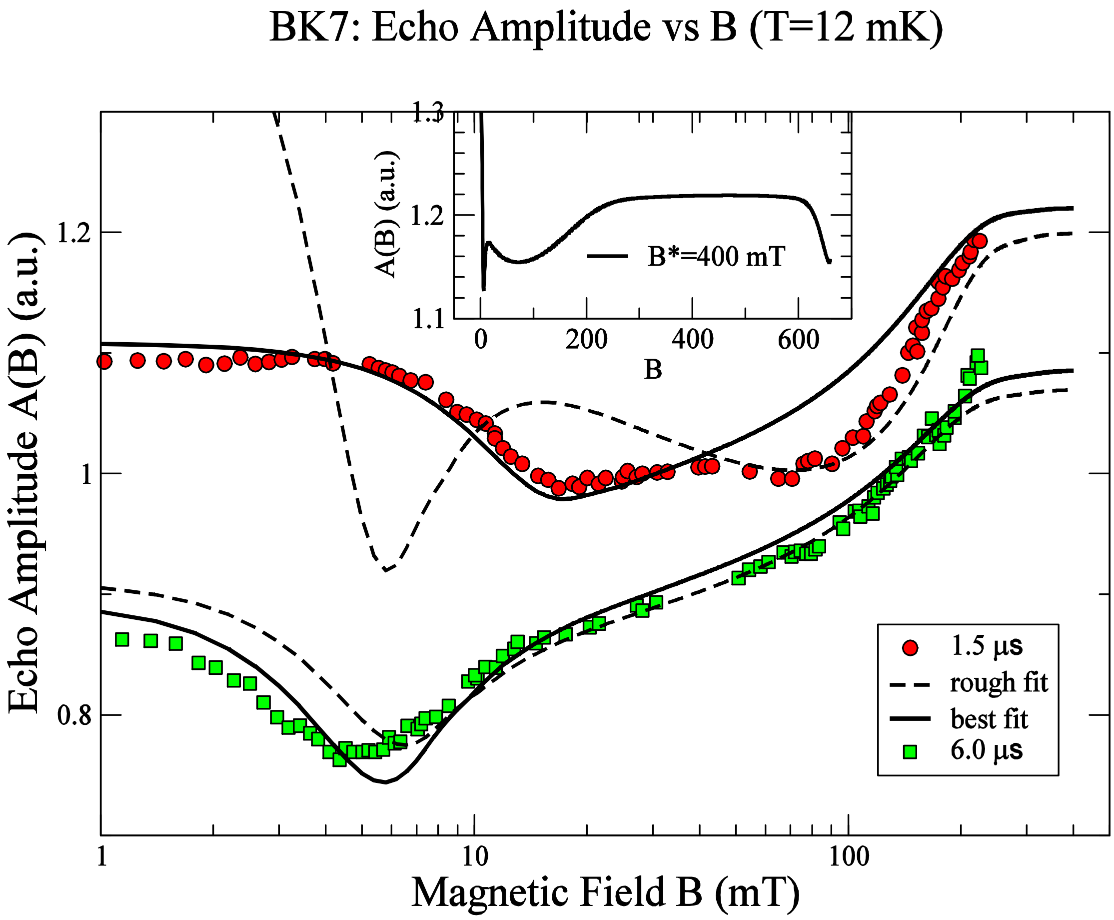

Fig. 9.6 – Magnetic field dependence of the polarization echo amplitude for the BK7 glass [9.2] at given experimental conditions. Dashed curves (rough fit) and continuous curves from our theory; there are no more than two observable maxima or minima (no true oscillations). Nominal frequency 0.9 GHz, $\tau_2 = 2\tau_1 = 0.2$ μs. Inset: our prediction for the higher magnetic field regime (B^* as defined in Chapter 6).

Finally, in the inset of Fig. 9.6, we show what the experimentalists missed by not exploring higher magnetic-field values. Using the simple-minded correction for the lower energy gap at higher fields, we plot the expected behaviour of $A(B)$ for intermediate fields. After the two minima, there is only an apparent saturation and new interesting features should characterise $A(B)$ at higher fields ($B > 600$ mT), just like it happens for the dielectric constant. A full description of the effect, however, requires a calculation involving all three ATS energy levels.

Table 9.1 – Fitting parameters for the echo amplitude’s magnetic field dependence

Glass type	D_{min} mK	$D_{0min} \left\|\frac{q}{e}\right\| S_{\Delta}$ KÅ^2	$D_{0max} \left\|\frac{q}{e}\right\| S_{\Delta}$ KÅ^2	Γ^{-1} $(\mu\text{s K}^5)^{-1}$	$c_{ATS} - c_{2LS}$ $(\mu\text{s K})^{-1}$	p_1F_0 D kV m^{-1}	$\tan \omega\Delta\tau$
AlBaSiO (sample 1)	17.74	0.95×10^3	2.13×10^4	9.22×10^6	5.008	0.461	0.247
AlBaSiO (sample 2)	27.20	1.14×10^3	8.96×10^3	2.57×10^5	3.825	0.450	0.245
BK7 (1.5 μs)	16.76	0.92×10^3	1.34×10^4	8.91×10^6	1.03 (*)	0.60	0.207
BK7 (6 μs)	15.94	0.89×10^3	3.31×10^4	3.25×10^6	5.72 (*)	0.98	0.204

(*) For BK7 (best-fit parameters only), c_{ATS} only is involved.

9.4 Amorphous glycerol and the so-called isotope effect

We now come to the astonishing case of amorphous glycerol ($C_3O_3H_8$ vitrifies around 47 K), deuterated and natural. The first question is whether our model applies to this system, which nominally is single-component. We firmly believe it does and therefore that the *a*-glycerol polarization echo experiments can also be explained by the presence of microphasing in the samples.

In Brandt’s Ph.D. Thesis [9.3] it is reported that the liquid glycerol, from which the glass samples were made of, were contaminated by water (see Table 2). Moreover, experiments on samples with different deuterium molar content and different before-cooling open-air shelf-storage times gave definitely different results. The available experimental data [9.3] are reported in Fig. 9.7. One observes a much greater variation in the experimental data for the $C_3O_3D_3H_5$ samples left in the air before freezing than in the similiarly prepared $C_3O_3D_5H_3$ samples.

Table 9.2 – Purity and water-contents data for the studied glycerol samples [9.3]

Sample	Chemical purity	Water content
Glycerol-d_0	99.9%	
Glycerol-d_3	99%	≤ 1.5% H_2O
Glycerol-d_5	98%	≤ 0.11% H_2O
Glycerol-d_8	98%	no information

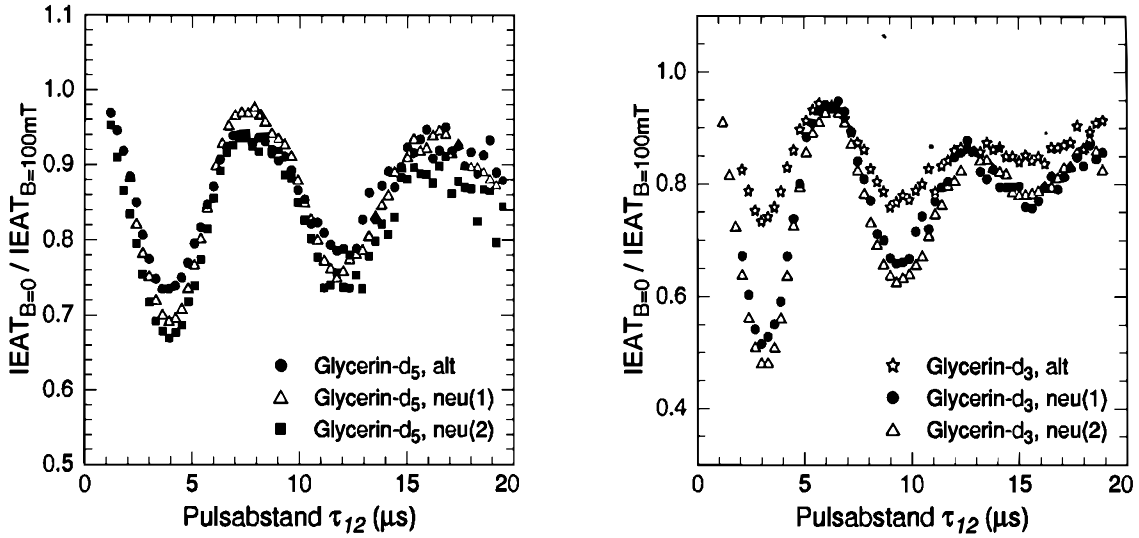

Fig. 9.7 – Relative integrated echo amplitude vs. τ_{12} for various deuterated amorphous glycerol samples at $B = 0$, nominal frequency 0.85 GHz, T =13.5 mK [9.3]. The samples termed “old” (alt) were left liquid several days in the air before cooling; two separate fresh preparations (neu(1) and neu(2)) were also employed, obtained from producer-sealed containers just before cooling.

Glycerol is a highly hygroscopic substance, owing to the polarity (similar to H_2O’s) of its molecules which tend to shed one of the three hydrogens (or deuteria) attached to the oxygens, but none of those firmly attached to the carbon atoms. The equilibrium process is of the type, e.g., $C_3O_3D_3H_5 \leftrightarrow C_3O_3D_2H_5^- + D^+$ causing similar equilibrium concentrations as in the familiar dissociation process $H_2O \leftrightarrow OH^- + H^+$. Thus it is not unreasonable to imagine that the water contained in the air causes some hydrogens to substitute for some O-attached deuteria, in time, when absorbed in liquid Glycerol-d$_3$, - but not in the case of Glycerol-d$_5$ The Glycerol-d$_3$ hygroscopic effect on the echo would support the NEQM theory, but the (albeit smaller) effect in Glycerol-d$_5$ does not. Moreover, oddly enough the more hygroscopically contaminated samples (“alt”) yield the smaller effect on the echo’s amplitude oscillations, whilst the fresher samples (“neu” (1) and (2)) give wider and different (neu(1) $\neq$ neu(2)) amplitude oscillations.

The lack of reproducibility of the effect leads us to believe that the origin of the observed magnetic phenomena lies again in the formation of microcrystallites during the freezing process, which in glycerol are nucleated by the presence of dissociated H_2O. The concentration of micro- or nano-crystals is therefore very much sample-dependent. To test these ideas, we have applied our theory for the V-shaped dielectric constant’s temperature-dependence (Chapter 4) to the only complete data available for Glycerol-d$_3$ [9.3], though the frequency of the applied electric field (0.863 GHz, nominally) is huge (as it turns out, however, the 2LS STM approach can still explain the resonant part of the data [9.3, 9.13]).

Fig. 9.8 (a) shows our best fit to the data, the relaxation part being reproduced only by means of the 2LS+ATS approach and with the parameters given in Table 9.3.

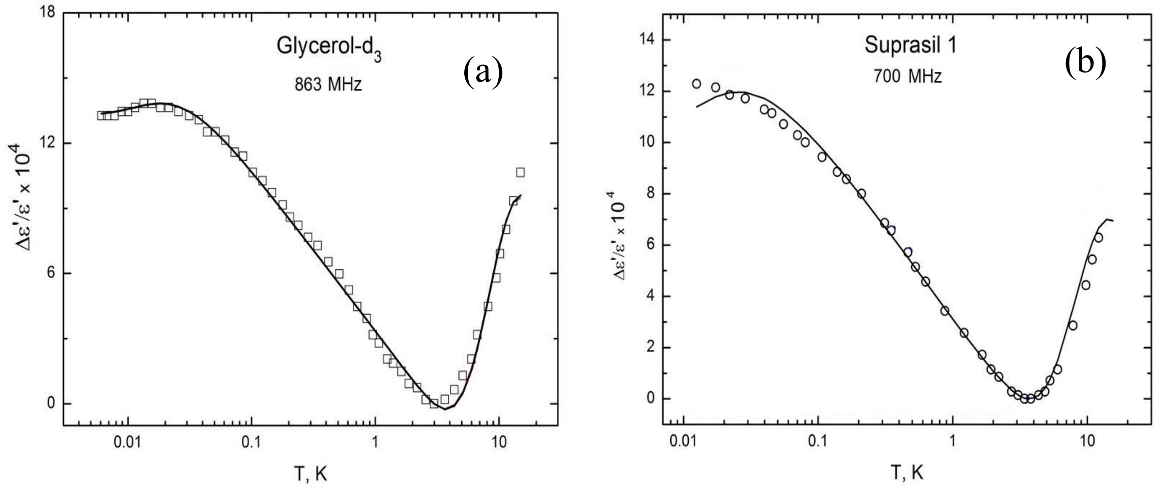

Fig. 9.8 – V-shaped dielectric constant temperature-dependence for the high frequency data of: a) amorphous Glycerol-d$_3$ (0.863 GHz), and b) Suprasil-I (0.7 GHz) [9.3]. The curves are the best fits from our theory (Chapter 4). The full ω-dependent formula for the 2LS RES contribution has been used in the fits.

Table 9.3 – Extracted parameters for the high-frequency (0.863 and 0.7 GHz) dielectric constant fits from the ATS theory (Chapter 4)

Glass type	A_{2LS} 10^{-4}	Δ_{0min} mK	γ 10^{-7} sK^3	A_{ATS} 10^{-2}	D_{min} K	Γ 10^{-5} sK^5
Glycerol-d$_3$	4.879	10.90	5.622	1.857	18.909	50.0
Suprasil-I	4.840	9.90	5.622	1.289	19.967	1.18

We have no explanation for such unrealistic, huge value of D_{min}, except that (Chapter 10) the number of coherently tunneling ions (most probably D$^+$ in Glycerol-d$_3$) may be large and/or that the electric-field intensity (unknown for the glycerol experiments) may also be huge (thus renormalizing the value of D_{min} upwards). This is confirmed by our best fit of similar data in Fig. 9.8 (b) for Suprasil-I at high frequency (0.7 GHz) [9.3] which allows us to extract the parameters in Table 9.3, the value of D_{min} being far bigger than the one extracted from experiments at low frequency (kHz range, Chapter 4) for the same glass.

The lack of reliable experimental dielectric data for amorphous glycerol makes the fitting of the polarization-echo data frustrating. All the more so, when considering that - so far - no evidence for a magnetocapacitance effect in a-glycerol has been found (albeit at the nominal frequency of 0.986 GHz) [9.3]. This last fact, however, could be explained by the suspected large value of D_{min}, for the order of magnitude of the magnetocapacitance is given, in our theory, by the combination $\pi P^* \overline{p_1^2} x_{ATS} / (2\varepsilon_0 \varepsilon_r D_{min})$ (Chapter 7) and for a-glycerol $\varepsilon_r = 42.5$ and D_{min} are much larger than for the multi-silicates. Low-frequency (kHz range) and weak electric-field intensity measurements of the dielectric constant of a-glycerol would be most useful. These lacking, we must limit our discussion of the magnetic dipole echo phenomena in a-glycerol to the qualitative level of understanding.

The integrated echo amplitude is readily obtained from Eq. (9.30), after the averaging procedure as in Eq. (9.32) and a subtraction of the pump-frequency mode ω are carried out:

$$\begin{aligned} \Delta IEA(\phi) \cong & -A_0 \frac{d}{\varepsilon_0 \varepsilon_r} x_{ATS} \frac{4\pi\hbar^2 P^*}{\mathrm{F}_0} \\ & \times \left\{ \int_{E_{c_1}}^{E_{c_2}} \frac{dE}{E} \int_{D_{min}}^{D_2(\phi)} \frac{dD}{D} \tanh\left(\frac{E}{2k_B T}\right) \frac{E^2}{E^2 - D^2} \Omega_R^2 \sigma(E) \frac{2w}{w^2 + (\omega_0 - \omega)^2} \right. \\ & \times [S(\theta_1, \theta_2) \cos(2(\omega_0 - \omega)\tau_{12}) + C(\theta_1, \theta_2) \sin(2(\omega_0 - \omega)\tau_{12})] + \\ & \left. + \int_{E_{c_2}}^{\infty} \frac{dE}{E} \int_{D_1(\phi)}^{D_2(\phi)} \frac{dD}{D} \;(\ldots \text{same integrand as above} \ldots) \right\} \end{aligned} \tag{9.37}$$

with $\sigma(E)$, w, S and C as in Eqs. (9.34, 9.35) above. We are now in the presence of an even narrower spectral delimiter than $\sigma(E)$:

$$\chi(E) = \frac{w}{\pi\hbar(w^2 + (\omega_0 - \omega)^2)} \tag{9.38}$$

is a (normalized) very sharply-peaked function of $E = \hbar\omega_0$ since $w \ll \Omega_R \ll \omega$. We can then take the limit $p_1 F_0 \to \infty$ that seems to be appropriate for the glycerol experiments and replace $\sigma(E)$ by a constant, $\sigma(E) \to (2\hbar\Omega_R)^{-1}$, to get:

$$\begin{aligned} \Delta IEA(\phi) \approx & -A_0 \frac{d}{\varepsilon_0 \varepsilon_r} x_{ATS} \frac{2\pi^2\hbar^2 P^*}{\mathrm{F}_0} \\ & \times \left\{ \int_{E_{c_1}}^{E_{c_2}} \frac{dE}{E} \int_{D_{min}}^{D_2(\phi)} \frac{dD}{D} \tanh\left(\frac{E}{2k_B T}\right) \frac{E^2}{E^2 - D^2} \Omega_R \chi(E)\, S(\theta_1, \theta_2) \cos(2(\omega_0 - \omega)\tau_{12}) \right. \\ & \left. + \int_{E_{c_2}}^{\infty} \frac{dE}{E} \int_{D_1(\phi)}^{D_2(\phi)} \frac{dD}{D} \;(\ldots \text{same integrand as above} \ldots) \right\} \end{aligned} \tag{9.39}$$

For fixed and large τ_{12} the above is essentially the energy convolution of a function very much like the DOS $g_{ATS}(E)$ times some slowly-varying functions of E and the sharply-peaked spectral delimiter $\chi(E)$. The result of this convolution is depicted in Fig. 9.9 and very much depends on whether $D_{min} < \hbar\omega$ or $D_{min} > \hbar\omega$.

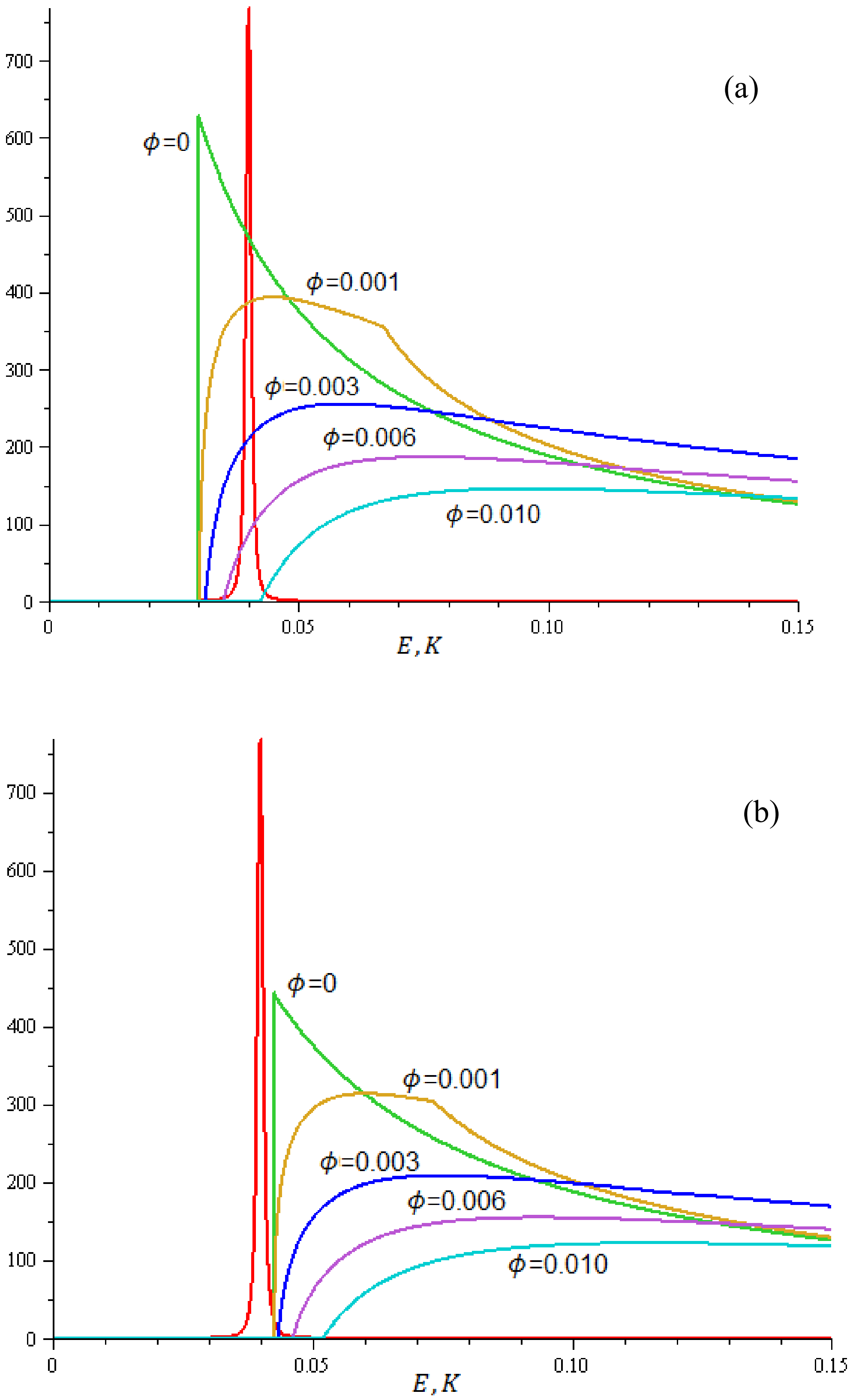

Fig. 9.9 – Convolution of the DOS $g_{ATS}(E, \phi)$ and the spectral delimiter $\chi(E)$ in the integral giving the IEA. a) If $D_{min} < \hbar\omega$ there is a significant effect on the echo amplitude as ϕ increases; b) In the opposite case $D_{min} > \hbar\omega$ the effect is much reduced and vanishes in the strict resonant case. This is our qualitative explanation for the "isotope effect".

In the first case, the evolution of the $g_{ATS}(E)$ with ϕ (or B) gives rise to a sizable magnetic effect on the echo amplitude (or IEA) even in the strict-resonant limit, whilst in the second case, $D_{min} > \hbar\omega$, the magnetic effect is drastically reduced and even vanishes in the strict resonant limit, $\chi(E) \to \delta(E - \hbar\omega)$.

This is the explanation for the so-called isotope effect in amorphous glycerol, which actually is a mere mass-substitution effect. Indeed, we claim that for natural glycerol the situation $D_{min} > \hbar\omega$ applies and that for the deuterated samples, as for the multi-silicates, $D_{min} < \hbar\omega$ applies. Indeed, D_{min} is roughly given by (Chapter 2, Eq. (2.4)):

$$D_{min} \approx \frac{1}{2}\hbar\sqrt{\frac{k}{M}} \qquad \text{moreover:} \quad D_0 \approx \hbar\sqrt{\frac{k}{M}}\, e^{-\frac{d}{\hbar}\sqrt{2MV_B}} \tag{9.40}$$

where k is the bonding constant that depends only on the chemistry and not on the isotope's mass, M. Thus we immediately see that $D_{min}(\text{deuterium}) = D_{min}(\text{hydrogen})/\sqrt{2}$ and this is sufficient to make the transition from case b) to case a) in Fig. 9.9 when a substantial mass change of the tunneling particles through isotopic substitution is made.The case of partial isotopic substitution requires separate considerations. A further consequence of mass substitution, as seen in Eq. (9.40) is that a larger mass M will make - the chemistry being unchanged - the parameters $D_{0min,max}$ much smaller and thus will give rise to a much slower variation of the echo's amplitude with B, as is indeed verified in the experiments (Fig. 9.3). The highly non-uniform shape of the DOS for the ATS model thus qualitatively (and for the multi-silicates also quantitatively) explains all of the experimental findings.

The last topic we discuss is our explanation for the dramatic effect for the echo's IEA dependence on the waiting time τ_{12} near $B = 0$. To explain this we take the $B \to 0$ limit of Eq. (9.39), when only the second term contributes and we get, evaluating the D-integral exactly and lumping all slowly-varying functions into an overall constant $\mathcal{A}^*$:

$$\lim \mathit{\Delta IEA}(\phi) \approx -\mathcal{A}^* \int_{D_{min}}^{\infty} \frac{dE}{E}\tanh\left(\frac{E}{2k_BT}\right)\ln\left(\left(\frac{D_{0max}}{D_{0min}}\right)^2 \frac{E^2 - D_{0min}^2\phi^2}{E^2 - D_{0max}^2\phi^2}\right) \times \chi(E)\cos(2(\omega_0 - \omega)\tau_{12}) \tag{9.41}$$

Inspection of this last expression shows, that the ATS contribution quadratically decreases as the AB phase (or magnetic field) increases; hence, the disappearance of the oscillations in τ_{12} is slow (as experimentally reported [9.2]) for very weak but increasing B. To understand the oscillations (and their absence) we set $B = 0$ and redefining the overall constant we arrive at (since τ_ϕ is the shortest decay time involved):

$$\lim \Delta IEA(0) \approx -\mathcal{B}^* \int_{D_{min}}^{\infty} \frac{dE}{E} \frac{\tau_{\phi}^{-1}}{\pi\hbar[\tau_{\phi}^{-2}+(\omega_0-\omega)^2]}\cos(2(\omega_0-\omega)\tau_{12}) \tag{9.42}$$

The remaining integral can be rewritten as an integral in the interval $[0,\infty]$, which yields an exponentially decaying contribution in τ_{12}, plus the integral in the energy interval $[0,\hbar\omega - D_{min}]$. The latter is responsible for the oscillations in τ_{12} since:

$$\int_0^b dx \frac{\cos x}{x^2+a^2} = \frac{\pi}{2a}e^{-a} + \mathrm{Im}\left\{\frac{e^{-a}}{2a}\mathrm{Ei}\,(-a+ib) - \frac{e^{a}}{2a}\mathrm{Ei}\,(a+ib)\right\} \tag{9.43}$$

where $\mathrm{Ei}(z)$ denotes the exponential-integral function [9.14]. Rearranging Eq. (9.42), also adding the 2LS standard exponentially decaying contribution [9.1, 9.11], we come to the following functional form for the total IEA of the sample:

$$\lim IEA(0) \approx C_{2LS}e^{-\frac{2\tau_{12}}{\tau_{\phi(2)}}} + C_{ATS}\frac{\tau_{\phi(3)}}{\tau_{12}}e^{-\frac{2\tau_{12}}{\tau_{\phi(3)}}}$$

$$+ K_{ATS}\mathrm{Im}\left\{\frac{e^{-a}}{2a}\mathrm{Ei}\,(-a+ib) - \frac{e^{a}}{2a}\mathrm{Ei}\,(a+ib)\right\} \tag{9.44}$$

where C_{2LS}, C_{ATS} and K_{ATS} are appropriate constants and where:

$$a = 2\tau_{12}\tau_{\phi(3)}^{-1} \qquad b = 2\tau_{12}\left(\omega - \frac{D_{min}}{\hbar}\right) \tag{9.45}$$

We plot expression (9.44) in Fig. 9.10 as a function of τ_{12}, assuming some reasonable value of $\tau_{\phi(3)} = 1.0$ µs for the ATS spectral-diffusion time, $\tau_{\phi(2)}$=10.0 µs for the 2LS one, and of $\Delta\omega = \omega - \frac{D_{min}}{\hbar} = 0.6$ MHz for the frequency offset.

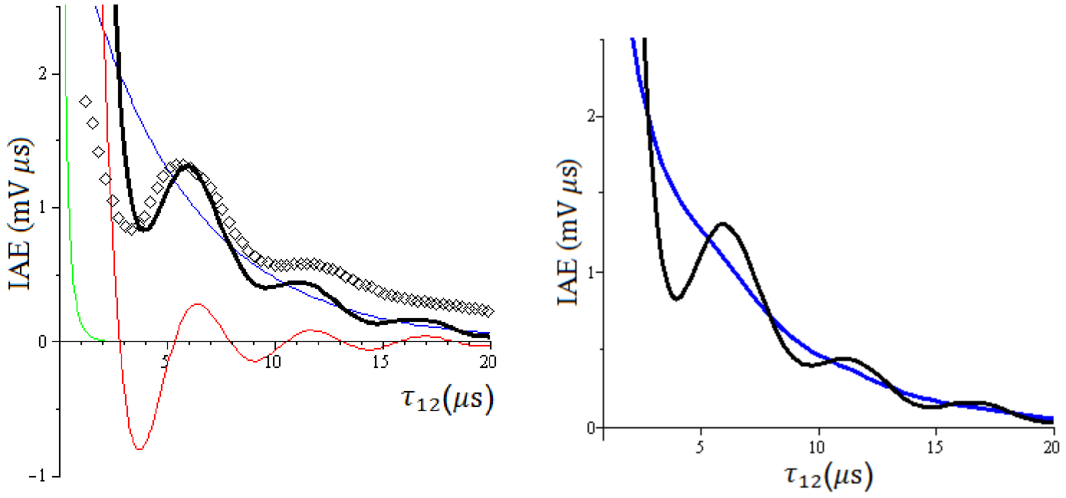

Fig. 9.10 – The IEA from Eq. (9.44) plotted as a function of τ_{12} for parameters as in the text. a) The simplified theory almost reproduces (black curve) the experimental data (diamonds) for Glycerol-d₃ at $B = 0$, nominal frequency $\omega/2\pi$ =0.887 GHz and T =13.5 mK [9.3] (blue curve: – 2LS contribution, green and red curves: – ATS contributions, black curve: – sum of 2LS and ATS contributions); b) Disappearance of the IAE oscillations when $\tau_{\phi(3)}$ decreases or $\Delta\omega$ increases (blue curve).

As is shown in Fig. 9.10 (a) (black curve), this simplified theoretical treatment almost reproduces the data for Glycerol-d$_3$ at $B = 0$ [9.3]. Fig. 9.10 (b) also shows (blue curve) that reducing to $\tau_{\phi(3)} = 0.3$ μs causes the oscillations to disappear; alternatively, this can be achieved by increasing $\Delta\omega$.

This explains the findings in Fig. 9.7. Leaving the sample in the air causes a change in D_{min} simply because more micro-crystals are generated (larger $\Delta\omega$), but also because of mass substitution through dissociation. The subtle role of the true value of the resonating frequency ω is as yet not completely understood.

Clearly, if $\Delta\omega < 0$ (case of Glycerol-d$_0$) there can only be exponential decay (from the 2LS contribution), but if $\Delta\omega > 0$ is also too large the oscillations die out. We believe this is the case for the multi-silicates.

Qualitatively at least, our ATS model explains all experimental observations so far.

Chapter 10

Interpretation of the fitting parameters: size of the tunneling cluster

The tunneling model is a phenomenological model, it makes use of the concept of tunneling systems (TS) within one modeling approach (2LS STM) or another (ATS), but with little knowledge of the TS's true nature. We claim here that thanks to the remarkable experiments in a magnetic field by the Berlin-Heidelberg and Saclay groups, for the first time some clear indication about the nature of the TS is indirectly emerging.

One cannot avoid noticing that, in comparison with the parameters for the 2LS STM (Chapter 2), those for the curve-fitting of our theory based on the multi-welled ATS appear to be rather large. Namely:

- D_{min} ranges from 16 to 870 mK;
- $D_{0min,max}$, multiplied by the quantity $\left|\frac{q}{e}\right| S_{\Delta}$, range from 0.8×10^2 to 4.5×10^5 KÅ^2;
- these values appear to be systematically larger for those experiments carried out at the higher temperatures;

moreover:

- $x_{ATS}\, P^*$ ranges from to 6 to 7×10^{16} g^{-1};
- p_1 ranges from 0.05 to 0.41 D; from the echo experiments (Table 9.1) for the nominal value $F_0 \approx 1.0$ kV/m of the electric field intensity one would infer values ranging from 0.46 to 0.98 D.

Our interpretation for the large values of D_{min} and especially of $D_0 \left|\frac{q}{e}\right| S_{\Delta}$, and at the same time for the small values of p_1 (on should consider that the elementary electric dipole is $ea_B = 2.54$ D) is as follows. The "tunneling particle" in question is only a fictitious one, representing the coherent tunneling of a cluster of *N* true particles (which might be the lighter ones involved in the material (O^{--} in the multi-silicates and H$^+$ and/or D$^+$ in a-glycerol)) of which we have made up appropriate renormalized tunneling parameters. The concept of coherent tunneling (CT) in separate local potentials is distinct from that of the joint tunneling of *N* particles in the same local potential, for in the latter case the tunneling probability would be depressed exponentially: $D_0 \approx {\Delta_0}^{N/2}$ (Δ_0 being the real particle's tunneling transparency). As we shall show below, at least for moderate values of *N*, for CT we expect:

$$D_0 \approx N\mathit{\Delta}_0 \qquad D_{min} \approx N\mathit{\Delta}_{min} \tag{10.1}$$

and, for the fictitious particle's charge and flux-threaded area:

$$q = Nq_0 \qquad S_{\mathit{\Delta}} \approx 4Na_B^2 \tag{10.2}$$

($q_0 \approx e$ being the charge of the real tunneling particle, a_B Bohr's radius). In the latter relations, less obvious is the renormalization of the flux-threaded area $S_{\mathit{\Delta}}$. It is however the direct consequence of our multi-phase model of real glass, thought of as made up of regions of enhanced atomic ordering (RER) (Fig. 4.2). The magnetic flux appears quadratically in our theory, each elementary flux adding up within each micro-crystal or RER and then appearing multiplied by $\cos^2\beta$ in the glassy matrix in a magnetic field, a factor averaging out to ½ in the bulk. From these considerations, the renormalization of *D₀* and $D_0\left|\frac{q}{e}\right|S_{\mathit{\Delta}}$ would be as follows:

$$D_{min} \approx N\Delta_{min} \qquad D_0\left|\frac{q}{e}\right|S_{\mathit{\Delta}} \approx 8N^3\Delta_0 a_B^2 \tag{10.3}$$

Setting $\Delta_0 = 1$ mK, one gets a value of *N* ranging from about 25 coherent-tunneling particles in a cluster at the lowest temperatures, to about 600 at the higher temperatures. These estimates are somewhat speculative, since the real values of the elementary flux-threaded area and of the elementary tunneling barrier transparency Δ_0 are unknown, we are however inclined to support the value $N \approx 200$ that was proposed by Lubchenko and Wolynes [10.1]. This would yield a value of Δ_{min} ranging from 80 μK to 4 mK.

The above considerations, however, show the tendency for the CT cluster size *N* to be also temperature dependent, much smaller at the lowest temperatures than at the higher ones. In our opinion this is a most interesting and reasonable finding. The idea of a large CT size *N* is however the most obvious interpretation for the small values of the electric dipole moment p_1 of the fictitious tunneling particle. Since electric dipole moments add up vectorially in the CT cluster:

$$\mathbf{p}_1 = \sum_{i=1}^{N} \mathbf{p}_i \tag{10.4}$$

it appears natural to us that the magnitude $\mathrm{p}_1 = |\boldsymbol{p}_1|$ should be smaller (even much smaller, for large *N*) than the value of the elementary dipole, ea_B (see Fig. 10.1).

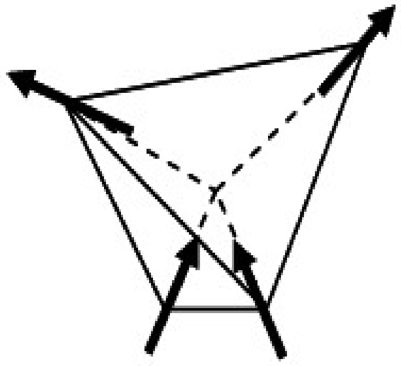

Fig. 10.1 – The electric dipole moments of the individual tunneling particles add up vectorially, resulting in an effective moment much smaller than the atomic ea_B.

We now come to the justification of Eqs. (10.1). At low temperatures the interactions between true tunneling particles become important and coherent tunneling motion can take place. Coherent motion in the context of the tunneling model is a state in which all of the particles in each local potential contribute to the overall tunneling process coherently. We exemplify our ideas in the context of the simpler 2LS situation ($n_w = 2$) first.

Let us consider two interacting 2LS's. The positions of the particles in the wells we call left (L) and right (R). The tunneling particles interact via a weak potential U which may, for example, appear from either a strain-strain interaction having the form $U \sim a/r^{-3}$ (dipole-dipole interaction) [10.2, 10.3], where r is the distance between the tunneling particles either in the L or R wells, a being a constant, or it could be due to electrostatic dipole-dipole interaction. The tunneling of the particle in one 2LS from L to R (or vice versa) influences, via the interaction, the particle from the other 2LS, forcing it to jump into the free well. The Hamiltonian of two interacting 2LS can be written as follow ($\Delta_{iL} = -\Delta_{iR} = \Delta_i,\ i = 1{,}2$):

$$H_2 = \Delta_{01} \sum c_{1a}^{\dagger} c_{1a'} + hc + \sum \Delta_{1a} c_{1a}^{\dagger} c_{1a} + \Delta_{02} \sum c_{2a}^{\dagger} c_{2a'} + hc + \sum \Delta_{2a} c_{2a}^{\dagger} c_{2a} - U\left(c_{1L}^{\dagger} c_{1L} c_{2L}^{\dagger} c_{2L} + c_{1R}^{\dagger} c_{1R} c_{2R}^{\dagger} c_{2R}\right) \quad (10.5)$$

which acts on the joint states $|aa'\rangle = \{|LL\rangle, |LR\rangle, |RL\rangle, |RR\rangle\}$. The coherent motion of the real particles can now be replaced by the tunneling of a new, fictitious particle in its own double well. In order to write the Hamiltonian of coherent tunneling particles we are interested only in matrix elements $\langle LL|H|LL\rangle$, $\langle RR|H|RR\rangle$, $\langle LR|H|RL\rangle$, $\langle RL|H|LR\rangle$ of the Hamiltonian (10.5):

$$\begin{aligned} \langle LL|H|LL\rangle &= \Delta_1 + \Delta_2 - U \\ \langle RR|H|RR\rangle &= -\Delta_1 - \Delta_2 - U \qquad (10.6) \\ \langle LR|H|RL\rangle &= \langle RL|H|LR\rangle = \Delta_{01} + \Delta_{02} \end{aligned}$$

These matrix elements represent the Hamiltonian of the fictitious particle, which corresponds to both particles moving together coherently:

$$H_1' = \begin{pmatrix} \Delta_1 + \Delta_2 - U & \Delta_{01} + \Delta_{02} \\ \Delta_{01} + \Delta_{02} & -\Delta_1 - \Delta_2 - U \end{pmatrix} \tag{10.7}$$

Next, we consider the case of three interacting 2LS's and repeat the previous operation. The Hamiltonian of three interacting 2LS has the form:

$$H_3 = \sum_{i=1}^{3} \left\{ \sum_{a,a'=L}^{R} \left(\Delta_{0a} c_{ia}^{\dagger} c_{ia'} + hc\right) + \sum_{a=L}^{R} \Delta_{ia} c_{ia}^{\dagger} c_{ia} \right\} - U \sum_{i,i'} \sum_{a} c_{ia}^{\dagger} c_{ia} c_{i'a}^{\dagger} c_{i'a} \tag{10.8}$$

The matrix elements that correspond to coherent tunneling are obtained as follows:

$$\begin{aligned} &\langle LLL|H|LLL\rangle = \Delta_1 + \Delta_2 + \Delta_3 - 3U \\ &\langle RRR|H|RRR\rangle \\ &\qquad = -\Delta_1 - \Delta_2 - \Delta_3 - 3U \\ &\langle LR|H|RL\rangle = \langle RL|H|LR\rangle = \Delta_{01} + \Delta_{02} + \Delta_{03} \end{aligned} \tag{10.9}$$

One can notice that the tunneling parameter is the sum of the Δ_{0i} of each 2LS. The energy asymmetry is also the arithmetical sum of the Δ_i of each 2LS, but one must subtract the interaction energy multiplied by $N(N-1)/2$. Thus, for a system of N 2LSs we find that the diagonal matrix element becomes $\Delta = \left(\sum_{i=1}^{N} \Delta_i\right) - \frac{N(N-1)}{2} U$ and the off-diagonal element, that corresponds to the coherent tunneling splitting for all three particles, becomes $\Delta_0 = \sum_{i=1}^{N} \Delta_{0i}$.

Applying the previous considerations to our model for a number N of ATS with three wells (see Fig. 10.2) we can write the interacting Hamiltonian in the form:

$$H_N = \sum_{i=1}^{N} \left\{ \sum_{a,a'=1}^{3} \left(D_{0a} c_{ia}^{\dagger} c_{ia'} + hc\right) + \sum_{a=1}^{3} E_{ia} c_{ia}^{\dagger} c_{ia} \right\} - U \sum_{i,i'} \sum_{a} c_{ia}^{\dagger} c_{ia} c_{i'a}^{\dagger} c_{i'a} \tag{10.10}$$

If we represent the group of N coherently-tunneling particles as a single fictitious particle moving in a 3-welled potential, which is characterized by its own ground state energies E_A and tunneling parameter D_0, we can describe this 3LS by the following Hamiltonian:

$$H_1' = \sum_{A} E_A c_A^{\dagger} c_A + \sum_{A,A'} \left(D_0 c_A^{\dagger} c_{A'} + hc\right), \quad A = 1,2,3 \tag{10.11}$$

The ground states energies E_A in the wells and tunneling parameter D_0 for the fictitious particle, in line with the calculations above, can be obtained as:

$$\begin{aligned} E_A &= \textstyle\prod_i \langle ia|H|ia\rangle \qquad A = a = 1,2,3 \\ D_0 &= \textstyle\prod_i \langle ia|H|ib\rangle\text{'} \qquad a \neq b, \;\; i = 1,2,..,N \end{aligned} \tag{10.12}$$

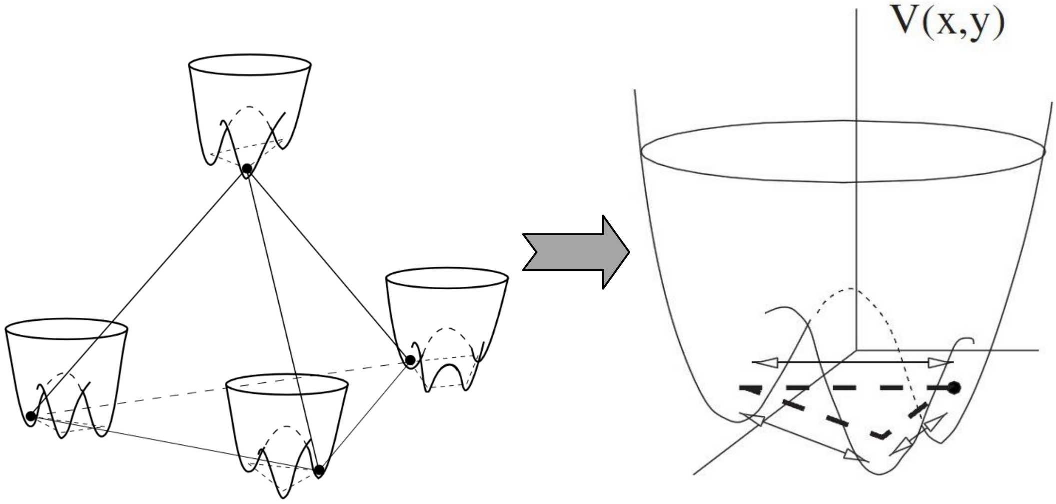

Figure 10.2 – A cluster of four interacting (real) tunneling particles being replaced with a (fictitious) single 3LS having renormalized parameters.

In analogy with the 2LS considerations one can see that the tunneling parameters D and especially D_0 become roughly the arithmetical sums of those of the bare coherently tunneling particles, $D \approx ND_i$ (neglecting the correction for sufficiently weak U) and $D_0 = ND_{0i}$, respectively. Therefore, since N can attain values as large as 200 [10.3] (independently of the solid’s composition) in some models, this leads to values of D_i and D_{0i} comparable to those characteristic of the 2LS TM.

Chapter 11

Conclusions and outlook

In the present work a new (*anomalous*) tunneling model has been re-proposed and applied, as an extension of the standard tunneling model to explain the anomalous dielectric properties exhibited by multi-component dielectric glasses at low and very low temperatures. Instead of the standard single-coordinate double-welled (W-shaped) potential, which describes the ordinary 2LS TS inherent to the a-SiO$_2$ network, the existence of anomalous tunneling systems (ATS) was assumed and justified in the glasses, where the particle (actually, the fictitious particle) of charge q moves in an n_w-welled 3D potential, tunneling through a relatively shallow energy barrier. ATS in the glasses are provided by the process of partial devitrification of the glassy network due to the presence of network-modifying ions in real glasses. The new probability distribution, which is now, in contrast to the constant one of the STM, inversely proportional to the energy gap, takes into account the said partial devitrification. The hopping Hamiltonian for a single, non interacting ATS with three wells as the simplest case was introduced and its eigenvalues were determined.

We have shown that there is direct evidence for the multi-welled ATS in zero magnetic field already. The new multi-welled ATS together with STM's 2LS explain qualitatively as well as quantitatively and with reasonable parameters the relative change of the dielectric permittivity at zero magnetic field for multi-component glasses such as AlBaSiO and BK7. It explains also the relative change of the dielectric permittivity and heat capacity with temperature and with variation of the alkali concentration x in the mixed $(\mathrm{SiO_2})_{1-x}\,(\mathrm{K_2O})_x$ glass. Our work predicts that the magnetic response of the alkali-silicate glasses should be important and scale like the molar alkali concentration x. At the same time the $-1 : 1$ slope ratio problem of the standard TM (which predicts a -2 : 1 ratio) has been given a simple explanation in terms of our two-component (2LS + ATS) tunneling model.

In order to explain the effects of the magnetic field we consider the motion of the fictitious charged particle in a 3-welled potential, coupling to the magnetic field through the particle's orbital motion. The magnetic-field dependent Hamiltonian of a single ATS has been modified introducing the Aharonov-Bohm phase. The energy eigenvalues are found to be periodic in the magnetic flux.

Keeping the same parameters probability distribution for $B = 0$ and using the new magnetic-field dependent Hamiltonian we are able to explain very well the experimentally observed relative change of the permittivity for the AlBaSiO, BK7, Duran and $SiO_{2+x}C_yH_z$ glasses and the relative change of the dielectric loss for AlBaSiO with almost the same material parameters. The higher-order approximation can qualitatively explain also the further increase of the dielectric constant and loss at higher magnetic field, as observed in some of the experiments.

The formulation of Gurevich et al. for the echo signal from a collection of 2LS was obtained and verified using the density matrix formalism and also (more rigorously) from a Schrödinger-equation treatment in which high-frequency modes are neglected and phonon-damping is treated in a phenomenological way. The polarization echo's theory was extended to the case of the ATS model describing glasses in a magnetic field; the point of view has been taken that a background of ordinary 2LS's - insensitive to the magnetic field - also exists in the glass. The agreement between theory and experiment is highly satisfactory, given the simplifications used in the theory. The ATS approach also predicts a linear in B intermediate decay regime for the echo amplitude, and this is often experimentally observed. The isotope-substitution effect in the dipole-echo amplitude also can be explained in a simple way with our model. Most pleasing was the semi-quantitative recovery of the damped oscillating behaviour of the integrated echo amplitude as a function of the pulse separation time, as observed for deuterated amorphous glycerol, but not for the other studied materials. We have been able to explain all these different observations, always making use of the same model in every detail.

The interpretation of the extracted material parameters brings us to confirm the existence of coherent tunneling of a cluster of N true particles, with a value of N ranging from about 25 coherent-tunneling particles in a cluster at the lowest temperatures, to about 600 at the higher temperatures. The above considerations, however, show the tendency for the cluster size N to be also temperature dependent, much smaller at the lowest temperatures than at the higher ones. In our opinion this is a most interesting and reasonable finding. The idea of a large cluster size N is ultimately the most obvious interpretation for the extracted small values of the electric dipole moment p_1 of the fictitious tunneling particle, that is the vector sum of all dipole moments of the particles in the cluster.

No one of the published theories, proposed earlier to describe the magnetic field effect in glasses at very low temperatures, could explain all of the experimentally observed effects in glasses at the same time. Our new (*anomalous*) tunneling model is the simplest extension of the standard tunneling model that can explain them all, including also the zero magnetic field composition-dependent behaviour at low temperatures which entails a fractal picture for the glass structure.

Our model opens the way for the microscopic understanding of the nature of the tunneling systems in real glasses and more experiments and computer simulations should be carried out to verify our model. For example in some multi-phase materials like ceramic glasses in which a degree of partial devitrification takes place and where micro-crystals embedded within an amorphous glassy matrix are known to occur.

A key experiment which would help in deciding upon the validity of the nuclear quadrupole approach would be as follows. The glass of chemical composition $(SiO_2)_{1-x}(MgO)_x$ should be investigated in a magnetic field and for variable, controlled molar concentrations x. This is also a ceramic glass and in our ATS approach the magnetic field response, for all experiments, would scale like x independently of the deployed magnesium isotope's nature. Conversely, according to the nuclear quadrupole approach there should be no magnetic response at all if the naturally occurring isotopes ^{24}Mg (abundance 79%, nuclear spin 0, NEQM Q=0) and ^{26}Mg (11%, nuclear spin 0, NEQM Q=0) are employed, whilst the response would scale like x only in the case in which ^{25}Mg (10%, nuclear spin 5/2, NEQM Q=199.4 m barn) is employed. The naturally-occurring Mg isotopes are used widely in nuclear medicine and are commercially available. This experiment, in our view, is feasible and decisive.

Finally, the interactions between the ATS should also be taken into account for very low temperatures, when the interactions become important, to provide a more complete interpretation of the low-temperature observed behaviour. The same should be said for the development of a theory that goes beyond the linear-response approximation. The high magnetic field dependence can be also described by means of higher-order approximations and a full multi-level approach in the calculations.

Addendum[4.23]: A spin-glass phase transition at 6 mK

So far all our theoretical modeling has involved mostly single-particle physics, although the single particle is fictitious and as we claim it represents in practice a cluster of N coherent-tunneling particles, with N large yet neither mesoscopic nor macroscopic. However, some of the earlier findings of the Berlin-Heidelberg group [4.11] hinted at the presence of collective phenomena in the multi-silicate glasses at the lowest temperatures explored. As shown in Fig. 11.1, the dielectric constant (thought of as electric field susceptibility) of AlBaSiO shows a kink in its temperature dependence in zero magnetic field and at around 6 mK. The purpose of this addendum is to convince the reader that also this mysterious phenomenon – in our opinion a genuine sping-glass transition – can be understood on the basis of the multi-welled ATS model.

One begins by evaluating the electric dipole moment of the generic ATS by adding a vanishing electric field $\mathbf{F}_0$ contribution to each single-well energy: $E_i \rightarrow E_i - \mathbf{F}_0 \cdot \mathbf{p}_i$ (alternatively a strain field and strain tensor can be invoked). Using the expressions for the 3-welled TS energies, Eq. (6.4), after some work one gets for the dipole of state $|a>, a = 0,1,2$:

$$\mathbf{d}_a = \sum_{i=1}^{3} \mathbf{d}_a^{(i)}$$

$$\mathbf{d}_a^{(i)} = \mathbf{p}_i \frac{2}{9} \frac{1}{\sqrt{1 - \frac{\sum_{i \neq j} E_i E_j}{6D_0^2}}} \left[\frac{E_i}{D_0} \cos\left(\frac{1}{3}\theta + \theta_a\right) + \frac{\operatorname{cotan}\theta}{D_0^2 \left(\cos\phi + \frac{E_1 E_2 E_3}{2D_0^3}\right)} E_j E_k (D_0^2 - \frac{1}{3} E_j E_k - \frac{1}{6} E_i^2) \sin\left(\frac{1}{3}\theta + \theta_a\right) \right] \qquad (11.1)$$

with the notation of Chapter 6 and where (i, j, k) is a cyclic permutation of (1,2,3). The dipole of state $|a>$ is thus made up of three dipoles directed along the well's directions.

One can then study (numerically) the behaviour of these dipoles in the relevant limits $D \equiv \sqrt{E_1^2 + E_2^2 + E_3^2} \ll D_0$ and $\phi \rightarrow 0$ to find:

- only d_0 and d_1 change significantly with ϕ, whilst d_2 remains small and virtually constant;
- the dipole $\mathbf{d}_0$ is to a very good approximation always opposite to $\mathbf{d}_1$, so much so that one can write

$$\mathbf{d}_a \cong \mathbf{d}(\phi) s_a \qquad (11.2)$$

where $s_a = \pm 1$ is an Ising variable for the two lowest-lying states $a = 0,1$.

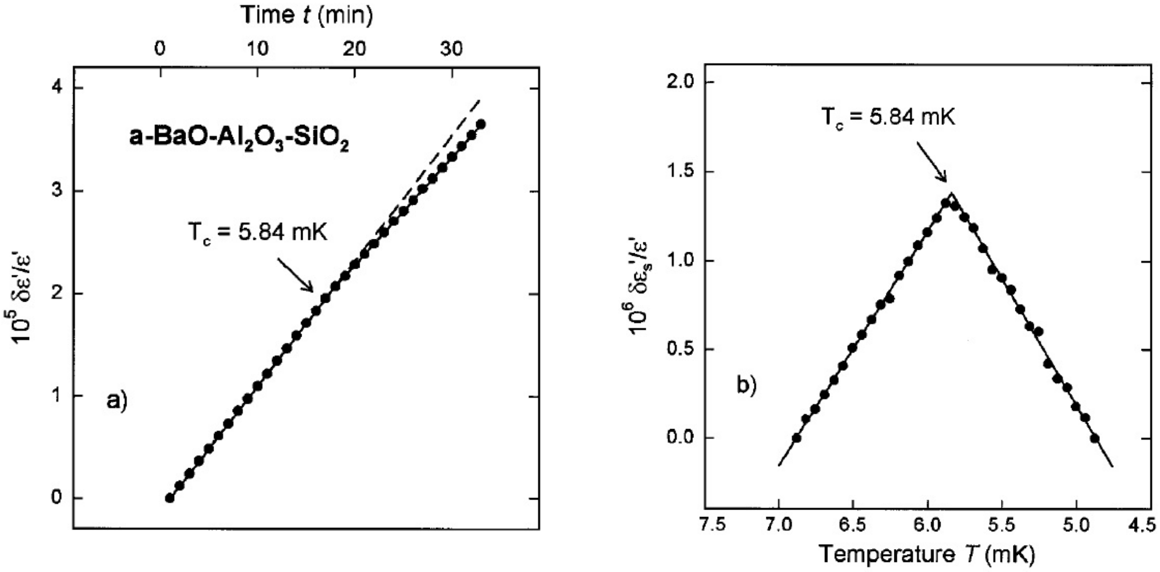

Fig. 11.1 – (a) Dielectric constant variation of the AlBaSiO glass measured at a constant cooling rate of 62.6 μK/min. The dashed line is the extrapolation of the data from higher temperature. (b) Same data after subtracting a straight line through the first and last points of the measurement. On the abscissa the time scale has been converted to temperature. The magnetic field was $B = 0$. From Ref. [4.11].

Thus, each ATS (regardless of the actual number of wells, in fact) A can be considered as the site of a "spin" $\mathbf{d}_A$ having random single-axis anisotropy as well as a random energy-gap $\Delta\mathcal{E} \cong \sqrt{D_0^2\phi^2 + D^2}$ for the flipping of the local spin direction. At this point, switching on the electric field again, one can write the following Hamiltonian representing the energy of the collection of (quasi-classical) "spins" distributed in the glass and coupled via a weak dipole-dipole interaction:

$$H_{ATS} = \sum_{\{A\neq B=1\}}^{N_{ATS}} \frac{\mathbf{d}_A \cdot \mathbf{d}_B - 3(\mathbf{d}_A \cdot \hat{\mathbf{r}}_{AB})(\mathbf{d}_B \cdot \hat{\mathbf{r}}_{AB})}{r_{AB}^3} - \mathbf{F}_0 \cdot \sum_A \mathbf{d}_A - \frac{1}{2}\sum_A \Delta\mathcal{E}_A\, s_A \quad (11.3)$$

where A, B denote pairs of ATS. This intractable Hamiltonian can be simplified by resorting to a single-index Ising spin variable $s_A = \pm 1$ and writing

$$\begin{aligned}\mathbf{d}_A \cdot \mathbf{d}_B - 3(\mathbf{d}_A \cdot \hat{\mathbf{r}}_{AB})(\mathbf{d}_B \cdot \hat{\mathbf{r}}_{AB}) \\ = \mathrm{d}_A \mathrm{d}_B(\sin\Phi_{AB}^A \sin\Phi_{AB}^B - 2\cos\Phi_{AB}^A \cos\Phi_{AB}^B) s_A s_B \quad (11.4)\end{aligned}$$

Φ_{AB}^A being the angle between ATS dipole $\mathbf{d}_A$ with the direction joining ATS A and B. The trigonometric expression above is a random variable that takes values in [-2, +2] and therefore, neglecting the randomness of $\mathbf{d}_A$ we end up with:

$$H_{\text{spin}} = [d(\phi)]^2 \sum_{\{A \neq B=1\}}^{N_{ATS}} \frac{J_\Phi(A,B)}{r_{AB}^3} s_A s_B - \frac{1}{2} \sum_A \Delta\mathcal{E}_A \, s_A \qquad (11.5)$$

where $J_\Phi(A,B)$ is a random variable taking values in [-2,+2] with a probability distribution $P(J_\Phi)$ that may be evaluated numerically by assuming a uniform, or polarized (some glasses have an overall dipole moment), distribution of dipoles $\{\mathbf{d}_A\}$ in the sample (Fig. 11.2).

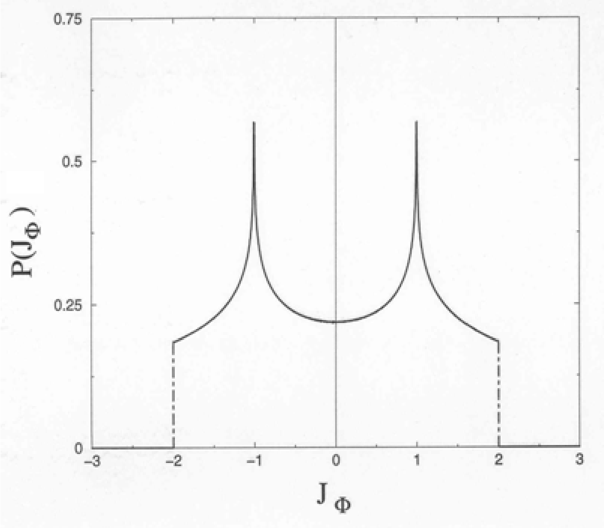

Fig. 11.2 – The (normalized) probability distribution for the coupling constant's sign J_Φ for uniform spatial dipole distribution; for a polarized spatial distribution, $P(J_\Phi)$ becomes skew.

It can be recognized immediately that the spin Hamiltonian (11.5) is that of a short-ranged (r^{-3}) Ising spin-glass system in a weak (random) positive external field, where $P(J_\Phi)$ can be replaced with a sum of Dirac's δ-functions centered in $J_\Phi/2 = -1,0,+1$. This dilute Ising spin-glass in three dimensions ought to display an Almeida-Thouless line in the (T,H) plane (where $\mathrm{H} = \overline{\Delta\mathcal{E}_A} > 0$ is a fictitious, averaged out "magnetic" field if we neglect the energy gap randomness in first approximation, its sign being always positive). The question being still controversial [11.1], this would however mean [11.2] that there is a genuine spin-glass transition at some temperature T_f (denoting perhaps just some dynamical freezing) which would come to depend on the real magnetic field B (through $d(\phi)$). Experiments like that in Fig. 11.1 have not, however, been repeated in an external magnetic field, where we predict the cusp to shift downwards in T_f with increasing B.

Acknowledgments

I would like to express my deep gratitude to my PhD Thesis supervisor, Professor Giancarlo Jug, for his proposition to work on this research, always interesting ideas, valuable recommendations, his openness and constant support during these three years of the work. I really enjoyed the time while working in this research.

I would like to thank MUIR for the generous support that I received through their scholarship “Progetto Giovani” to support my studies and life in Italy.

My gratitude to the Università degli Studi dell'Insubria for opening their doors to international researchers giving the opportunity to study here.

A special thank to Italy and Como City, for the hospitality and for the new friends from all over the world that I met here during these years.

I would like to thank to the Sumy State University and to Aleksander Olemskoi, the head of the Physical Electronics Department (now Department of Nanoelectronics) for the knowledge I have get there, to Volodymyr Yu. Storizhko from the Institute of Applied Physics, to Aleksandr St. Bakai and Alexander Borisenko from National Science Center KIPT.

A big thanks to my friend Maksym Riabokon, with whom we explored an italian cities, Alps, lakes and seas during holidays accompanied by fundamental conversations about life and science, and to my first roommate Matias Ubogui for his openness and friendship, that opened for me international community in Como.

I would also like to thank all my friends in Ukraine, especially to Lyulyov Oleksiy and Liliya and their small son Dima, for the unconditional support and friendship at a distance.

My huge special thanks to Mrs. Oksana Vil’kova for her support which gives me strength to work, who more than everyone has made this time special.

In the end, particular thanks are due to my family in Ukraine for the unconditional support and love: my parents Valentina and Valery, my brother Oleg, my grandmother Halya, and all other relatives.

Maksym Paliienko,
Italy, Como,
2008-2011.

REFERENCES

2.1 Zachariasen W. H., J. Am. Chem. Soc. **54**, 3841 (1932).

2.2 Shelby J. E., Introduction to Glass Science and Technology, 2-nd Edition, The Royal Society of Chemistry, Cambridge, UK, p.297 (2005).

2.3 Zeller R. C., Pohl R.O., Phys. Rev. B **4**, 2029 (1971).

2.4 Phillips W. A., J. Low. Temp. Phys. **7**, 351 (1972).

2.5 Anderson P. W., Halperin B. I., Varma C. M., Philos. Mag. **25**, 1 (1972).

2.6 Reinisch J. and Heuer A., Phys. Rev. Lett. **95**, 155502 (2005).

2.7 Reinisch J. and Heuer A., J. Phys. Chem. B **110**, 19044. (2006**).**

2.8 Hunklinger S., Arnold W., Stein S., Nava R., Dransfeld K., Phys. Lett. A **42**, 253 (1972).

2.9 Golding B., Graebner J. E., Halperin B. I., Schutz R. J., Phys. Rev. Lett. **30**, 223 (1976).

2.10 Stephens R. B., Phys. Rev. B **13**, 852 (1976).

2.11 M. von Schickfus, Hunklinger S., J. Phys. C **9**, L439 (1976).

2.12 Phillips W. A. (Editor), Amorphous Solids, Topics in Current Physics, Springer Verlag, p. 107, (1981).

2.13 Jackle J., Z. Physik, **257**, 212 (1972).

2.14 Bloch F., Phys. Rev. **70**, 460 (1946).

2.15 Carruzzo H., Grannan E. R. and Yu C. C., Phys. Rev. B **50**, 6685 (1994).

2.16 Hunklinger S., Arnold W. In: Thurston R. N. and Mason W. P. Editors, Physical Acoustics – Vol. **12**, p.155 (1976).

2.17 Wiegers S. A. J., Jochemsen R., Kranenburg C. C. and Frossati G., Rev. Sci. Instrum. **58**, 2274 (1987).

2.18 Rau S., Enss C. and Hunklinger S., Neu P. and Würger A., Phys. Rev. B **52**, 7179 (1995).

2.19 Piché L., Maynard R., Hunklinger S. and Jäckle J., Phys. Rev. Lett. **32**, 1426 (1974).

2.20 Heuer A., Phys. Rev. Lett. **78**, 4051 (1997).

2.21 Yu C. C. and Leggett A. J., Comm. Cond. Matt. Phys. **14**, 231 (1988).

2.22 Fulde P. and Wagner H., Phys. Rev. Lett. **27**, 1280 (1971).

2.23 Galperin Yu. M. and Gurevich V. L., Parshin D. A., Phys. Rev. B **32**, 6873 (1985); Galperin Yu. M. and Gurevich V. L., Parshin D. A., Phys. Rev. B **37**, 10339 (1988); Karpov V. G., Klinger M. I., and Ignat'ev F., Sov. Phys. JETP **57**, 439 (1983). Parshin D. A., Schober H. R. and Gurevich V. L., Phys. Rev. B.**76**, 064206 (2007).

2.24 Kühn R. and Horstmann U., Phys. Rev. Lett. **78**, 4067 (1997); Kühn R., Europhys. Lett. **62**, 313 (2003); van Baardewijk J. and Kühn R., Phys. Rev. B **81**, 054203 (2010).

2.25 Grannan E. R., Randeira M. and Sethna J. P., Phys. Rev. Lett. **60**, 1402 (1988); Grannan E. R., Randeira M. and Sethna J. P., Phys. Rev. B **41**, 7784 (1990); Grannan E. R., Randeira M. and Sethna J. P., Phys. Rev. B **41**, 7799 (1990).

2.26 Cohen M. H. and Grest G. S., Phys. Rev. Lett. **45**, 1271 (1980).

3.1 Weber T. A. and Stillinger F. H., Phys. Rev. B **32**, 5402 (1985).

3.2 Heuer A. and Silbey R. J., Phys. Rev. Lett., **70**, 3911 (1992).

3.3 Heuer A., Phys. Rev. Lett. **78**, 4051 (1996).

3.4 Trachenko K., Dove M. T., Hammonds K. D., Harris M. J. and Heine V., Phys. Rev. Lett., **81**, 3431 (1998).

3.5 Smith D. A., Phys. Rev. Lett. **42**, 729 (1979).

3.6 Guttman L. J. and Rahman S. M., Phys. Rev. B **33**, 1506 (1986).

3.7 Meyer A., Horbach J., Kob W., Kargl F. and Schober H., Phys. Rev. Lett., **93**, 027801-1 (2004).

3.8 Horbach J., Kob W. and Binder K., Chem. Geol. **174**, 87 (2000).

4.1 Enss C., Physica B **316–317**, 12 (2002).

4.2 Freeman J. J. and Anderson A. C., Phys. Rev. B **34,** 5684 (1986).

4.3 Strehlow P. and Wohlfahrt M., Jansen A. G. M., Haueisen R. and Weiss G., Enss C. and Hunklinger S., Phys. Rev. Lett. **84**, 1938 (2000).

4.4 Kettemann S., Fulde P., Strehlow P., Phys. Rev. Lett. **83**, 4325 (1999)

4.5 Rogge S., Natelson D., Tigner B. and Osheroff D. D., Phys. Rev. B **55**, 11256 (1997).

4.6 Wiegers S. A. J., Jochemsen R., Kranenburg C. C.and Frossati G., Rev. Sci. Instrum. **58**, 2274 (1987).

4.7 Frossati G., Gilchrist J.le G., Lasjaunias J.C., and Meyer W., J. Phys. C **10**, L515 (1977).

4.8 Esquinazi P. (Editor), Tunneling Systems in Amorphous and Crystalline Solids (Springer, Berlin) 1998.

4.9 Phillips W. A. (Editor), Amorphous Solids: Low-Temperature Properties (Springer, Berlin) 1981.

4.10 Phillips W. A., Rep. Prog. Phys. **50**, 1657 (1987).

4.11 Strehlow P., Enss C. and Hunklinger S., Phys. Rev. Lett. **80**, 5361 (1998).

4.12 Jug G., Philos. Mag. **84**, 3599 (2004).

4.13 Jug G., Phys. Rev. B **79**, 180201(R) (2009).

4.14 MacDonald W. M., Anderson A. C. and Schroeder J., Phys. Rev. B **31**, 1090 (1985).

4.15 Black J. L., Halperin B. I., Phys. Rev. B **16**, 2879 (1977).

4.16 Fang C.-Y., Yinnon H. and Uhlmann D. R., J. Non-Cryst. Solids **57**, 465 (1983).

4.17 Pellegri N., Dawnay E. J. C. and Yeatman E. M., J. Sol-Gel Sci. Technol. **13**, 783 (1998).

4.18 De G. et al., J. Non-Cryst. Solids **194**, 225 (1996).

4.19 Duan X. L. et al., J. Cryst. Growth **252**, 311 (2003).

4.20 Sussmann J. A., Proc. Phys. Soc. **79**, 758 (1962).

4.21 Schuster G., Hechtfischer G., Buck D. and Hoffmann W., Rep. Prog. Phys. **57**, 187 (1994).

4.22 Bach H. and Krause D., Analysis of the Composition and Structure of Glass and Glass Ceramics (New York: Springer) (1999).

4.23 Jug G. (unpublished)

4.24 Jug G., Paliienko M., EPL **90**, 36002 (2010).

4.25 Black J. L., Phys. Rev. B **17**, 2740 (1978).

4.26 Seibert L, Doctoral Thesis Heidelberg www.kip.uni-heidelberg.de/Veroeffentlichungen/ps/siebert-disser.pdf

4.27 Borisenko A., J. Phys.: Condens. Matter **19**, 416102 (2007).

5.1 Strehlow, P., J. non-crystalline Solids **121**, 463 (1990).

5.2 Strehlow, P., Physica B **165/166**, 25 (1990).

5.3 Strehlow, P.,Cryogenics (ICEC Suppl.) **34**, 421 (1994).

5.4 Schuster, G., Hechtfischer, G., Buck, D., and Hoffmann, W., Rep. Prog. Phys. **57**, 187, 212 (1994).

5.5 Wohlfahrt, M., Strehlow, P., Enss, C., and Hunklinger, S., Europhys. Lett. **56**, 690 (2001).

5.6 Le Cochec, Ladieu F., and P. Pari, Phys. Rev. B **66**, 064203 (2002).

5.7 Aharonov Y., Bohm D., Phys. Rev. **115**, 485 (1959).

5.8 Langari A. Phys. Rev. B **65**, 104201 (2002).

5.9 Würger A, Fleischmann A. and Enss C., Phys. Rev. Lett. **89**, 237601 (2002).

5.10 Nagel P., Fleischmann A., Hunklinger S., Enss C., Phys. Rev. Lett. **92**, 245511 (2004).

5.11 Bazrafshan M., Fickenscher G., Schickfus M.V., Fleischmann A., Enss C., J. Phys.:Conf. Ser. **92**, 012135 (2007).

5.12 Bazrafshan M., Fickenscher G., Schickfus M.V., Fleischmann A., Enss C., J. Phys.:Conf. Ser. **92**, 012135 (2007).

5.13 Bazrafshan M., Fickenscher G., Schickfus M.V., Fleischmann A., Enss C., J. Phys.:Conf. Ser. **150**, 042032 (2009).

5.14 Shumilin A.V., Parshin D.A., JETP Lett. **89**, 553 (2009).

5.15 Bodea D. and Würger A., J. Low Temp. Phys. **136**, 39 (2004).

5.16 Polishchuk Ya., Fulde P., Burin A. L., Sereda Y. and Balamurugan D., J. Low Temp. Phys **140**, 355 (2005).

5.17 Klotz F., Fleischmann A. and Enss C., J. Phys.: Conf. Ser. **150** (2009); Klotz F., Ph.D. Thesis Heidelberg http://webserver.kip.uni-heidelberg.de/Veroeffentlichungen/download.php/4655/ps/1819.PDF

5.18 Borisenko A.and Bakai A., Physica B **388**, 112 (2007).

7.1 Wohlfahrt M., Ph.D. Thesis Heidelberg, 2001 www.ub.uni-heidelberg.de/archiv/1587 .

8.1 Smolyakov B.P. and Khaimovich E.P., Pis'ma Zh. Eksp. Teor. Fiz. **29**, 464 (1979) [courtesy A. Borisenko].

9.1 Phillips W. A., Rep. Prog. Phys. 50, 1657 (1987) (Section 5).

9.2 Ludwig S, Enss C., Hunklinger S., and Strehlow P., Phys. Rev. Lett. **88**, 075501 (2002); Ludwig S., Nagel P., Hunklinger S. and Enss C., J. Low Temp. Phys. **131**, 89 (2003).

9.3 Brandt M., Ph.D. Thesis Heidelberg http://www.ub.uni-heidelberg.de/archiv/4822; Brandt M., Nagel P., Fleischmann A., Enss C. and Hunklinger S., Phys. Stat. Sol. (c) **1**, 2875 (2004).

9.4 Fleischmann A. and Enss C., *Geheimnis der Tunnelsysteme im Glas gelüftet*, Physik Journal **6** (Nr. 10), 41 (2007).

9.5 Nagel P., Fleischmann A., Hunklinger S. And Enss C., Phys. Rev. Lett. **92**, 245511 (2004).

9.6 Gurevich V. L., Muradov M. I., and Parshin D. A., Sov. Phys. JETP **5**, 928 (1990).

9.7 GalperinYu. M., Gurevich V. L. and Parshin D. A, Phys. Rev. B **37**, 10339 (1988).

9.8 Klauder J. R. and Anderson P. W., Phys. Rev. **125**, 912 (1962).

9.9 Borisenko A. and Jug G. (2011, unpublished).

9.10 Black J. L. and Halperin B. I., Phys. Rev. B 16, 2879 (1977).

9.11 Enss C., Weis R., Ludwig S. and Hunklinger S., Czech. J. Phys. **46** (S6), 3287 (1996); Enss C., Ludwig S., Weis R., and Hunklinger S., Czech. J. Phys. **46** (S4), 2247 (1996).

9.12 Maynard R., Rammal R. and Suchail R., J. Physique Lett. **41**, L-291 (1980).

9.13 Bachellerie A. and Legros P., J. Physique Lett. **41**, L-603 (1980).

9.14 Corrington M. S., Math. And Comput. 15, **1** (1961) (6.18).

10.1 Lubchenko V. and Wolynes P. G., Phys. Rev. Lett. **87**, 195901 (2001).

10.2 Klein M. W., Fischer B, Anderson A. C., and Anthony P. J., Phys. Rev. B **18**, 5887 (1978).

10.3 Klein M. W., Phys. Rev. B **29**, 5887 (1984).

11.1 Katzgraber H. G., Larson D and Young P., Phys. Rev. Lett. **102**, 177205 (2009).

11.2 Tabata Y., Matsuda K., Kanada S., Yamazaki T., Waki T., Nakamura H, Sato K. and Kindo K., arXiv: cond-mat.dis-nn/1009.6115v2 (courtesy G. Parisi).